

UNIVERSITY OF ZAGREB
FACULTY OF SCIENCE
DEPARTMENT OF PHYSICS

Marinko Jablan

Electrodynamic properties of graphene and their technological applications

Doctoral Thesis submitted to the Department of Physics
Faculty of Science, University of Zagreb
for the academic degree of
Doctor of Natural Sciences (Physics)

Zagreb, 2012.

SVEUČILIŠTE U ZAGREBU
PRIRODOSLOVNO-MATEMATIČKI FAKULTET
FIZIČKI ODSJEK

Marinko Jablan

Elektrodinamička svojstva grafena i primjene u tehnologiji

Doktorska disertacija
predložena Fizičkom odsjeku
Prirodoslovno-matematičkog fakulteta Sveučilišta u Zagrebu
radi stjecanja akademskog stupnja
doktora prirodnih znanosti fizike

Zagreb, 2012.

University of Zagreb
Faculty of Science
Department of Physics

Doctoral Thesis

Electrodynamic properties of graphene and their technological applications

MARINKO JABLAN

Faculty of Science, University of Zagreb

Graphene is a novel two-dimensional material with fascinating electrodynamic properties like the ability to support collective electron oscillations (plasmons) accompanied by tight confinement of electromagnetic fields. Our goal is to explore light-matter interaction in graphene in the context of plasmonics and other technological applications but also to use graphene as a platform for studying many body physics like the interaction between plasmons, phonons and other elementary excitations. Plasmons and plasmon-phonon interaction are analyzed within the self-consistent linear response approximation. We demonstrate that electron-phonon interaction leads to large plasmon damping when plasmon energy exceeds that of the optical phonon but also a peculiar mixing of plasmon and optical phonon polarizations. Plasmon-phonon coupling is strongest when these two excitations have similar energy and momentum. We also analyze properties of transverse electric plasmons in bilayer graphene. Finally we show that thermally excited plasmons strongly mediate and enhance the near field radiation transfer between two closely separated graphene sheets. We also demonstrate that graphene can be used as a thermal emitter in the near field thermophotovoltaics leading to large efficiencies and power densities. Near field heat transfer is analyzed withing the framework of fluctuational electrodynamics.

Keywords: graphene / plasmonics / loss / plasmon / transverse electric mode / plasmon-phonon coupling / near-field / heat transfer / thermophotovoltaics

(99 pages, 71 references, original in English)

Supervisor: Prof. Dr. sc. H. Buljan

Co-supervisor: Prof. Dr. sc. M. Soljačić, Massachusetts Institute of Technology, USA

Committee: Prof. Dr. sc. A. Bjeliš
Prof. Dr. sc. H. Buljan
Prof. Dr. sc. M. Soljačić, Massachusetts Institute of Technology, USA
Dr. sc. I. Kupčić, v. zn. sur.
Dr. sc. M. Kralj, v. zn. sur., Institute of Physics

Replacements: Prof. Dr. sc. S. Barišić
Dr. sc. I. Bogdanović-Radović, v. zn. sur., Ruđer Bošković Institute

Thesis accepted: 2012.

TEMELJNA DOKUMENTACIJSKA KARTICA

Sveučilište u Zagrebu
Prirodoslovno-matematički fakultet
Fizički odsjek

Doktorska disertacija

Elektrodinamička svojstva grafena i primjene u tehnologiji

MARINKO JABLAN

Prirodoslovno-matematički fakultet, Sveučilište u Zagrebu

Grafen je tek nedavno otkriveni dvo-dimenzionalan materijal s vrlo zanimljivim elektrodinamičkim svojstvima poput mogućnosti podržavanja kolektivnih oscilacija elektronskog plina (plazmona) praćenih s jakom lokalizacijom elektromagnetskog polja. Cilj ovog doktorata je proučiti interakciju svjetlosti i materije u grafenu u kontekstu plazmonike i drugih tehnoloških primjena ali također upotrijebiti grafen kao platformu za istraživanje pojava fizike mnoštva čestica kao što su interakcija između plazmona, fonona i drugih elementarnih pobuđenja. Plazmone i plazmon-fonon interakciju analiziramo u kontekstu aproksimacije samo-konzistentnog linearnog odziva. Pokazujemo da elektron-fonon interakcija vodi k jakom gušenju plazmona kada energija plazmona prijeđe energiju optičkog fonona ali također neobično miješanje polarizacija plazmona i optičkog fonona. Plazmon-fonon vezanje je najjače kad ta dva pobuđenja imaju usporedivu energiju i impuls. Također analiziramo svojstva transverzalnog električnog plazmona u dvo-sloju grafena. Konačno pokazujemo da termalno pobuđeni plazmoni kanaliziraju i bitno pospješuju radiativni transfer topline između dvije bliske ravnine grafena. Također pokazujemo da se grafen može koristiti kao termalni emiter u termofotovoltaičima bliskog polja što vodi k velikim efikasnostima i gustoći snage. Prijenos topline u bliskom polju analiziramo u kontekstu fluktuacijske elektrodinamike.

Ključne riječi: grafen / plazmonika / gušenja / plazmon / transverzalni električni mod / plazmon-fonon vezanje / blisko-polje / prijenos topline / termofotovoltaiči

(99 stranica, 71 literaturnih navoda, jezik izvornika engleski)

Mentor: Prof. Dr. sc. H. Buljan

Ko-mentor: Prof. Dr. sc. M. Soljačić, Massachusetts Institute of Technology, SAD

Komisija: Prof. Dr. sc. A. Bjeliš
Prof. Dr. sc. H. Buljan
Prof. Dr. sc. M. Soljačić, Massachusetts Institute of Technology, SAD
Dr. sc. I. Kupčić, v. zn. sur.
Dr. sc. M. Kralj, v. zn. sur., Institut za fiziku

Zamjene: Prof. Dr. sc. S. Barišić
Dr. sc. I. Bogdanović-Radović, v. zn. sur., Institut Ruđer Bošković

Radnja prihvaćena: 2012.

Acknowledgements

The work in this thesis was completed under the supervision of Prof. Dr. Hrvoje Buljan at the University of Zagreb and Prof. Dr. Marin Soljačić at the Massachusetts Institute of Technology. I would like to thank both for their generous help and guidance during my research as a graduate student. I would like to thank Hrvoje for his tremendous patience but even more for opening my mind to discussion and showing me how powerful it can be when two very different minds cooperate. I would also like to thank Marin for giving me the opportunity to work in the stimulating environment of MIT but even more for his incredible insight into the current trends of modern science. At last I would like to thank Dr. Ivan Celanović and Ognjen Ilić for the effort and time they invested in our papers. I would especially like to thank Ognjen for our stimulating discussions and for reminding me that in the end it is math that tells you how big things really are.

The work presented in this thesis has been published in several articles. The reference for each chapter is given below.

Chapter 3:

M. Jablan, H. Buljan and M. Soljačić
Plasmonics in graphene at infrared frequencies,
Phys. Rev. B **80**, 245435 (2009).

Chapter 4:

M. Jablan, H. Buljan and M. Soljačić
Transverse electric plasmons in bilayer graphene,
Optics Express **19**, 11236 (2011).

Chapter 5:

M. Jablan, M. Soljačić and H. Buljan,
Unconventional plasmon-phonon coupling in graphene,
Phys. Rev. B **83**, 161409(R) (2011).

Chapter 6:

O. Ilic, M. Jablan, J. D. Joannopoulos, I. Celanovic, H. Buljan and M. Soljačić
Near-field thermal radiation transfer controlled by plasmons in graphene,
arXiv:1201.1489, accepted for publication in Phys. Rev. B (2012).

O. Ilic, M. Jablan, J. D. Joannopoulos, I. Celanovic and M. Soljačić
Overcoming the black body limit in plasmonic and graphene near-field thermophotovoltaic systems,
Optics Express, **20**, A366 (2012).

Contents

Acknowledgements	xi
Contents	xiii
1 Introduction	1
1.1 Experimental realization	1
1.2 Plasmonics	2
1.3 Near field thermo-photo-voltaics	3
1.4 Objectives and results	4
2 Methods	7
2.1 Tight binding approximation in graphene	7
2.1.1 Electron band structure	7
2.1.2 Dirac electron dispersion in graphene	12
2.1.3 Electron-phonon interaction	14
2.2 Response functions	20
2.2.1 Conductivity	20
2.2.2 Density-density response function	24
2.2.3 Current-current response function	28
2.2.4 Fluctuation-dissipation theorem	30
2.3 Radiative heat transfer	32
3 Plasmonics in graphene	39
3.1 Surface plasmons	40
3.2 Plasmons and their losses in doped graphene	41
3.2.1 Semiclassical model	43
3.2.2 RPA and relaxation-time approximation	44

3.2.3	Losses due to optical phonons	47
3.3	Conclusion and Outlook	50
4	Transverse-electric plasmons	53
4.1	Optical conductivity of bilayer graphene	54
4.2	Transverse-electric plasmon dispersion in bilayer graphene	57
5	Plasmon-phonon coupling	61
6	Near field heat transfer	71
6.1	Near field heat transfer between two graphene sheets	71
6.2	Near field thermo-photo-voltaics using graphene as a thermal emitter	76
7	Summary	79
A	Plasmon-phonon coupling in the context of Feynman diagrams	81
	Bibliography	89
	List of Figures	95

Chapter 1

Introduction

Carbon is a basic ingredient of life and all organic chemistry which is consequence of its abundance in nature and his chemical reactivity. With four valence electrons distributed to one $2s$ and three $2p$ orbitals, which can hybridize in many different ways, carbon is characterized by a large flexibility of chemical bonding. One particularly interesting case is sp^2 hybridization which creates three strong σ -bonds in plane, while the remaining p orbital is weakly bound with neighboring atoms creating π -bond. In this thesis we will be studying graphene: a two-dimensional (2D) crystal of carbon atoms assembled in a honeycomb structure. While σ -bond is responsible for the most of the structural integrity of graphene, π -bond determines low-energy electric and optical properties. Very peculiar property of graphene is that its low-energy electrons behave as massless Dirac particles [1, 2] (near the corners of the Brillouin zone). Since graphene is essentially a 2D material, one can simply tune its Fermi level through an electrostatic gating which brings about large control over electrical and optical properties, important for various technological applications.

1.1 Experimental realization

Scientists were puzzled for long time whether nature allows existence of a two-dimensional crystal. In 1930's Peierls [3] and Landau [4] showed that thermal fluctuations would destroy long range order and essentially melt 2D lattice at any finite temperature. Therefore it came as a surprise when Geim and

Novoselov announced [5, 6, 7] in 2004 a discovery of a first 2D crystal made of carbon atoms - graphene. Scientist were further astonished by a sheer simplicity of the experimental method which essentially used a scotch tape to exfoliate graphite (graphite can be viewed as a simple stack of weakly bound graphene planes). The 2010 Nobel prize in physics came as a credit for this great discovery but it is interesting that even today in 2012 experimentalists still use this "scotch tape technique" since it offers exceptionally pure graphene samples on a small scale, important for fundamental research. Of course it is impractical on a large scale production which is required by various industrial applications, and soon after the discovery of graphene several other methods were developed for graphene production, most notably chemical vapor deposition (CVD) [8], segregation by heat treatment of carbon-containing substrates [9] and liquid phase exfoliation [10]. The most promising of these methods, for large scale graphene growth, is CVD which is also used [11] by the group of Dr. Marko Kralj from the Institute of Physics in Zagreb, Croatia. They heat ethylene (C_2H_4) gas, up to a temperature of $1000^\circ C$, above the metal surface which serves both as a catalyst for ethylene decomposition and substrate for graphene growth.

It is interesting to note that various groups claim they have seen graphene in their experiments prior to 2004 but it wasn't until Geim and Novoselov groundbreaking experiments that the true potential and importance of graphene was recognized.

While graphene's intriguing mechanical properties are still debated, this thesis concerns primarily with electrical and optical properties which are a subject of intense research and numerous practical applications.

1.2 Plasmonics

Plasmonics studies collective electron surface charge oscillations (surface plasmons at surfaces of bulk materials or plasmons in a pure 2D materials like graphene) accompanied by tight confinement of electromagnetic (EM) fields. In recent years, an enormous interest has been surrounding the field of plasmonics, because of the variety of tremendously exciting and novel phenomena it could enable. On one hand, plasmonics seems to be the only viable path

toward realization of nanophotonics: control of light at scales substantially smaller than the wavelength [12, 13, 14, 15]. On the other hand, plasmonics is a crucial ingredient for implementation of most metamaterials, and thereby all the exciting phenomena that they support [16, 17, 18, 19], including negative refraction, superlensing, and cloaking. However, there is one large and so far insurmountable obstacle towards achieving this great vision: plasmonic materials (most notably metals) have enormous losses in the frequency regimes of interest. This greatly motivates us to explore plasmons and their losses in a newly available material with unique properties: graphene [5, 6, 7].

Plasmons are also very interesting phenomenon from the point of view of many-body physics. Since losses are in a large manner determined by phonons we will encounter interactions between various elementary excitations and interesting many-body effects like plasmon-phonon coupling.

1.3 Near field thermo-photo-voltaics

Radiative heat transfer between two bodies can be greatly enhanced in the *near field*, i.e. by bringing the surfaces close together to allow tunneling of evanescent photon modes [20, 21, 22]. This happens because near field radiation transfer involves thermal excitation of various surface modes which can have much greater wave vectors (and density of states) than the freely propagating modes (limited by the light line). Since each wave vector corresponds to a heat channel, vacuum becomes better heat conductor in the near field. However, due to their localization and evanescent nature, it is only at sub-wavelength separations that these modes become relevant. While measuring near field transfer has been experimentally difficult [23, 24, 25, 26], the promise of order-of-magnitude enhancements over the far field Stefan-Boltzman black body limit has made transfer in the near field the topic of much research.

With the current world energy demand and large environmental impact of fossil fuels there is a worldwide shift toward renewable energy sources. In that respect, thermo-photo-voltaics (TPVs) are a promising class of heat to electricity conversion devices [27, 28] where Sun can heat up an emitter that selectively re-radiates frequencies matched to the band gap of the photo-voltaic cell thus minimizing the thermalization losses. TPVs are not limited by the

Sun source and can use any hot (terrestrial) object like a factory furnace or various hot car parts as a heat source. From the perspective of future energy crisis there is a large demand for more efficient energy management where TPVs can play important role by turning wasted heat into electricity.

Near field TPVs [29, 30, 31] further offer greater power densities since the near field heat transfer can be orders of magnitude larger than the far field limit. Finally, due to evanescent nature of EM modes, one does not need to worry about losing energy through modes with frequencies below the photovoltaic band gap, resulting in even larger device efficiencies.

1.4 Objectives and results

The objective of this research is to study electrodynamic properties of graphene and especially high-frequency collective oscillations of electrons (plasmons). We will analyze plasmon excitations in the context of plasmonics and other technological applications, but we will also look at the same problem from the point of view of many-body physics as an interaction between various elementary excitations (plasmons, phonons, etc.). Finally we study near field heat transfer with graphene (mediated by thermally excited plasmons) in the context of TPVs.

We study plasmon excitations in graphene in the context of the Random Phase Approximation (RPA) [56] and number-conserving relaxation-time approximation [34] and we show that plasmons in doped graphene can have both low losses and large localization for frequencies below optical phonon energy at 0.2 eV. Large plasmon damping occurs in the regime of interband single particle excitations which can be shifted towards larger energies for stronger doping values. We demonstrate that for sufficiently large doping there is a frequency interval from optical phonon frequency to boundary of interband regime, where the plasmon damping is dominated by emission of optical phonon and electron-hole pair. To describe impurity scattering we use DC relaxation time since we don't expect significant frequency dependence. The phonon contribution is estimated from the electron self-energy induced by electron-phonon interaction.

We also explore electron-phonon interaction in graphene as an interesting problem from the aspect of many-body physics. By measuring Raman shift of

optical phonon energy it was demonstrated that Born-Oppenheimer approximation (BOA) is not a valid approximation in graphene [32]. The measured Raman shift is a consequence of the interaction with single particle excitations, however the breakdown of BOA means that electrons and phonons move on comparable energy scales which leads to a possibility of interaction between phonons and collective electron excitations (plasmons). We show that a peculiar type of hybridization of plasmon and optical phonon modes occurs around the point where the two modes cross in energy and momentum simultaneously since then the electron-phonon interaction will be drastically increased due to collective electron response. We demonstrate that the electron-phonon interaction leads to polarization mixing of the two modes so that longitudinal plasmon (LP) couples exclusively to the transverse optical phonon (TO) mode, while the transverse electric mode, also referred to as the transverse plasmon (TP), couples exclusively to longitudinal optical phonon (LO) mode; thus there is no coupling between LPs and LO modes. Formally, we analyze plasmon-phonon coupling in the self-consistent linear-response formalism which describes interaction of phonons with both single particle and collective electronic excitations. We emphasize that the phonon interaction with collective excitations is much larger than the phonon interaction with single particle excitations (measured by Raman) which means that plasmon-phonon interaction can serve as a magnifier for exploring electron-phonon interaction in graphene. Further on, our calculations give a slight correction to the standard result of Raman shift of the optical phonon energy since the longwave phonons can interact also with radiative EM modes so that we predict increasing Raman linewidths for higher dopings. Finally we note that LO phonon decouples from all (single particle and collective) electronic excitations when its dispersion crosses the light line.

While longitudinal charge density oscillation can be referred to as longitudinal plasmon, which is also polarized like transverse-magnetic (TM) EM mode, we also analyze properties of the unusual transverse plasmon in 2D systems [48], which is polarized like transverse-electric (TE) mode, and accompanied by transverse current density oscillation. These kind of modes are possible only if the imaginary part of 2D conductivity is negative which in principle requires interband transitions. From that perspective bilayer graphene is an interesting candidate for exploring these modes, because it has a rich band structure and particularly two perfectly nested bands with a gap of 0.4 eV

which results in large joint density of states considering the vertical interband transitions. We show that plasmon properties (localization) of TE modes are much more pronounced in bilayer than in single layer graphene.

We also show that thermally excited plasmons strongly mediate and enhance the near field radiation transfer between two closely separated graphene sheets. Near field heat transfer is analyzed within the framework of fluctuational electrodynamics and we predict several orders of magnitude larger values of heat transfer between two graphene sheets in the near field than the case of heat transfer between two black bodies, of the same temperatures, in the far field. Finally we demonstrate that graphene can be used as a thermal emitter in the near field thermophotovoltaics leading to large efficiencies and power densities.

The thesis is organized into chapters as follows. In Chapter 2 we present theoretical methods and tools that will be used throughout the text. We first calculate electron dispersion and electron-phonon interaction Hamiltonian in graphene within the tight binding approximation. Next we give the density-density and current-current response functions in the linear approximation and use fluctuation-dissipation theorem to calculate current-current correlation function due to thermal fluctuations in the system. Finally we use this to calculate the radiative heat transfer between two graphene sheets. In Chapter 3 we calculate plasmon dispersion and damping due to electron-impurity and electron-phonon scattering. In Chapter 4 we calculate dispersion of TE modes in single and bilayer graphene. In Chapter 5 we calculate plasmon-phonon interaction within the self-consistent linear response formalism. In Chapter 6 we calculate near field heat transfer between two graphene sheets and we analyze near field TPV device with graphene as a thermal emitter. Finally, in Chapter 7 we summarize.

Chapter 2

Methods

In this chapter, for the sake of the clarity of the presentation, we derive basic physical quantities used to describe graphene such as the low energy Dirac Hamiltonian and the electron-phonon interaction. We will also define standard response functions, like the conductivity, density-density, and current-current response functions, that will be used in later chapters. This chapter is intended to provide an introduction and overview of these concepts so the reader already familiar with them can skip the corresponding sections. Finally we will derive an expression for the radiative heat transfer between two graphene sheets at different temperatures by employing the fluctuation-dissipation theorem.

2.1 Tight binding approximation in graphene

In this section we use the tight-binding approximation to derive the electron band structure of graphene, Dirac equation valid at low energies and electron-phonon interaction.

2.1.1 Electron band structure

Graphene crystal structure is determined by a Bravais lattice with two atoms in a basis (see figure 2.1). We can choose unit cell vectors as $\mathbf{a}_1 = a(1, 0)$ and $\mathbf{a}_2 = a(-1/2, \sqrt{3}/2)$, while the vectors connecting first neighbors are given by $\boldsymbol{\tau}_1 = a(0, 1/\sqrt{3})$, $\boldsymbol{\tau}_2 = a(-1/2, -1/2\sqrt{3})$, and $\boldsymbol{\tau}_3 = a(1/2, -1/2\sqrt{3})$. Here $a = 0.25$ nm is a lattice constant while the nearest neighbor carbon-carbon distance is $|\boldsymbol{\tau}_l| = b = a/\sqrt{3} = 0.14$ nm.

Unit cell vectors of reciprocal lattice are given by $\mathbf{c}_1 = (2\pi/a)(1, 1/\sqrt{3})$ and $\mathbf{c}_2 = (2\pi/a)(0, 2/\sqrt{3})$, while we are primarily interested in the vertex points of the Brillouin zone i.e. vectors $\mathbf{K} = (2\pi/a)(1/3, 1/\sqrt{3})$ and $\mathbf{K}' = (2\pi/a)(2/3, 0)$. The remaining four vertex points are equivalent to the points \mathbf{K} i \mathbf{K}' since they are connected to them by a simple translation with the reciprocal vector $n_1\mathbf{c}_1 + n_2\mathbf{c}_2$, where n_1 and n_2 are integers.

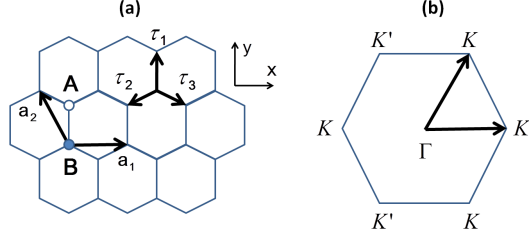


Figure 2.1: a) Graphene crystal structure. Unit cell vectors are \mathbf{a}_1 and \mathbf{a}_2 while A and B are atoms of the basis. b) Brillouin zone. We mark high symmetry points \mathbf{K} and \mathbf{K}' where the low-energy electron excitations are described by massless Dirac equation.

As we already pointed out in the introduction, *sp*² hybridization is responsible for the mechanical stability of graphene by creating three strong σ bonds in *xy* plane while the remaining p_z orbital weakly interacts with the neighborings p_z orbitals creating the π bond. Since we are particularly interested in π bond, the entire problem is very well described with the tight binding approximation [1].

Let us define now an operator $c_{\mathbf{R}}^\dagger$ that creates a free p_z orbital at the lattice point \mathbf{R} , i.e. $|p_z(\mathbf{R})\rangle = c_{\mathbf{R}}^\dagger|0\rangle$. Let us further denote by $-\gamma_0$ the hopping integral between nearest neighbor p_z orbitals (next-nearest neighbor interaction is negligible and $\gamma_0 \approx 2.8$ eV [1]). Since we are only interested in the behavior of the electron energies near the p_z orbital energy, our system is well described by a tight binding Hamiltonian

$$H = -\gamma_0 \sum_{\mathbf{R}_A, \tau_l} c_{\mathbf{R}_A - \tau_l}^\dagger c_{\mathbf{R}_A} - \gamma_0 \sum_{\mathbf{R}_B, \tau_l} c_{\mathbf{R}_B + \tau_l}^\dagger c_{\mathbf{R}_B}, \quad (2.1)$$

where the sum over lattice points is divided into two parts that contain different basis atoms i.e. $\mathbf{R}_A = n_1\mathbf{a}_1 + n_2\mathbf{a}_2 + \tau_1$ and $\mathbf{R}_B = n_1\mathbf{a}_1 + n_2\mathbf{a}_2$ (n_1 and n_2 are integers). In equation (2.1), we have assumed that zero energy corresponds to

p_z orbital energy (i.e. $E(p_z) = 0$) and we have neglected overlapping of the two neighboring orbitals. We have also omitted the notion of electron spin since it only plays the role of additional degree of freedom. Eigenstates of the Hamiltonian (2.1) must take the form of the linear combination of p_z orbitals that satisfy the Bloch condition

$$c_{\mathbf{k}}^\dagger = \frac{1}{\sqrt{N}} \sum_{\mathbf{R}_A} e^{i\mathbf{k}\cdot\mathbf{R}_A} c_{\mathbf{R}_A}^\dagger f_A(\mathbf{k}) + \frac{1}{\sqrt{N}} \sum_{\mathbf{R}_B} e^{i\mathbf{k}\cdot\mathbf{R}_B} c_{\mathbf{R}_B}^\dagger f_B(\mathbf{k}) Z, \quad (2.2)$$

where we have explicitly separated the phase Z ($Z^*Z = 1$) which will be defined later so that analytical expressions would look as simple as possible. Let us define now Fourier transform of operators $c_{\mathbf{R}_A}^\dagger$ and $c_{\mathbf{R}_B}^\dagger$ as

$$A_{\mathbf{k}}^\dagger = \frac{1}{\sqrt{N}} \sum_{\mathbf{R}_A} e^{i\mathbf{k}\cdot\mathbf{R}_A} c_{\mathbf{R}_A}^\dagger, \text{ and} \quad (2.3)$$

$$B_{\mathbf{k}}^\dagger = \frac{Z}{\sqrt{N}} \sum_{\mathbf{R}_B} e^{i\mathbf{k}\cdot\mathbf{R}_B} c_{\mathbf{R}_B}^\dagger. \quad (2.4)$$

Then, the Bloch eigenstate (2.2) is $c_{\mathbf{k}}^\dagger = f_A(\mathbf{k})A_{\mathbf{k}}^\dagger + f_B(\mathbf{k})B_{\mathbf{k}}^\dagger$, and we can also write the inverse Fourier transforms (since $Z^*Z = 1$) as

$$c_{\mathbf{R}_A}^\dagger = \frac{1}{\sqrt{N}} \sum_{\mathbf{k}} e^{-i\mathbf{k}\cdot\mathbf{R}_A} A_{\mathbf{k}}^\dagger, \text{ and} \quad (2.5)$$

$$c_{\mathbf{R}_B}^\dagger = \frac{Z^*}{\sqrt{N}} \sum_{\mathbf{k}} e^{-i\mathbf{k}\cdot\mathbf{R}_B} B_{\mathbf{k}}^\dagger. \quad (2.6)$$

Let us look now at the first sum from (2.1) and notice that every vector $\mathbf{R}_A - \boldsymbol{\tau}_l$ is in fact one of the \mathbf{R}_B vectors, so we have

$$\begin{aligned} \sum_{\mathbf{R}_A, \boldsymbol{\tau}_l} c_{\mathbf{R}_A - \boldsymbol{\tau}_l}^\dagger c_{\mathbf{R}_A} &= \sum_{\mathbf{R}_A, \boldsymbol{\tau}_l} \left(\frac{Z^*}{\sqrt{N}} \sum_{\mathbf{k}'} e^{-i\mathbf{k}'\cdot(\mathbf{R}_A - \boldsymbol{\tau}_l)} B_{\mathbf{k}'}^\dagger \right) \left(\frac{1}{\sqrt{N}} \sum_{\mathbf{k}} e^{i\mathbf{k}\cdot\mathbf{R}_A} A_{\mathbf{k}} \right) \\ &= \sum_{\mathbf{k}, \mathbf{k}', \boldsymbol{\tau}_l} Z^* e^{i\mathbf{k}'\cdot\boldsymbol{\tau}_l} B_{\mathbf{k}'}^\dagger A_{\mathbf{k}} \sum_{\mathbf{R}_A} \frac{1}{N} e^{i(\mathbf{k}-\mathbf{k}')\cdot\mathbf{R}_A}. \end{aligned} \quad (2.7)$$

However, since

$$\sum_{\mathbf{R}_A} \frac{1}{N} e^{i(\mathbf{k}-\mathbf{k}')\cdot\mathbf{R}_A} = \delta_{\mathbf{k}, \mathbf{k}'}, \quad (2.8)$$

we obtain in the first sum

$$\sum_{\mathbf{R}_A, \boldsymbol{\tau}_l} c_{\mathbf{R}_A - \boldsymbol{\tau}_l}^\dagger c_{\mathbf{R}_A} = \sum_{\mathbf{k}, \boldsymbol{\tau}_l} Z^* e^{i\mathbf{k} \cdot \boldsymbol{\tau}_l} B_{\mathbf{k}}^\dagger A_{\mathbf{k}}. \quad (2.9)$$

In a similar manner we get the second sum

$$\begin{aligned} \sum_{\mathbf{R}_B, \boldsymbol{\tau}_l} c_{\mathbf{R}_B + \boldsymbol{\tau}_l}^\dagger c_{\mathbf{R}_B} &= \sum_{\mathbf{R}_B, \boldsymbol{\tau}_l} \left(\frac{1}{\sqrt{N}} \sum_{\mathbf{k}'} e^{-i\mathbf{k}' \cdot (\mathbf{R}_B + \boldsymbol{\tau}_l)} A_{\mathbf{k}'}^\dagger \right) \left(\frac{Z}{\sqrt{N}} \sum_{\mathbf{k}} e^{i\mathbf{k} \cdot \mathbf{R}_B} B_{\mathbf{k}} \right) \\ &= \sum_{\mathbf{k}, \boldsymbol{\tau}_l} Z e^{-i\mathbf{k} \cdot \boldsymbol{\tau}_l} A_{\mathbf{k}}^\dagger B_{\mathbf{k}}. \end{aligned} \quad (2.10)$$

Finally, the Hamiltonian (2.1) becomes

$$H = -\gamma_0 \sum_{\mathbf{k}} \left(\sum_l Z^* e^{i\mathbf{k} \cdot \boldsymbol{\tau}_l} \cdot B_{\mathbf{k}}^\dagger A_{\mathbf{k}} + \sum_l Z e^{-i\mathbf{k} \cdot \boldsymbol{\tau}_l} \cdot A_{\mathbf{k}}^\dagger B_{\mathbf{k}} \right). \quad (2.11)$$

Relation (2.11) contains a specially important function

$$T(\mathbf{k}) = -\gamma_0 \sum_l Z e^{-i\mathbf{k} \cdot \boldsymbol{\tau}_l}, \quad (2.12)$$

so finally we can write equation (2.11) in a matrix form

$$H = \sum_{\mathbf{k}} \begin{pmatrix} A_{\mathbf{k}}^\dagger & B_{\mathbf{k}}^\dagger \end{pmatrix} \begin{pmatrix} 0 & T(\mathbf{k}) \\ T^*(\mathbf{k}) & 0 \end{pmatrix} \begin{pmatrix} A_{\mathbf{k}} \\ B_{\mathbf{k}} \end{pmatrix}. \quad (2.13)$$

Now, since the Bloch state $c_{\mathbf{k}}^\dagger = f_A(\mathbf{k})A_{\mathbf{k}}^\dagger + f_B(\mathbf{k})B_{\mathbf{k}}^\dagger$ has to diagonalize this Hamiltonian, we can also write

$$H = \sum_{\mathbf{k}} E(\mathbf{k}) c_{\mathbf{k}}^\dagger c_{\mathbf{k}} = \sum_{\mathbf{k}} E(\mathbf{k}) \begin{pmatrix} A_{\mathbf{k}}^\dagger & B_{\mathbf{k}}^\dagger \end{pmatrix} \begin{pmatrix} f_A(\mathbf{k}) \\ f_B(\mathbf{k}) \end{pmatrix} \begin{pmatrix} f_A^*(\mathbf{k}) & f_B^*(\mathbf{k}) \end{pmatrix} \begin{pmatrix} A_{\mathbf{k}} \\ B_{\mathbf{k}} \end{pmatrix}. \quad (2.14)$$

By comparing equations (2.13) and (2.14) we need to have:

$$\begin{pmatrix} 0 & T(\mathbf{k}) \\ T^*(\mathbf{k}) & 0 \end{pmatrix} \begin{pmatrix} f_A(\mathbf{k}) \\ f_B(\mathbf{k}) \end{pmatrix} = E(\mathbf{k}) \begin{pmatrix} f_A(\mathbf{k}) \\ f_B(\mathbf{k}) \end{pmatrix}. \quad (2.15)$$

So we have reduced entire problem to the matrix diagonalization, while the

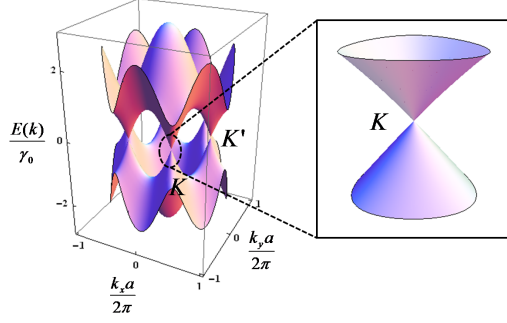


Figure 2.2: Graphene electron band structure with Dirac cones around \mathbf{K} point (magnified). Intrinsic graphene has Fermi level $E_F = E_{\mathbf{K}} = 0$.

eigenvalues (i.e. energies) are given by:

$$\begin{vmatrix} -E(\mathbf{k}) & T(\mathbf{k}) \\ T^*(\mathbf{k}) & -E(\mathbf{k}) \end{vmatrix} = 0. \quad (2.16)$$

Solution of the determinant equation (2.16) determines the electron band structure in graphene as [1]:

$$E_{\pm}(\mathbf{k}) = \pm \sqrt{T(\mathbf{k})T^*(\mathbf{k})} = \pm \gamma_0 \sqrt{1 + 4 \cos \frac{ak_x}{2} \cos \frac{ak_y \sqrt{3}}{2} + 4 \cos^2 \frac{ak_x}{2}}. \quad (2.17)$$

Figure 2.2 shows the function $E(\mathbf{k})$ and we can notice the peculiar behavior of the bands at the Brillouin zone vertex points \mathbf{K} and \mathbf{K}' . Further on, since each graphene unit cell contains two atoms in basis and each atom donates one free electron into the band, Fermi energy is defined such that there are enough electrons to fill precisely one Brillouin zone in the reciprocal space. Relation (2.17) tells us that electron bands are divided into positive and negative states that touch precisely at the the vertex point of the Brillouin zone (see also figure 2.2), such that we have $E_F = E_{\mathbf{K}} = 0$. Because of the fact that electron states around the Fermi energy determines the low-energy properties, we will focus precisely on the area around the \mathbf{K} and the \mathbf{K}' points. Finally we note that, since valence (negative) and conduction (positive) band touch at only 6 points (\mathbf{K} , \mathbf{K}' and the remaining four equivalent vertex points), that are located precisely at the Fermi level, the intrinsic graphene is an unusual zero gap semiconductor.

2.1.2 Dirac electron dispersion in graphene

We can write equation (2.15) as an eigenvalue equation: $H_{\mathbf{k}}\psi_{\mathbf{k}} = E_{\mathbf{k}}\psi_{\mathbf{k}}$, where the Hamiltonian and the wave function (eigenfunction) are given by

$$H_{\mathbf{k}} = \begin{pmatrix} 0 & T(\mathbf{k}) \\ T^*(\mathbf{k}) & 0 \end{pmatrix}, \text{ and} \quad (2.18)$$

$$\psi_{\mathbf{k}} = \begin{pmatrix} f_A(\mathbf{k}) \\ f_B(\mathbf{k}) \end{pmatrix}. \quad (2.19)$$

Let us focus now on the area around the \mathbf{K} point and change the origin of our wave vector as $\mathbf{k} \rightarrow \mathbf{k} + \mathbf{K}$, so that we have $|\mathbf{k}| \ll |\mathbf{K}|$. Now we can make a Taylor expansion of the function $T(\mathbf{k})$ as follows:

$$T(\mathbf{k}) = -\gamma_0 \sum_l Z e^{-i(\mathbf{k}+\mathbf{K})\cdot\boldsymbol{\tau}_l} \approx -\gamma_0 \sum_l Z e^{-i\mathbf{K}\cdot\boldsymbol{\tau}_l} (1 - i\mathbf{k}\cdot\boldsymbol{\tau}_l). \quad (2.20)$$

Next we calculate the following sums:

$$\sum_l e^{-i\mathbf{K}\cdot\boldsymbol{\tau}_l} = 0, \text{ and} \quad (2.21)$$

$$\sum_l \boldsymbol{\tau}_l e^{-i\mathbf{K}\cdot\boldsymbol{\tau}_l} = e^{-i2\pi/3} \frac{\sqrt{3}}{2} a(i\hat{x} + \hat{y}). \quad (2.22)$$

Now we will choose the phase $Z = e^{-i\pi/3}$ so that we have

$$\sum_l \boldsymbol{\tau}_l Z e^{-i\mathbf{K}\cdot\boldsymbol{\tau}_l} = e^{-i\pi} \frac{\sqrt{3}}{2} a(i\hat{x} + \hat{y}) = \frac{\sqrt{3}}{2} a(-i\hat{x} - \hat{y}). \quad (2.23)$$

Finally we get expressions for the function $T(\mathbf{k})$ and the effective Hamiltonian $H_{\mathbf{k}}$ in the vicinity of point \mathbf{K} :

$$T(\mathbf{k}) = \gamma_0 i\mathbf{k}\cdot \sum_l \boldsymbol{\tau}_l Z e^{-i\mathbf{K}\cdot\boldsymbol{\tau}_l} = \frac{\sqrt{3}}{2} a\gamma_0 (k_x - ik_y), \text{ and} \quad (2.24)$$

$$H_{\mathbf{k}} = \frac{\sqrt{3}}{2} a\gamma_0 \begin{pmatrix} 0 & k_x - ik_y \\ k_x + ik_y & 0 \end{pmatrix}. \quad (2.25)$$

It is now convenient to introduce new variable: $\hbar v_F \equiv \frac{\sqrt{3}}{2} a \gamma_0$, where $v_F \approx 10^6$ m/s since $\gamma_0 \approx 2.8$ eV [1]. Hamiltonian (2.25) now becomes

$$H_{\mathbf{k}} = \hbar v_F \left[\begin{pmatrix} 0 & 1 \\ 1 & 0 \end{pmatrix} k_x + \begin{pmatrix} 0 & -i \\ i & 0 \end{pmatrix} k_y \right], \quad (2.26)$$

that is,

$$H_{\mathbf{k}} = \hbar v_F \boldsymbol{\sigma} \cdot \mathbf{k}, \quad (2.27)$$

where $\boldsymbol{\sigma} = \sigma_x \hat{\mathbf{x}} + \sigma_y \hat{\mathbf{y}}$, while $\sigma_x = \begin{pmatrix} 0 & 1 \\ 1 & 0 \end{pmatrix}$ and $\sigma_y = \begin{pmatrix} 0 & -i \\ i & 0 \end{pmatrix}$ are the Pauli spin matrices. Here we note the remarkable property of graphene around \mathbf{K} point where electrons behave precisely like massless Dirac particles of spin 1/2 [33]! We can also find energies (eigenvalues) and wave functions (eigenvectors) from the equation $H_{\mathbf{k}} \psi_{\mathbf{k}} = E_{\mathbf{k}} \psi_{\mathbf{k}}$:

$$E_{n,\mathbf{k}} = n \cdot \hbar v_F |\mathbf{k}| = n \cdot \hbar v_F \sqrt{k_x^2 + k_y^2}, \text{ and} \quad (2.28)$$

$$\psi_{n,\mathbf{k}}(\mathbf{r}) = \langle \mathbf{r} | n\mathbf{k} \rangle = \frac{1}{L\sqrt{2}} \begin{pmatrix} n \\ e^{i\theta(\mathbf{k})} \end{pmatrix} e^{i\mathbf{k} \cdot \mathbf{r}}. \quad (2.29)$$

Here L^2 is the area of graphene, $n = 1$ ($n = -1$) denotes the conduction (valence) band, respectively, and the angle $\theta(\mathbf{k}) = \tan^{-1}(k_y/k_x)$. Further on, we note that behavior around \mathbf{K}' point is easily found if we move the wave vector origin so that $\mathbf{k} \rightarrow \mathbf{k} + \mathbf{K}'$. In that case it is more convenient to choose the phase $Z = 1$ and the Hamiltonian (2.18) turns into $H'_{\mathbf{k}} = \hbar v_F \boldsymbol{\sigma}^* \cdot \mathbf{k}$. Hamiltonian $H'_{\mathbf{k}}$ has eigenvalues: $E'_{n,\mathbf{k}} = n \cdot \hbar v_F |\mathbf{k}| = E_{n,\mathbf{k}}$ that are degenerate with eigenvalues of Hamiltonian $H_{\mathbf{k}}$ so that \mathbf{K}' point represents only an additional degree of freedom like electron spin. In other words we can limit ourself to the behavior around \mathbf{K} point if we note that each state is four fold degenerate i.e. two spin and two valley ($\mathbf{K} - \mathbf{K}'$) degenerate.

Finally, let us find the electron density and electron current density operators for Dirac electrons in graphene. To start, note that the electron momentum is $\mathbf{p} = \hbar \mathbf{k}$, which can be written as an operator in the coordinate representation $\mathbf{p} = -i\hbar \nabla$, so the Dirac Hamiltonian (2.27) can be written as: $H = -i\boldsymbol{\sigma} \cdot \nabla$. If we now describe this Dirac electron by a wave function $\psi_{\alpha}(\mathbf{r}) = \langle \mathbf{r} | \alpha \rangle$, then

the electron particle density is simply $\rho_\alpha = |\psi_\alpha(\mathbf{r})|^2$ so the density operator is

$$\rho_{op}(\mathbf{r}) = \delta(\mathbf{r} - \mathbf{r}_{op}). \quad (2.30)$$

To find the electron current density we can apply the equation of continuity: $-e \frac{\partial \rho}{\partial t} + \nabla \cdot \mathbf{j} = 0$ (here we take $e > 0$ so that $-e$ denotes the electron charge), with an equation of motion $H\psi = i\hbar \frac{\partial \psi}{\partial t}$. This yields the electron current density: $\mathbf{j}_\alpha = -ev_F \psi_\alpha(\mathbf{r})^* \boldsymbol{\sigma} \psi_\alpha(\mathbf{r})$, i.e. the current density operator:

$$\mathbf{j}_{op}(\mathbf{r}) = -ev_F \boldsymbol{\sigma} \delta(\mathbf{r} - \mathbf{r}_{op}). \quad (2.31)$$

At last, the Fourier transforms of these quantities are given by

$$\rho_{op}(\mathbf{q}) = \frac{1}{L^2} e^{-i\mathbf{q} \cdot \mathbf{r}_{op}}, \text{ and} \quad (2.32)$$

$$\mathbf{j}_{op}(\mathbf{q}) = -\frac{ev_F}{L^2} \boldsymbol{\sigma} e^{-i\mathbf{q} \cdot \mathbf{r}_{op}}. \quad (2.33)$$

2.1.3 Electron-phonon interaction

Since graphene is a 2D crystal with two atoms per basis, there are also two optical phonon branches (transverse and longitudinal) that are degenerate at energy $\hbar\omega_0 = 0.196$ eV and mostly independent of wave vector q (for long wave modes $q \ll 2\pi/a$). Let us denote by $\mathbf{u}(\mathbf{R}) = [\mathbf{u}_A(\mathbf{R}) - \mathbf{u}_B(\mathbf{R})]/\sqrt{2}$ motion of the basis atom A relative to the atom B in the unit cell at the position \mathbf{R} (see figure 2.3). If A and B were oppositely charged ions like in polar crystals, then their motion would result in the electric dipole moment i.e. electric field in the direction of the vector \mathbf{u} and strong electron-phonon interaction. However, since A and B are completely equivalent carbon atoms, graphene belongs to the class of covalent crystals, and electron-phonon interaction is considerably reduced compared to the case of polar crystals. We will also see that electron-phonon interaction in graphene acquires unusual form in the vicinity of the Dirac (\mathbf{K} and \mathbf{K}') point and we will demonstrate that optical phonon oscillation creates effective electric field that is perpendicular to the vector \mathbf{u} . That fact will lead to peculiar mixing of plasmon and optical phonon polarizations.

The rigorous calculation of electron-phonon interaction in graphene is given

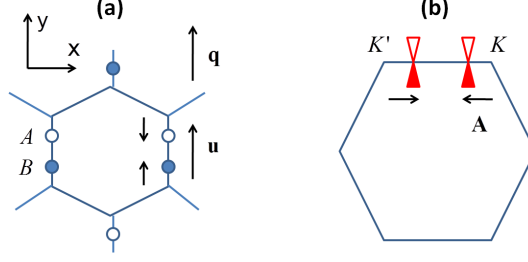


Figure 2.3: a) Atom motion in graphene during the longitudinal optical phonon oscillations. b) Motion of basis atoms described by a vector \mathbf{u} in the real space induces vector potential \mathbf{A} that moves Dirac points in the reciprocal space. Dirac point symmetry causes unusual polarization of this vector potential: $\mathbf{A} \perp \mathbf{u}$.

in references [52, 53], while we only sketch here the main steps. Let us start with the tight binding Hamiltonian (2.18)

$$H_{\mathbf{k}} = \begin{pmatrix} 0 & T(\mathbf{k}) \\ T^*(\mathbf{k}) & 0 \end{pmatrix}. \quad (2.34)$$

The effect of phonon on the electron motion can be simply found by considering the change in the hopping integral ($-\gamma_0$) with the change in the nearest neighbor distance. Let us now observe atom A at a position \mathbf{R}_A and a neighboring atom B at a position $\mathbf{R}_B = \mathbf{R}_A - \boldsymbol{\tau}_l$ whose equilibrium relative distance is simply $|\boldsymbol{\tau}_l| = b$. If we move these two atoms out of equilibrium positions, new distance is: $|\boldsymbol{\tau}_l + \mathbf{u}_A(\mathbf{R}_A) - \mathbf{u}_B(\mathbf{R}_A - \boldsymbol{\tau}_l)|$, and the leading order change in the hopping integral is

$$\begin{aligned} -\gamma &= -\gamma_0 - \frac{\partial \gamma_0(b)}{\partial b} [|\boldsymbol{\tau}_l + \mathbf{u}_A(\mathbf{R}_A) - \mathbf{u}_B(\mathbf{R}_A - \boldsymbol{\tau}_l)| - b] \\ &\approx -\gamma_0 - \frac{\partial \gamma_0(b)}{\partial b} \frac{1}{b} \boldsymbol{\tau}_l \cdot [\mathbf{u}_A(\mathbf{R}_A) - \mathbf{u}_B(\mathbf{R}_A - \boldsymbol{\tau}_l)]. \end{aligned} \quad (2.35)$$

Since we are interested in long wavelength optical phonons ($q \ll 2\pi/a$), then instead of discrete vector \mathbf{R} , we can write a continuous coordinate \mathbf{r} in the expression $\mathbf{u}(\mathbf{R}) = [\mathbf{u}_A(\mathbf{R}) - \mathbf{u}_B(\mathbf{R})]/\sqrt{2}$, i.e. we write

$$\mathbf{u}_A(\mathbf{R}_A) - \mathbf{u}_B(\mathbf{R}_A - \boldsymbol{\tau}_l) \approx \mathbf{u}_A(\mathbf{r}) - \mathbf{u}_B(\mathbf{r} - \boldsymbol{\tau}_l) \approx \mathbf{u}(\mathbf{r})\sqrt{2}. \quad (2.36)$$

Finally the change in the hopping integral (2.35), in the long wavelength limit,

is given by:

$$-\gamma \approx -\gamma_0 - \frac{\partial \gamma_0(b)}{\partial b} \frac{\sqrt{2}}{b} \boldsymbol{\tau}_l \cdot \mathbf{u}(\mathbf{r}). \quad (2.37)$$

Note here that all three neighboring carbon atoms ($l = 1, 2, 3$) see the same phonon amplitude $\mathbf{u}(\mathbf{r})$, which will not be true in the case of finite wavevector q . However this change in amplitude will come with an extra factor $q \cdot a$, so unless we are working with phonon wavevectors on the order of Brillouin zone, the long wavelength limit is a great approximation concerning the interaction between electrons and optical phonons.

We can write phonon motion $\mathbf{u}(\mathbf{r})$ as a sum over normal modes

$$\mathbf{u}(\mathbf{r}) = \sum_{\mathbf{q}, \mu} \frac{1}{\sqrt{NM}} Q_{\mathbf{q}\mu} \mathbf{e}_{\mathbf{q}\mu} e^{i\mathbf{q}\cdot\mathbf{r}}. \quad (2.38)$$

Here M is the mass of a carbon atom, $\mu = L, T$ denotes longitudinal i.e. transverse polarization, and if we define an angle $\varphi(\mathbf{q}) = \tan^{-1}(q_y/q_x)$, then polarization vectors are given by

$$\mathbf{e}_{\mathbf{q}L} = i(\cos \varphi(\mathbf{q})\hat{x} + \sin \varphi(\mathbf{q})\hat{y}), \text{ and} \quad (2.39)$$

$$\mathbf{e}_{\mathbf{q}T} = i(-\sin \varphi(\mathbf{q})\hat{x} + \cos \varphi(\mathbf{q})\hat{y}). \quad (2.40)$$

Finally we can write the phonon amplitude $Q_{\mathbf{q}\mu}$ through the creation ($b_{\mathbf{q}\mu}^\dagger$) and annihilation operators ($b_{\mathbf{q}\mu}$) as

$$Q_{\mathbf{q}\mu} = \sqrt{\frac{\hbar}{2\omega_0}} (b_{\mathbf{q}\mu} + b_{-\mathbf{q}\mu}^\dagger). \quad (2.41)$$

To find how the phonon motion $\mathbf{u}(\mathbf{r})$ influences the electrons around the \mathbf{K} point let us change the origin of wave vector as before: $\mathbf{k} \rightarrow \mathbf{k} + \mathbf{K}$. Now the

function $T(\mathbf{k})$ becomes

$$\begin{aligned}
T(\mathbf{k}, \mathbf{r}) &= \sum_l (-\gamma) Z e^{-i(\mathbf{k}+\mathbf{K})\cdot\boldsymbol{\tau}_l} \\
&= \sum_l \left(-\gamma_0 - \frac{\partial\gamma_0(b)}{\partial b} \frac{\sqrt{2}}{b} \boldsymbol{\tau}_l \cdot \mathbf{u}(\mathbf{r}) \right) Z e^{-i(\mathbf{k}+\mathbf{K})\cdot\boldsymbol{\tau}_l} \\
&\approx \sum_l \left(-\gamma_0 - \frac{\partial\gamma_0(b)}{\partial b} \frac{\sqrt{2}}{b} \boldsymbol{\tau}_l \cdot \mathbf{u}(\mathbf{r}) \right) Z e^{-i\mathbf{K}\cdot\boldsymbol{\tau}_l} (1 - i\mathbf{k} \cdot \boldsymbol{\tau}_l). \quad (2.42)
\end{aligned}$$

By looking at the leading order expansion in the phonon motion $\mathbf{u}(\mathbf{r})$ and electron wave vector \mathbf{k} we have

$$T(\mathbf{k}, \mathbf{r}) = \left(\gamma_0 i\mathbf{k} - \frac{\partial\gamma_0(b)}{\partial b} \frac{\sqrt{2}}{b} \mathbf{u}(\mathbf{r}) \right) \cdot \sum_l \boldsymbol{\tau}_l Z e^{-i\mathbf{K}\cdot\boldsymbol{\tau}_l}. \quad (2.43)$$

We recognize the first part of the expression (2.43) from the equation (2.24) for bare Dirac electrons

$$T_0(\mathbf{k}) = \gamma_0 i\mathbf{k} \cdot \sum_l \boldsymbol{\tau}_l Z e^{-i\mathbf{K}\cdot\boldsymbol{\tau}_l} = \frac{\sqrt{3}}{2} a \gamma_0 (k_x - ik_y), \quad (2.44)$$

while the other part of the sum (2.43) gives

$$\begin{aligned}
T_{e-ph}(\mathbf{r}) &= -\frac{\partial\gamma_0(b)}{\partial b} \frac{\sqrt{2}}{b} \mathbf{u}(\mathbf{r}) \cdot \sum_l \boldsymbol{\tau}_l Z e^{-i\mathbf{K}\cdot\boldsymbol{\tau}_l} \\
&= -\frac{\partial\gamma_0(b)}{\partial b} \frac{\sqrt{2}}{b} \frac{\sqrt{3}}{2} a (-iu_x - u_y). \quad (2.45)
\end{aligned}$$

With the substitution: $\hbar v_F = \frac{\sqrt{3}}{2} a \gamma_0$, expressions above transform into a simpler form

$$T_0(\mathbf{k}) = \hbar v_F (k_x - ik_y), \text{ and} \quad (2.46)$$

$$T_{e-ph}(\mathbf{r}) = \hbar v_F \frac{\partial\gamma_0(b)}{\partial b} \frac{\sqrt{2}}{b\gamma_0} (iu_x + u_y). \quad (2.47)$$

Finally since $T(\mathbf{k}, \mathbf{r}) = T_0(\mathbf{k}) + T_{e-ph}(\mathbf{r})$, we can also write for the total Hamil-

tonian $H_{\mathbf{k}} = H_{\mathbf{k}}^0 + H_{e-ph}$ where

$$H_{\mathbf{k}}^0 = \begin{pmatrix} 0 & T_0(\mathbf{k}) \\ T_0^*(\mathbf{k}) & 0 \end{pmatrix} = \hbar v_F \begin{pmatrix} 0 & k_x - ik_y \\ k_x + ik_y & 0 \end{pmatrix}, \text{ and} \quad (2.48)$$

$$H_{e-ph} = \begin{pmatrix} 0 & T_{e-ph} \\ T_{e-ph} & 0 \end{pmatrix} = \hbar v_F \frac{\partial \gamma_0(b)}{\partial b} \frac{\sqrt{2}}{b\gamma_0} \begin{pmatrix} 0 & u_y + iu_x \\ u_y - iu_x & 0 \end{pmatrix}. \quad (2.49)$$

If we introduce here the notation $\boldsymbol{\sigma} \times \mathbf{u} = \sigma_x u_y - \sigma_y u_x$, then we can write equation (2.49) in a convenient form [51, 52, 53]:

$$H_{e-ph} = -\hbar v_F \frac{\partial \gamma_0(b)}{\partial b} \frac{\sqrt{2}}{b\gamma_0} \boldsymbol{\sigma} \times \mathbf{u}(\mathbf{r}). \quad (2.50)$$

From this expression we can immediately see the unusual property of the electron-phonon interaction in the vicinity of Dirac point. Namely the total Hamiltonian $H_{\mathbf{k}}$ in the presence of the phonons, can be obtained from the bare Hamiltonian $H_{\mathbf{k}}^0 = \hbar v_F \boldsymbol{\sigma} \cdot \mathbf{k}$, by a simple substitution:

$$k_x \rightarrow k_x + K u_y, \quad (2.51)$$

$$k_y \rightarrow k_y - K u_x, \quad (2.52)$$

where $K = \frac{\partial \gamma_0(b)}{\partial b} \frac{\sqrt{2}}{b\gamma_0}$. But this is precisely equivalent to the action of the vector potential \mathbf{A} :

$$\hbar \mathbf{k} \rightarrow \hbar \mathbf{k} + e \mathbf{A}. \quad (2.53)$$

In other words influence of phonons on the electron motion is equivalent to the presence of vector potential with components: $A_x \propto u_y$ and $A_y \propto -u_x$. This will in turn lead to the unusual mixing of plasmon and optical phonon polarizations. To understand this let us assume that the phonon wave vector is oriented in the y direction ($\mathbf{q} = q\hat{y}$) and let us look at the longitudinal optical phonon motion that have $u_x = 0$ and $u_y \neq 0$ (see figure 2.3). Then the phonon influence is given by transverse vector potential since $A_x \neq 0$ and $A_y = 0$. In other words longitudinal phonon oscillation is equivalent to the transverse vector potential oscillation i.e. transverse electric field. On the other hand, since plasmons are collective charge density oscillations, accompanied by a longitudinal electric field, there won't be any interaction between plasmon

and longitudinal optical phonon. We will further show that there is a strong interaction of plasmon and transverse optical phonon which is a very counter intuitive result from the perspective of polar crystals.

The simplest way to analyze the electron-phonon interaction in graphene is to show how the phonon amplitude couples to the electron current density. In that regards let us take electron-phonon Hamiltonian (2.50) and write expansion of the phonon motion $\mathbf{u}(\mathbf{r})$ over the normal modes from equation (2.38) to obtain:

$$H_{e-ph} = -\hbar v_F \frac{\partial \gamma_0(b)}{\partial b} \frac{\sqrt{2}}{b \gamma_0} \frac{1}{\sqrt{NM}} \sum_{\mathbf{q}, \mu} e^{i\mathbf{q}\cdot\mathbf{r}} \boldsymbol{\sigma} \times \mathbf{e}_{\mathbf{q}\mu} Q_{\mathbf{q}\mu}. \quad (2.54)$$

Here we recognize the current density operator $\mathbf{j}_{\mathbf{q}}^\dagger = -\frac{ev_F}{L^2} \boldsymbol{\sigma} e^{i\mathbf{q}\cdot\mathbf{r}}$ from equation (2.33), and if we introduce the factor $F = \frac{\hbar}{e} \frac{\partial \gamma_0(b)}{\partial b} \frac{\sqrt{2}}{b \gamma_0} \frac{1}{\sqrt{NM}}$, we can finally write for the electron-phonon interaction Hamiltonian:

$$H_{e-ph} = L^2 F \sum_{\mathbf{q}, \mu} \mathbf{j}_{\mathbf{q}}^\dagger \times \mathbf{e}_{\mathbf{q}\mu} Q_{\mathbf{q}\mu}. \quad (2.55)$$

A more convenient way to write electron-phonon interaction is to show how the phonon amplitude couples to the electron density. In that respect, let us define the quantities:

$$E_{\mathbf{q}L} \equiv e_{\mathbf{q}L} \cdot \hat{y} + ie_{\mathbf{q}L} \cdot \hat{x} = i \sin \varphi(\mathbf{q}) - \cos \varphi(\mathbf{q}) = -e^{-i\varphi(\mathbf{q})}, \text{ and} \quad (2.56)$$

$$E_{\mathbf{q}T} \equiv e_{\mathbf{q}T} \cdot \hat{y} + ie_{\mathbf{q}T} \cdot \hat{x} = i \cos \varphi(\mathbf{q}) + \sin \varphi(\mathbf{q}) = ie^{-i\varphi(\mathbf{q})}. \quad (2.57)$$

Then by using the normal mode expansion (2.38) we obtain

$$u_y + iu_x = \sum_{\mathbf{q}, \mu} \frac{1}{\sqrt{NM}} Q_{\mathbf{q}\mu} (e_{\mathbf{q}\mu} \cdot \hat{y} + ie_{\mathbf{q}\mu} \cdot \hat{x}) e^{i\mathbf{q}\cdot\mathbf{r}} = \sum_{\mathbf{q}, \mu} \frac{1}{\sqrt{NM}} Q_{\mathbf{q}\mu} E_{\mathbf{q}\mu} e^{i\mathbf{q}\cdot\mathbf{r}}. \quad (2.58)$$

Finally the electron-phonon interaction Hamiltonian (2.49) can be written as:

$$H_{e-ph} = \hbar v_F \frac{\partial \gamma_0(b)}{\partial b} \frac{\sqrt{2}}{b \gamma_0} \sum_{\mathbf{q}, \mu} \frac{1}{\sqrt{NM}} Q_{\mathbf{q}\mu} \begin{pmatrix} 0 & E_{\mathbf{q}\mu} \\ E_{\mathbf{q}\mu}^* & 0 \end{pmatrix} e^{i\mathbf{q}\cdot\mathbf{r}}. \quad (2.59)$$

If we now define

$$g \equiv \hbar v_F \frac{\partial \gamma_0(b)}{\partial b} \frac{\sqrt{2}}{b \gamma_0} \frac{1}{\sqrt{NM}}, \text{ and} \quad (2.60)$$

$$M_{\mathbf{q}\mu} \equiv \begin{pmatrix} 0 & E_{\mathbf{q}\mu} \\ E_{\mathbf{q}\mu}^* & 0 \end{pmatrix}, \quad (2.61)$$

then we can write electron-phonon interaction as a coupling between phonon amplitude $Q_{\mathbf{q}\mu}$ and electron density operator $\rho_{\mathbf{q}}^\dagger$ from equation (2.32) as:

$$H_{e-ph} = L^2 \sum_{\mathbf{q}, \mu} g M_{\mathbf{q}\mu} \rho_{\mathbf{q}}^\dagger Q_{\mathbf{q}\mu}. \quad (2.62)$$

Formula (2.55) and (2.62) are equivalent. However, the response of the system to the interaction Hamiltonian (2.55) is most easily described by utilizing the current-current response function while the response to the interaction Hamiltonian (2.62) is most easily described by the density-density response function.

2.2 Response functions

In this section we present response functions which describe response of our system to an external perturbation. Specifically we calculate graphene's conductivity, density-density, and current-current response functions in the weak coupling approximation i.e. linear response theory. These three functions are all connected by simple relations, however it will be more convenient to use one or another depending on the specific nature of the problem being studied.

2.2.1 Conductivity

Semiclassical model - Drude conductivity

If we are only interested in the response of the graphene under the influence of external electromagnetic field, we can simply calculate the conductivity function $\sigma(\omega)$. The semiclassical model gives a simple relation for the Drude conductivity [38]

$$\sigma_D(\omega) = e^2 \int 4 \frac{d\mathbf{k}}{4\pi^2} \frac{\mathbf{v}(\mathbf{k})\mathbf{v}(\mathbf{k})}{1/\tau - i\omega} \left(-\frac{\partial f}{\partial E} \right)_{E=E(\mathbf{k})}, \quad (2.63)$$

where τ is the relaxation time, $\mathbf{v}(\mathbf{k}) = \frac{1}{\hbar} \frac{\partial E(\mathbf{k})}{\partial \mathbf{k}}$ is the electron velocity, $f(E) = \frac{1}{e^{(E-\mu)/kT} + 1}$ is the Fermi-Dirac distribution function, and factor 4 stands for two

spin and two valley degeneracy. Semiclassical model is simply a generalization of the Drude model for free electrons to the case of an arbitrary band structure $E(\mathbf{k})$, however we will see that it can describe lot of interesting phenomena in a qualitatively correct way. At zero temperature one has $-\partial f/\partial E = \delta(E - \mu)$ and it is straightforward to show that for the case of Dirac electrons in graphene $H_{\mathbf{k}} = \hbar v_F \boldsymbol{\sigma} \cdot \mathbf{k}$, the Drude conductivity is given by

$$\sigma_D(\omega) = e^2 \frac{\mu}{\pi \hbar^2} \frac{1}{1/\tau - i\omega}. \quad (2.64)$$

It is a slightly more tedious task to show that at finite temperature T one has

$$\sigma_D(\omega) = e^2 \frac{2kT}{\pi \hbar^2} \ln \left(2 \cosh \frac{\mu}{2kT} \right) \frac{1}{1/\tau - i\omega}. \quad (2.65)$$

Fermi's golden rule - interband conductivity

The semiclassical model has a serious limitation since it cannot describe transitions between different bands [38], which is particularly important in graphene that has zero band-gap between valence and conduction bands. To take into account these interband transitions we will calculate the response of graphene to an external electric field, in the first order perturbation theory (using the Fermi's golden rule).

Let us imagine that an electromagnetic plane wave of frequency ω is incident under the normal angle onto the graphene sheet. We can choose the gauge so that the scalar potential $\varphi = 0$, while the vector potential $\mathbf{A} = \mathbf{A}_0 e^{-i\omega t}$, so that the electric field is given by $\mathbf{E} = -\frac{\partial \mathbf{A}}{\partial t} = i\omega \mathbf{A} = \mathbf{E}_0 e^{-i\omega t}$, and $\mathbf{E}_0 = i\omega \mathbf{A}_0$. Electrons in graphene are described by a Dirac Hamiltonian (2.27) $H_0 = \hbar v_F \boldsymbol{\sigma} \cdot \mathbf{k} = v_F \boldsymbol{\sigma} \cdot \mathbf{p}$, where \mathbf{p} is the graphene's electron momentum so that the interaction with the vector potential is simply described by a substitution $\mathbf{p} \rightarrow \mathbf{p} + e\mathbf{A}$. In other words, the total Hamiltonian in the presence of electromagnetic field can be written as $H = v_F \boldsymbol{\sigma} \cdot (\mathbf{p} + e\mathbf{A}) = H_0 + H_{int}$, where the interaction part of the Hamiltonian is given by

$$H_{int} = e v_F \boldsymbol{\sigma} \cdot \mathbf{A} = \frac{e v_F}{i\omega} \boldsymbol{\sigma} \cdot \mathbf{E}_0 e^{-i\omega t}. \quad (2.66)$$

Here we have kept only the time dependent part ($e^{-i\omega t}$) responsible for the absorption process. Then the Fermi's golden rule [68] gives the probability for

a transition from an initial state i to the final state f , with an absorption of a photon:

$$\frac{dw_{i \rightarrow f}}{dt} = \frac{2\pi}{\hbar} |\langle i | H_{int} | f \rangle|^2 \delta(\hbar\omega_{if} - \hbar\omega) f_i (1 - f_f). \quad (2.67)$$

The total power absorbed from the incident wave can be written in two ways. First, one can write

$$P_a = \sum_{i,f} \hbar\omega \frac{dw_{i \rightarrow f}}{dt}. \quad (2.68)$$

On the other hand, since $\mathbf{j}(\omega) = \sigma(\omega)\mathbf{E}(\omega)$, one can write (for harmonic fields) [67]

$$P_a = 2\Re \int \mathbf{j}(\omega) \cdot \mathbf{E}^*(\omega) d\mathbf{r} = 2\Re \sigma(\omega) |\mathbf{E}_0|^2 L^2, \quad (2.69)$$

where L^2 is the area of graphene sheet, and we used the fact that $\mathbf{E}(\omega) = \mathbf{E}_0$ is uniform along the graphene plane for the case of normal incident wave. Finally we have

$$\Re \sigma(\omega) = \frac{\hbar\omega}{2|\mathbf{E}_0|^2 L^2} \sum_{i,f} \frac{2\pi}{\hbar} |\langle i | H_{int} | f \rangle|^2 \delta(\hbar\omega_{if} - \hbar\omega) f_i (1 - f_f). \quad (2.70)$$

Now, let us denote the initial (final) state of the electron by a band index n (n') and a wave vector \mathbf{k} (\mathbf{k}') i.e. $|i\rangle = |n\mathbf{k}\rangle$ ($|f\rangle = |n'\mathbf{k}'\rangle$). Without loss of generality we can assume that the electric field is polarized along the x direction: $\mathbf{E}_0 = E_0 \hat{\mathbf{x}}$. Then we can write for the matrix element:

$$\langle i | H_{int} | f \rangle = \frac{e v_F}{i\omega} E_0 \langle n'\mathbf{k}' | \sigma_x | n\mathbf{k} \rangle. \quad (2.71)$$

Further on, by using explicit form (2.29) for the Dirac electron wave function $\psi_{n,\mathbf{k}}$, it is simple to show that

$$\langle n'\mathbf{k}' | \sigma_x | n\mathbf{k} \rangle = \int \psi_{n',\mathbf{k}'}^*(\mathbf{r}) \sigma_x \psi_{n,\mathbf{k}}(\mathbf{r}) d\mathbf{r} = \frac{1}{2} \delta_{\mathbf{k},\mathbf{k}'} (n e^{-i\theta_{\mathbf{k}}} + n' e^{i\theta_{\mathbf{k}}}), \quad (2.72)$$

so we obtain expressions for the matrix element

$$|\langle i | H_{int} | f \rangle|^2 = \frac{e^2 v_F^2}{\omega^2} |E_0|^2 \delta_{\mathbf{k},\mathbf{k}'} \frac{1}{2} (1 + nn' \cos 2\theta_{\mathbf{k}}), \quad (2.73)$$

and conductivity

$$\Re\sigma(\omega) = \frac{\hbar\omega}{2} 4 \sum_{n,n'} \frac{1}{4\pi^2} \int k dk \int d\theta_{\mathbf{k}} \frac{2\pi}{\hbar} \frac{e^2 v_F^2}{\omega^2} \frac{1}{2} (1 + nn' \cos 2\theta_{\mathbf{k}}) \times \delta(n'\hbar v_F k - n\hbar v_F k - \hbar\omega) f_{nk}(1 - f_{n'k}), \quad (2.74)$$

where we also took into account 2 spin and 2 valley degeneracy. We now take into account only (interband) transitions between conduction and valence bands, because the intraband transitions are already taken into account by the Drude conductivity. After lengthy but straightforward calculation, one obtains simple expression for the real part of the conductivity

$$\Re\sigma(\omega) = \frac{e^2}{4\hbar} f(-\hbar\omega/2)[1 - f(\hbar\omega/2)]. \quad (2.75)$$

It is instructive to look at this result at zero temperature

$$\Re\sigma(\omega) = \frac{e^2}{4\hbar} \theta(\hbar\omega - 2\mu). \quad (2.76)$$

Here $\theta(x)$ is a simple step function [$\theta(x < 0) = 0$ and $\theta(x > 0) = 1$]. The real part of the conductivity provides us with absorption of the electromagnetic field incident on a graphene sheet. We see that there is no absorption for $\hbar\omega < 2\mu$ which is result of the Pauli exclusion principle. On the other hand above this threshold, when $\hbar\omega > 2\mu$ one will have uniform absorption. Since the incident energy flux is given by $W_i = 2|E_0|^2/\mu_0 c$ (see reference [67]), and the absorbed energy per unit time per unit area is given by $W_a = P_a/L^2 = 2\Re\sigma(\omega)|E_0|^2$ (see equation (2.69)), the absorption coefficient can be written as

$$|a|^2 = \frac{W_a}{W_i} = \frac{\mu_0 c e^2}{4\hbar} = 2.3\%. \quad (2.77)$$

This result has been confirmed by experiment [37]. Further on, note that if we include the emission process, then we obtain the following expression for the

conductivity:

$$\begin{aligned}\Re\sigma(\omega) &= \frac{e^2}{4\hbar}[f(-\hbar\omega/2)[1 - f(\hbar\omega/2)] - [1 - f(-\hbar\omega/2)]f(\hbar\omega/2)] \\ &= \frac{e^2}{4\hbar}[f(-\hbar\omega/2) - f(\hbar\omega/2)].\end{aligned}\quad (2.78)$$

Finally we can obtain the imaginary part of the conductivity by using the Kramers-Kronig relations [56]:

$$\begin{aligned}\Im\sigma(\omega) &= -\frac{2\omega}{\pi}\mathcal{P}\int_0^\infty\frac{\Re\sigma(\omega')}{\omega'^2 - \omega^2}d\omega' \\ &= -\frac{e^2}{4\hbar}\frac{4\hbar\omega}{\pi}\mathcal{P}\int_0^\infty\frac{f(-\epsilon) - f(\epsilon)}{(2\epsilon)^2 - (\hbar\omega)^2}d\epsilon.\end{aligned}\quad (2.79)$$

It is convenient to introduce the following function:

$$G(\epsilon) \equiv f(-\epsilon) - f(\epsilon) = \frac{\sinh\frac{\epsilon}{kT}}{\cosh\frac{\mu}{kT} + \cosh\frac{\epsilon}{kT}}.\quad (2.80)$$

Then, we can simply write for the total interband conductivity (see also [61]):

$$\sigma_I(\omega) = \frac{e^2}{4\hbar}\left(G(\omega/2) + i\frac{4\hbar\omega}{\pi}\int_0^\infty\frac{G(\epsilon) - G(\hbar\omega/2)}{(2\epsilon)^2 - (\hbar\omega)^2}d\epsilon\right).\quad (2.81)$$

In the last expression, we took into account that principal value of the integral with $G(\hbar\omega/2)$ equals to zero, which removes singularities from the integral in the imaginary part of the conductivity.

2.2.2 Density-density response function

We now proceed to a more formal, but powerful, aspect of linear response theory by looking into the density-density response function. In the last section we assumed that there is no spatial dependence of external perturbation and calculated only frequency dependence of the conductivity. Let us assume that graphene is placed in an external scalar potential of arbitrary spatial and time dependence

$$\varphi_{ext}(\mathbf{r}, t) = \int e^{-i\omega t}d\omega\sum_{\mathbf{q}}e^{i\mathbf{q}\cdot\mathbf{r}}\varphi_{ext}(\mathbf{q}, \omega).\quad (2.82)$$

Now, scalar potential simply couples to the electron charge density so one can write the interaction Hamiltonian [56]

$$H_{int} = \int e^{-i\omega t} d\omega L^2 \sum_{\mathbf{q}} (-e\varphi_{ext}(\mathbf{q}, \omega)) \rho_{\mathbf{q}}^{\dagger}. \quad (2.83)$$

We now assume the weak coupling between the system (electron density) and a probe (external potential) so that we can focus on a single (\mathbf{q}, ω) component. The induced electron particle density is then given by

$$\langle \rho_{ind}(\mathbf{q}, \omega) \rangle = \chi(\mathbf{q}, \omega) (-e\varphi_{ext}(\mathbf{q}, \omega)), \quad (2.84)$$

where the density-density response function is given by [56]

$$\chi(\mathbf{q}, \omega) = L^2 \sum_{a,b} \frac{e^{-\beta E_b}}{Z} |\langle a | \rho_{\mathbf{q}}^{\dagger} | b \rangle|^2 \left(\frac{1}{\hbar\omega - \hbar\omega_{ab} + i\eta} - \frac{1}{\hbar\omega + \hbar\omega_{ab} + i\eta} \right). \quad (2.85)$$

Here $Z = \sum_b e^{-\beta E_b}$ is the partition function, and $\hbar\omega_{ab} = E_a - E_b$. Further on $|a\rangle$, and E_a are exact many body state, and energy of the system in the presence of the perturbation. In other words we can write $H|a\rangle = E_a|a\rangle$ where $H = H_0 + H_{int}$ is the total system Hamiltonian given by the sum of the Hamiltonian in the absence of perturbation (H_0) and the interaction term (H_{int}). Equation (2.85) is exact in the limit of weak coupling (i.e. linear response), however one first needs to find the exact eigenstates of the total Hamiltonian H which is not an easy task. We shall deal with this issue by working in the self-consistent approximation i.e. by introducing simple, yet powerful, concept of screening. In that regard let us note that the induced charge density $\langle \rho_{ind}(\mathbf{q}, \omega) \rangle$ will be accompanied by an scalar potential $\varphi_{ind}(\mathbf{q}, \omega)$ which can act back on the electrons through the interaction Hamiltonian (2.83). In other words, instead of equation (2.84) we should write the self-consistent equation for the total induced particle density

$$\langle \rho_{ind}(\mathbf{q}, \omega) \rangle = \chi(\mathbf{q}, \omega) (-e\varphi_{ext}(\mathbf{q}, \omega) - e\varphi_{ind}(\mathbf{q}, \omega)). \quad (2.86)$$

However, $\chi(\mathbf{q}, \omega)$ is now the screened density-density response function which is again given by the equation (2.85), only $|a, b\rangle$ are now simply the eigenstates of the noninteracting Hamiltonian H_0 . This is the lowest order approximation

which can also be traced down to the random phase approximation. For a system of Dirac electrons, described by a wave functions $\psi_{n,\mathbf{k}}$ given by equation (2.29), one then obtains for the screened response function [56]:

$$\begin{aligned}\chi(\mathbf{q}, \omega) &= \frac{1}{L^2} 4 \sum_{nn'\mathbf{k}} |\langle n'\mathbf{k} + \mathbf{q} | e^{i\mathbf{q}\cdot\mathbf{r}} | n\mathbf{k} \rangle|^2 \frac{f_{n\mathbf{k}} - f_{n'\mathbf{k}+\mathbf{q}}}{\hbar\omega - E_{n'\mathbf{k}+\mathbf{q}} + E_{n\mathbf{k}} + i\eta} \\ &= \frac{1}{L^2} 4 \sum_{nn'\mathbf{k}} \frac{1}{2} [1 + nn' \cos(\theta_{\mathbf{k}+\mathbf{q}} - \theta_{\mathbf{k}})] \frac{f_{n\mathbf{k}} - f_{n'\mathbf{k}+\mathbf{q}}}{\hbar\omega - E_{n'\mathbf{k}+\mathbf{q}} + E_{n\mathbf{k}} + i\eta}.\end{aligned}\quad (2.87)$$

We will be particularly interested in the dielectric function of this system so we need to find the relation between the scalar potential φ_{ind} and the induced surface charge density $-e\langle\rho_{ind}(\mathbf{r}, t)\rangle = -e\langle\rho_{ind}(\mathbf{q}, \omega)\rangle e^{i\mathbf{q}\cdot\mathbf{r}} e^{-i\omega t}$. Let us define here the vector $\mathbf{r} = x\hat{\mathbf{x}} + y\hat{\mathbf{y}}$ which lies in the graphene plane (located at $z = 0$) while z axis is perpendicular to graphene plane. Further on we assume graphene is sitting in between two dielectrics of permittivities ϵ_{r1} ($z < 0$) and ϵ_{r2} ($z > 0$). If we work in the electrostatic approximation ($q \gg \omega/c$) then the scalar potential induced by the surface charge density located at the plane $z = 0$ is simply given by

$$\varphi_{ind}(\mathbf{r}, z, t) = \varphi_{ind}(\mathbf{q}, \omega) e^{i\mathbf{q}\cdot\mathbf{r} - q|z|} e^{-i\omega t}.\quad (2.88)$$

The electric field is given by $\mathbf{E} = -\nabla\varphi$. We can now separate the electric field $\mathbf{E} = \mathbf{E}_{\mathbf{r}} + E_z\hat{\mathbf{z}}$ into component along the graphene plane $\mathbf{E}_{\mathbf{r}} = -\nabla_{\mathbf{r}}\varphi$ which is given by expression

$$\mathbf{E}_{\mathbf{r}}^{ind}(\mathbf{r}, z, t) = -\varphi_{ind}(\mathbf{q}, \omega) i\mathbf{q} e^{i\mathbf{q}\cdot\mathbf{r} - q|z|} e^{-i\omega t},\quad (2.89)$$

and component perpendicular to the graphene plane $E_z = -\partial\varphi/\partial z$ which is given by expressions

$$\mathbf{E}_z^{ind}(\mathbf{r}, z > 0, t) = \varphi_{ind}(\mathbf{q}, \omega) i q e^{i\mathbf{q}\cdot\mathbf{r} - qz} e^{-i\omega t},\quad (2.90)$$

$$\mathbf{E}_z^{ind}(\mathbf{r}, z < 0, t) = -\varphi_{ind}(\mathbf{q}, \omega) i q e^{i\mathbf{q}\cdot\mathbf{r} + qz} e^{-i\omega t}.\quad (2.91)$$

Further on, the Gauss law can be written as a boundary condition across the

graphene plane as [67]

$$\begin{aligned} -e\langle\rho_{ind}(\mathbf{r}, t)\rangle &= [\mathbf{D}^{ind}(\mathbf{r}, z = 0^+, t) - \mathbf{D}^{ind}(\mathbf{r}, z = 0^-, t)] \cdot \hat{\mathbf{z}} \\ &= \epsilon_0\epsilon_{r1}E_z^{ind}(\mathbf{r}, z = 0^+, t) - \epsilon_0\epsilon_{r2}E_z^{ind}(\mathbf{r}, z = 0^-, t). \end{aligned} \quad (2.92)$$

Then by using the decomposition into Fourier components and equations (2.90) and (2.91) we obtain desired relation between the induced charge density and corresponding induced scalar potential:

$$-e\langle\rho_{ind}(\mathbf{q}, \omega)\rangle = q\varphi_{ind}(\mathbf{q}, \omega)2\bar{\epsilon}_r\epsilon_0. \quad (2.93)$$

Here $\bar{\epsilon}_r = (\epsilon_{r1} + \epsilon_{r2})/2$, and we can introduce the external charge density corresponding to the external potential by the same relation

$$-e\rho_{ext}(\mathbf{q}, \omega) = q\varphi_{ext}(\mathbf{q}, \omega)2\bar{\epsilon}_r\epsilon_0. \quad (2.94)$$

Let us now define the graphene dielectric function $\epsilon(\mathbf{q}, \omega)$ as [56]:

$$\frac{\epsilon(\mathbf{q}, \omega)}{\bar{\epsilon}_r} = \frac{\rho_{ext}(\mathbf{q}, \omega)}{\rho_{ext}(\mathbf{q}, \omega) + \langle\rho_{ind}(\mathbf{q}, \omega)\rangle}. \quad (2.95)$$

Then from equations (2.86), (2.93) and (2.94) we obtain

$$\frac{\epsilon(\mathbf{q}, \omega)}{\bar{\epsilon}_r} = 1 - \frac{e^2}{2\bar{\epsilon}_r\epsilon_0q}\chi(\mathbf{q}, \omega). \quad (2.96)$$

Note that the zero of dielectric function ($\epsilon(\mathbf{q}, \omega) = 0$) defines the collective electron oscillation (plasmon) which is the core subject of this thesis.

Finally let us find the relation between density-density response function $\chi(\mathbf{q}, \omega)$ and conductivity $\sigma(\mathbf{q}, \omega)$. If we introduce the total scalar potential $\varphi_{tot} = \varphi_{ext} + \varphi_{ind}$, then by using equation (2.86), we can write the induced surface charge density as $-e\langle\rho_{ind}(\mathbf{q}, \omega)\rangle = \chi(\mathbf{q}, \omega)e^2\varphi_{tot}(\mathbf{q}, \omega)$. On the other hand Ohm's law gives the induced surface current density $\langle\mathbf{j}_{ind}(\mathbf{q}, \omega)\rangle = \sigma(\mathbf{q}, \omega)\mathbf{E}_r^{tot}(\mathbf{q}, \omega)$, while the electric field can be found from equation (2.89): $\mathbf{E}_r^{tot}(\mathbf{q}, \omega) = -\varphi_{tot}(\mathbf{q}, \omega)i\mathbf{q}$. Finally, equation of continuity can be written with Fourier components as $-e\langle\rho_{ind}(\mathbf{q}, \omega)\rangle = \mathbf{q} \cdot \langle\mathbf{j}_{ind}(\mathbf{q}, \omega)\rangle/\omega$, so we obtain desired

relation:

$$\sigma(\mathbf{q}, \omega) = i \frac{\omega e^2}{q^2} \chi(\mathbf{q}, \omega). \quad (2.97)$$

Note however that $\sigma(\mathbf{q}, \omega)$ refers only to the longitudinal conductivity since the scalar potential alone is not enough to describe the transverse fields.

2.2.3 Current-current response function

In the last section we described response to the external scalar potential which we now supplement by calculating response to the external vector potential. Let us then start with the Hamiltonian (2.27) describing free Dirac particles: $H_0 = v_F \boldsymbol{\sigma} \cdot \mathbf{p}$, where \mathbf{p} is the electron momentum. In the presence of external vector potential $\mathbf{A}_{ext}(\mathbf{r}, t)$, one can write for the total Hamiltonian $H = v_F \boldsymbol{\sigma} \cdot (\mathbf{p} + e \mathbf{A}_{ext}(\mathbf{r}, t)) = H_0 + H_{int}$, where the interaction part of the Hamiltonian is given by: $H_{int} = e v_F \boldsymbol{\sigma} \cdot \mathbf{A}_{ext}(\mathbf{r}, t)$. We can now decompose vector potential into Fourier components to obtain:

$$H_{int} = \sum_{\mathbf{q}} e^{i\mathbf{q} \cdot \mathbf{r}} e v_F \boldsymbol{\sigma} \cdot \mathbf{A}_{ext}(\mathbf{q}, t), \quad (2.98)$$

then by using the current density operator from equation (2.33) we can write

$$H_{int} = -L^2 \sum_{\mathbf{q}} \mathbf{j}_{\mathbf{q}}^\dagger \cdot \mathbf{A}_{ext}(\mathbf{q}, t). \quad (2.99)$$

It is now convenient to introduce the longitudinal ($V_L = \mathbf{V} \cdot \mathbf{e}_{\mathbf{q}L}^*$) and transverse ($V_T = \mathbf{V} \cdot \mathbf{e}_{\mathbf{q}T}^*$) vector components by using the polarization vectors from equations (2.39) and (2.40). We can now write the interaction Hamiltonian

$$\begin{aligned} H_{int} &= -L^2 \sum_{\mathbf{q}, \mu} j_{\mathbf{q}, \mu}^\dagger \cdot A_{ext, \mu}(\mathbf{q}, t) \\ &= \int e^{-i\omega t} d\omega (-L^2) \sum_{\mathbf{q}, \mu} j_{\mathbf{q}, \mu}^\dagger \cdot A_{ext, \mu}(\mathbf{q}, \omega). \end{aligned} \quad (2.100)$$

Finally, by assuming the weak coupling between the external probe and our system, precisely like in the last section, we obtain the induced current density:

$$\langle j_{ind, \mu}(\mathbf{q}, \omega) \rangle = \chi_\mu(\mathbf{q}, \omega) (-A_{ext, \mu}(\mathbf{q}, \omega)). \quad (2.101)$$

Here the current-current response function is given by [56]

$$\chi_\mu(\mathbf{q}, \omega) = L^2 \sum_{a,b} \frac{e^{-\beta E_b}}{Z} |\langle a | j_{\mathbf{q},\mu}^\dagger | b \rangle|^2 \left(\frac{1}{\hbar\omega - \hbar\omega_{ab} + i\eta} - \frac{1}{\hbar\omega + \hbar\omega_{ab} + i\eta} \right). \quad (2.102)$$

We can now use the free electron states to write the screened function:

$$\chi_\mu(\mathbf{q}, \omega) = L^2 4 \sum_{nn'\mathbf{k}} |\langle n'\mathbf{k} + \mathbf{q} | j_{\mathbf{q},\mu}^\dagger | n\mathbf{k} \rangle|^2 \frac{f_{n\mathbf{k}} - f_{n'\mathbf{k}+\mathbf{q}}}{\hbar\omega - E_{n'\mathbf{k}+\mathbf{q}} + E_{n\mathbf{k}} + i\eta}. \quad (2.103)$$

At last, by using the exact form of the electron wave function from equation (2.29), we obtain different expressions for the longitudinal and transverse current-current response functions:

$$\chi_L(\mathbf{q}, \omega) = \frac{e^2 v_F^2}{L^2} 4 \sum_{nn'\mathbf{k}} \frac{1}{2} [1 + nn' \cos(\theta_{\mathbf{k}} + \theta_{\mathbf{k}+\mathbf{q}})] \frac{f_{n\mathbf{k}} - f_{n'\mathbf{k}+\mathbf{q}}}{\hbar\omega - E_{n'\mathbf{k}+\mathbf{q}} + E_{n\mathbf{k}} + i\eta}, \quad (2.104)$$

$$\chi_T(\mathbf{q}, \omega) = \frac{e^2 v_F^2}{L^2} 4 \sum_{nn'\mathbf{k}} \frac{1}{2} [1 - nn' \cos(\theta_{\mathbf{k}} + \theta_{\mathbf{k}+\mathbf{q}})] \frac{f_{n\mathbf{k}} - f_{n'\mathbf{k}+\mathbf{q}}}{\hbar\omega - E_{n'\mathbf{k}+\mathbf{q}} + E_{n\mathbf{k}} + i\eta}. \quad (2.105)$$

Note here that expressions (2.104) and (2.105) actually diverge if we use Dirac states (2.29) instead of actual electron states in graphene limited by some band cut-off. However, this subtlety can be easily solved by subtracting from $\chi_L(\mathbf{q}, \omega)$ [$\chi_T(\mathbf{q}, \omega)$] the value $\chi_L(\mathbf{q}, \omega = 0)$ [$\chi_T(\mathbf{q} \rightarrow 0, \omega = 0)$] to take into account that there is no current response to the longitudinal [transverse] time [time and space] independent vector potential, see [54, 55] for details.

Let us also find relation between the conductivity and the current-current response function. Note that the electric field is given by $\mathbf{E} = -\partial\mathbf{A}/\partial t$ so that $\mathbf{E}(\mathbf{q}, \omega) = i\omega\mathbf{A}(\mathbf{q}, \omega)$. Then we can write equation (2.101) as $\langle j_{ind,\mu}(\mathbf{q}, \omega) \rangle = \chi_\mu(\mathbf{q}, \omega) \frac{i}{\omega} E_{ext,\mu}(\mathbf{q}, \omega)$. In other words desired relation is simply:

$$\sigma_\mu(\mathbf{q}, \omega) = \frac{i}{\omega} \chi_\mu(\mathbf{q}, \omega). \quad (2.106)$$

Note here that longitudinal conductivity $\sigma_L(\mathbf{q}, \omega)$ (describing response of a system to the longitudinal field) is generally different from the transverse conductivity $\sigma_T(\mathbf{q}, \omega)$ (describing response of a system to the transverse field), unless we are working in the limit of small wave vectors ($q \rightarrow 0$).

2.2.4 Fluctuation-dissipation theorem

In this section we derive relation between current-current correlation function and the current-current response function at finite temperature, which is given by the fluctuation-dissipation theorem. We will use this result later to calculate the radiative heat transfer between two graphene sheets.

We start with the current-current correlation function:

$$K_\mu(\mathbf{r}, t, \mathbf{r}', t') = \langle j_\mu(\mathbf{r}, t) j_\mu^\dagger(\mathbf{r}', t') \rangle. \quad (2.107)$$

Due to translational invariance in space and time we can write $K_\mu(\mathbf{r}, t, \mathbf{r}', t') = K_\mu(\mathbf{r} - \mathbf{r}', t - t') = K_\mu(\mathbf{d}, \tau)$, where we have denoted by: $\mathbf{d} = \mathbf{r} - \mathbf{r}'$ and $\tau = t - t'$. Then the Fourier transforms from the space and time domains are respectively given by

$$K_\mu(\mathbf{q}, \tau) = \frac{1}{L^2} \int K_\mu(\mathbf{d}, \tau) e^{-i\mathbf{q}\cdot\mathbf{d}} d\mathbf{d}, \quad (2.108)$$

$$K_\mu(\mathbf{q}, \omega) = \frac{1}{2\pi} \int K_\mu(\mathbf{q}, \tau) e^{i\omega\tau} d\tau. \quad (2.109)$$

It will be more convenient for us to use these relations in a slightly different form. In that regards let us use relations (2.108) and (2.109) with translational invariance in space and time, respectively, to show that

$$\begin{aligned} \langle j_\mu(\mathbf{q}) j_\mu^\dagger(\mathbf{q}') \rangle &= \frac{1}{L^4} \int \int \langle j_\mu(\mathbf{r}) j_\mu^\dagger(\mathbf{r}') \rangle e^{-i\mathbf{q}\cdot\mathbf{r}} e^{i\mathbf{q}'\cdot\mathbf{r}'} d\mathbf{r} d\mathbf{r}' \\ &= \frac{1}{L^2} \int e^{i(\mathbf{q}'-\mathbf{q})\cdot\mathbf{r}'} d\mathbf{r}' \frac{1}{L^2} \int K_\mu(\mathbf{r} - \mathbf{r}') e^{-i\mathbf{q}\cdot(\mathbf{r}-\mathbf{r}')} d\mathbf{r} \\ &= \delta_{\mathbf{q},\mathbf{q}'} K_\mu(\mathbf{q}), \end{aligned} \quad (2.110)$$

$$\begin{aligned} \langle j_\mu(\omega) j_\mu^\dagger(\omega') \rangle &= \frac{1}{4\pi^2} \int \int \langle j_\mu(t) j_\mu^\dagger(t') \rangle e^{i\omega t} e^{-i\omega' t'} dt dt' \\ &= \frac{1}{2\pi} \int e^{i(\omega-\omega')t'} dt' \frac{1}{2\pi} \int K_\mu(t-t') e^{-i\omega(t-t')} dt \\ &= \delta(\omega - \omega') K_\mu(\omega). \end{aligned} \quad (2.111)$$

Relations (2.110) and (2.111) simply state that there is no correlation between different \mathbf{q} or different ω components. We can join these two relations in a

single one

$$\langle j_\mu(\mathbf{q}, \omega) j_\mu^\dagger(\mathbf{q}', \omega') \rangle = \delta_{\mathbf{q}, \mathbf{q}'} \delta(\omega - \omega') K_\mu(\mathbf{q}, \omega). \quad (2.112)$$

To find the $K_\mu(\mathbf{q}, \omega)$ let us note that evolution of current operator, in the Heisenberg picture, is given by $j_\mu(\mathbf{q}, \tau) = e^{iH\tau/\hbar} j_\mu^\dagger(\mathbf{q}, 0) e^{-iH\tau/\hbar}$. Now we can write

$$\begin{aligned} K_\mu(\mathbf{q}, \tau) &= \langle j_\mu(\mathbf{q}, \tau) j_\mu^\dagger(\mathbf{q}, 0) \rangle \\ &= \langle e^{iH\tau/\hbar} j_\mu^\dagger(\mathbf{q}, 0) e^{-iH\tau/\hbar} j_\mu^\dagger(\mathbf{q}, 0) \rangle \\ &= \sum_{a,b} \frac{e^{-\beta E_b}}{Z} \langle b | e^{iH\tau/\hbar} j_\mu(\mathbf{q}) | a \rangle \langle a | e^{-iH\tau/\hbar} j_\mu^\dagger(\mathbf{q}) | b \rangle \\ &= \sum_{a,b} \frac{e^{-\beta E_b}}{Z} |\langle a | j_\mu^\dagger(\mathbf{q}) | b \rangle|^2 e^{i\omega_{ab}\tau}. \end{aligned} \quad (2.113)$$

Finally, the Fourier transform of this expression is given by

$$K_\mu(\mathbf{q}, \omega) = \sum_{a,b} \frac{e^{-\beta E_b}}{Z} |\langle a | j_\mu^\dagger(\mathbf{q}) | b \rangle|^2 \delta(\omega - \omega_{ab}). \quad (2.114)$$

Note however that the imaginary part of the response function, calculated in equation (2.102), is given by

$$\Im \chi_\mu(\mathbf{q}, \omega) = L^2 \sum_{a,b} \frac{e^{-\beta E_b}}{Z} |\langle a | j_\mu^\dagger(\mathbf{q}) | b \rangle|^2 \frac{-\pi}{\hbar} [\delta(\omega - \omega_{ab}) - \delta(\omega + \omega_{ab})]. \quad (2.115)$$

We immediately see that correlation function is related to a response function in a simple manner:

$$\Im \chi_\mu(\mathbf{q}, \omega) = -\frac{\pi}{\hbar} L^2 [K_\mu(\mathbf{q}, \omega) - K_\mu(\mathbf{q}, -\omega)]. \quad (2.116)$$

By applying the detail balancing condition here, we can write

$$\Im \chi_\mu(\mathbf{q}, \omega) = -\frac{\pi}{\hbar} L^2 [1 - e^{-\beta \hbar \omega}] K_\mu(\mathbf{q}, \omega). \quad (2.117)$$

Finally we have

$$K_\mu(\mathbf{q}, \omega) = -\frac{\hbar}{\pi} \frac{1}{1 - e^{-\beta \hbar \omega}} \frac{1}{L^2} \Im \chi_\mu(\mathbf{q}, \omega), \quad (2.118)$$

or if we use the relation $\chi_\mu(\mathbf{q}, \omega) = -i\omega\sigma_\mu(\mathbf{q}, \omega)$ we can write this in a more convenient form as

$$K_\mu(\mathbf{q}, \omega) = \frac{1}{\pi} \frac{\hbar\omega}{1 - e^{-\beta\hbar\omega}} \frac{1}{L^2} \Re\sigma_\mu(\mathbf{q}, \omega). \quad (2.119)$$

This is in fact the well know fluctuation-dissipation theorem stating that the correlation function (K_μ) due to thermal fluctuations is directly related to the dissipation in the system ($\Re\sigma_\mu$ or $\Im\chi_\mu$). This result will be of use in the following section.

2.3 Radiative heat transfer

In this section we analyze the radiative heat transfer between two graphene sheets separated by a distance D and held at temperatures T_1 and T_2 (see figure 2.4). To calculate the heat transfer we shall start by looking into correlations between electric currents induced by the thermal fluctuations in the first graphene sheet. Following that we shall use Green function technique to find the electromagnetic fields in the second graphene sheet, induced by the fluctuating currents from the first sheet. Finally heat transfer can be found by calculating Ohmic losses, induced by this electromagnetic field, within the second graphene sheet.

In the last section we calculated current-current correlation function due to thermal fluctuations. Fluctuation-dissipation theorem (2.119) and equation (2.112) give the correlation function of the fluctuating currents in the first graphene sheet:

$$\langle j_{1\mu}(\mathbf{q}, \omega) j_{1\mu}^\dagger(\mathbf{q}, \omega') \rangle = \delta(\omega - \omega') \frac{1}{\pi} \frac{\hbar\omega}{1 - e^{-\beta_1\hbar\omega}} \frac{1}{L^2} \Re\sigma_{1\mu}(\mathbf{q}, \omega). \quad (2.120)$$

To find the electromagnetic fields induced by these fluctuating currents we can use classical electrodynamics so we shall start with classical quantities and return to the quantum values only later when necessary. Since the system is translational invariant we can focus on a single \mathbf{q}, ω -component and write the Fourier transform of the surface current density from the first graphene sheet as

$$\mathbf{j}_1(\mathbf{r}, t) = \int e^{-i\omega t} d\omega \sum_{\mathbf{q}} e^{i\mathbf{q}\cdot\mathbf{r}} \mathbf{j}_1(\mathbf{q}, \omega). \quad (2.121)$$

Further on, let us assume the most simple case where there is only vacuum in between and around graphene sheets. Then the electric field satisfies a simple wave equation

$$(\nabla^2 + \omega^2/c^2)\mathbf{E}(\mathbf{r}, z) = 0. \quad (2.122)$$

This equation has a plane wave solution $\mathbf{E}(\mathbf{r}, z) = \mathbf{E}(\mathbf{q}, \omega)e^{i\mathbf{q}\cdot\mathbf{r} + i\gamma z}$, where we took into consideration that the periodicity in the xy direction is determined by the wave vector \mathbf{q} . In other words we can write for the total wave vector: $\mathbf{w} = \mathbf{q} + \gamma\hat{\mathbf{z}}$, while the equation (2.122) requires: $w^2 = |\mathbf{w}|^2 = q^2 + \gamma^2 = \omega^2/c^2$ i.e. the z component of the wave vector \mathbf{w} is given by:

$$\gamma = \sqrt{\omega^2/c^2 - q^2}. \quad (2.123)$$

Further on, since there is no free charge around graphene sheets, the Gauss law states that $\nabla \cdot \mathbf{E}(\mathbf{r}, z) = 0$. This means that $\mathbf{E}(\mathbf{q}, \omega) \cdot \mathbf{w} = 0$ i.e. electric field is transversely polarized so it is convenient to introduce unit vectors $\hat{\mathbf{s}}$ and $\hat{\mathbf{p}}$ that are perpendicular to wave vector \mathbf{w} :

$$\hat{\mathbf{s}} = \hat{\mathbf{q}} \times \hat{\mathbf{z}}, \text{ and} \quad (2.124)$$

$$\hat{\mathbf{p}} = w^{-1}(-\gamma\hat{\mathbf{q}} + q\hat{\mathbf{z}}). \quad (2.125)$$

In this way $(\hat{\mathbf{s}}, \hat{\mathbf{w}}, \hat{\mathbf{p}})$ is a set of right-handed orthonormal triad (see figure 2.4) where

$$\hat{\mathbf{w}} = \frac{\mathbf{w}}{w} = w^{-1}(q\hat{\mathbf{q}} + \gamma\hat{\mathbf{z}}). \quad (2.126)$$

We also note that there is a simple connection with the longitudinal and transverse wave vectors introduced before in this chapter: $\mathbf{e}_{qL} = i\hat{\mathbf{q}}$, $\mathbf{e}_{qT} = -i\hat{\mathbf{s}}$.

To match the boundary conditions given by the surface current density $\mathbf{j}_1(\mathbf{q}, \omega)$ from the first graphene plane ($z = -D$) in the presence of the second graphene sheet ($z = 0$), we use the Green function technique from reference [60] which is particularly convenient for the layered structures like ours. In that manner one obtains different electric field component $\mathbf{E}(\mathbf{q}, \omega)$ depending whether we are located below the first graphene sheet ($z < -D$), in between the sheets ($-D < z < 0$), or above the second sheet ($z > 0$). Since we are interested in the field in the second sheet ($z = 0$), it is easiest to look into the expression for the field above the second graphene sheet ($z > 0$) where one

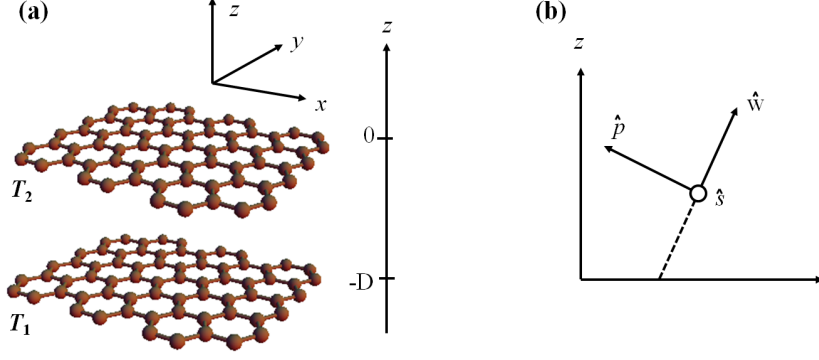


Figure 2.4: (a) Schematic diagram of the radiation transfer problem: a free standing sheet of graphene at temperature T_1 is radiating to another free standing graphene sheet at temperature T_2 and distance D away. (b) Polarization vectors defined in the text.

obtains

$$\mathbf{E}(\mathbf{q}, \omega) = -\frac{\omega}{2\epsilon_0 c^2 \gamma} (\hat{\mathbf{s}} T_{12}^s \hat{\mathbf{s}} + \hat{\mathbf{p}} T_{12}^p \hat{\mathbf{p}}) \cdot \mathbf{j}_1(\mathbf{q}, \omega). \quad (2.127)$$

Here we have explicitly separated s and p polarizations which have very different behavior, and T_{12} is a transmission coefficient for a system of two parallel graphene sheets given by [60]

$$T_{12} = \frac{t_1 t_2 e^{i\gamma D}}{1 - r_1 r_2 e^{2i\gamma D}}. \quad (2.128)$$

Note that the same expression is valid for s and p polarization, but reflection r and transmission t coefficients are different for different polarizations. It is a simple manner of elementary electrodynamics to demonstrate that these are

$$r^s = \frac{-\frac{\omega\sigma_T}{2\gamma\epsilon_0 c^2}}{1 + \frac{\omega\sigma_T}{2\gamma\epsilon_0 c^2}}, \quad (2.129)$$

$$t^s = \frac{1}{1 + \frac{\omega\sigma_T}{2\gamma\epsilon_0 c^2}}, \quad (2.130)$$

$$r^p = \frac{\frac{\gamma\sigma_L}{2\epsilon_0\omega}}{1 + \frac{\gamma\sigma_L}{2\epsilon_0\omega}}, \text{ and} \quad (2.131)$$

$$t^p = \frac{1}{1 + \frac{\gamma\sigma_L}{2\epsilon_0\omega}}. \quad (2.132)$$

Note also that transverse conductivity (σ_T) determines the s -polarization, and longitudinal conductivity (σ_L) determines the p -polarization. Finally the total electric field in the space above the second graphene sheet ($z > 0$) is given by

$$\mathbf{E}(\mathbf{r}, z, t) = \int e^{-i\omega t} d\omega \sum_{\mathbf{q}} e^{i\mathbf{q}\cdot\mathbf{r} + i\omega z} \mathbf{E}(\mathbf{q}, \omega). \quad (2.133)$$

So the field, precisely at the second sheet ($z = 0$) is

$$\mathbf{E}(\mathbf{r}, t) = \mathbf{E}(\mathbf{r}, z = 0^+, t) = \int e^{-i\omega t} d\omega \sum_{\mathbf{q}} e^{i\mathbf{q}\cdot\mathbf{r}} \mathbf{E}(\mathbf{q}, \omega). \quad (2.134)$$

At last, the heat transfer from the first graphene sheet to the second graphene sheet is simply given by Ohmic losses induced by this electric field. The power dissipated per unit area is given by [67]

$$\begin{aligned} H_{1 \rightarrow 2} &= \frac{1}{L^2} \frac{dE_{mech}}{dt} = \frac{1}{L^2} \int \mathbf{j}_2(\mathbf{r}, t) \cdot \mathbf{E}(\mathbf{r}, t) d\mathbf{r} \\ &= \int \int d\omega d\omega' e^{-i(\omega - \omega')t} \sum_{\mathbf{q}} \mathbf{j}_2(\mathbf{q}, \omega) \cdot \mathbf{E}^*(\mathbf{q}, \omega'). \end{aligned} \quad (2.135)$$

Let us now take into account that current densities $\mathbf{j}_{1,2}(\mathbf{q}, \omega)$ have only vector components along the graphene (xy) plane. Then due to equation (2.125) one has $\hat{\mathbf{p}} \cdot \mathbf{j}_1(\mathbf{q}, \omega) = -\frac{\gamma}{w} \hat{\mathbf{q}} \cdot \mathbf{j}_1(\mathbf{q}, \omega)$, and we can write equation (2.127) again as

$$\mathbf{E}(\mathbf{q}, \omega) = -\frac{\omega}{2\epsilon_0 c^2 \gamma} \left(\hat{\mathbf{s}} T_{12}^s \hat{\mathbf{s}} + \left(\frac{\gamma^2}{w^2} \hat{\mathbf{q}} - \frac{q\gamma}{w^2} \hat{\mathbf{z}} \right) T_{12}^p \hat{\mathbf{q}} \right) \cdot \mathbf{j}_1(\mathbf{q}, \omega). \quad (2.136)$$

Further on, the scalar product in the equation (2.135) can be written as $\mathbf{j}_2 \cdot \mathbf{E}^* = \mathbf{j}_2 \cdot \mathbf{E}_r^*$, where $\mathbf{E}_r = \mathbf{E} - (\mathbf{E} \cdot \hat{\mathbf{z}}) \hat{\mathbf{z}}$ is the projection of the electric field vector to the graphene (xy) plane. In that way we can write equation (2.136) as

$$\mathbf{E}_r(\mathbf{q}, \omega) = -\frac{\omega}{2\epsilon_0 c^2 \gamma} \left(\hat{\mathbf{s}} T_{12}^s \hat{\mathbf{s}} + \frac{\gamma^2}{w^2} \hat{\mathbf{q}} T_{12}^p \hat{\mathbf{q}} \right) \cdot \mathbf{j}_1(\mathbf{q}, \omega). \quad (2.137)$$

Let us note here again that $\hat{\mathbf{q}} = i\mathbf{e}_{qL}^*$ and $\hat{\mathbf{s}} = -i\mathbf{e}_{qT}^*$ while the longitudinal ($\mu = L$) and transverse ($\mu = T$) components of the current density are defined

as: $j_\mu(\mathbf{q}, \omega) = \mathbf{j}(\mathbf{q}, \omega) \cdot \mathbf{e}_{\mathbf{q}\mu}^*$. Then we can write equation (2.137) as

$$\mathbf{E}_r(\mathbf{q}, \omega) = -\frac{\omega}{2\epsilon_0 c^2 \gamma} \left(-\mathbf{e}_{\mathbf{q}T}^* T_{12}^s j_{1T}(\mathbf{q}, \omega) + -\frac{\gamma^2}{\omega^2} \mathbf{e}_{\mathbf{q}L}^* T_{12}^p j_{1L}(\mathbf{q}, \omega) \right). \quad (2.138)$$

Finally due to Ohm's law $j_{2\mu}(\mathbf{q}, \omega) = \sigma_{2\mu}(\mathbf{q}, \omega) E_{r,\mu}(\mathbf{q}, \omega)$ we have

$$\begin{aligned} \langle \mathbf{j}_2(\mathbf{q}, \omega) \cdot \mathbf{E}_r^*(\mathbf{q}, \omega') \rangle &= \frac{\omega^2}{4\epsilon_0^2 c^4 |\gamma|^2} \sigma_{2T}(\mathbf{q}, \omega) \langle j_{1T}(\mathbf{q}, \omega) j_{1T}(\mathbf{q}, \omega')^* \rangle |T_{12}^s|^2 \\ &\quad + \frac{|\gamma|^2}{4\epsilon_0^2 \omega^2} \sigma_{2L}(\mathbf{q}, \omega) \langle j_{1L}(\mathbf{q}, \omega) j_{1L}(\mathbf{q}, \omega')^* \rangle |T_{12}^p|^2. \end{aligned} \quad (2.139)$$

Here we have explicitly written the ensemble average which requires us to calculate precise quantum correlations of the current density operator. We have also used relation (2.112) which states that there is no correlation between different ω components due to translational invariance in the time domain. In fact the current-current correlation function (2.120) is given by

$$\langle j_{1\mu}(\mathbf{q}, \omega) j_{1\mu}^\dagger(\mathbf{q}, \omega') \rangle = \delta(\omega - \omega') \frac{1}{\pi} \frac{\hbar\omega}{1 - e^{-\beta_1 \hbar\omega}} \frac{1}{L^2} \Re \sigma_{1\mu}(\mathbf{q}, \omega). \quad (2.140)$$

Since the final result has to be a real quantity, we can simply look into real part of the expression (2.139)

$$\begin{aligned} \Re \langle \mathbf{j}_2(\mathbf{q}, \omega) \cdot \mathbf{E}_r^*(\mathbf{q}, \omega') \rangle &= \delta(\omega - \omega') \frac{1}{\pi} \frac{\hbar\omega}{1 - e^{-\beta_1 \hbar\omega}} \frac{1}{L^2} \times \\ &\quad \left(\frac{\omega^2}{4\epsilon_0^2 c^4 |\gamma|^2} \Re \sigma_{2T}(\mathbf{q}, \omega) \Re \sigma_{1T}(\mathbf{q}, \omega) |T_{12}^s|^2 + \right. \\ &\quad \left. + \frac{|\gamma|^2}{4\epsilon_0^2 \omega^2} \Re \sigma_{2L}(\mathbf{q}, \omega) \Re \sigma_{1L}(\mathbf{q}, \omega) |T_{12}^p|^2 \right). \end{aligned} \quad (2.141)$$

This can be written in a more transparent form by using reflection and transmission coefficients (2.129) - (2.132). However, since $\gamma = \sqrt{\omega^2/c^2 - q^2}$ we have to distinguish between the case of propagating waves in the far field ($\omega/c > q$) and evanescent waves in the near field ($\omega/c < q$). In the first case ($\omega/c > q$) one has

$$\frac{\omega}{2\epsilon_0 c^2 |\gamma|} \Re \sigma_T = \frac{1 - |r^s|^2 - |t^s|^2}{2|t^s|^2}, \text{ and} \quad (2.142)$$

$$\frac{|\gamma|}{2\epsilon_0 \omega} \Re \sigma_L = \frac{1 - |r^p|^2 - |t^p|^2}{2|t^p|^2}. \quad (2.143)$$

It is convenient here to define the following quantities

$$\begin{aligned} h_{ff}^s(\mathbf{q}, \omega) &\equiv \frac{\omega^2}{4\epsilon_0^2 c^4 |\gamma|^2} \Re\sigma_{1T}(\mathbf{q}, \omega) \Re\sigma_{2T}(\mathbf{q}, \omega) |T_{12}^s|^2 \\ &= \frac{(1 - |r_1^s|^2 - |t_1^s|^2)(1 - |r_2^s|^2 - |t_2^s|^2)}{4|1 - r_1^s r_2^s e^{2i\gamma D}|^2}, \text{ and} \end{aligned} \quad (2.144)$$

$$\begin{aligned} h_{ff}^p(\mathbf{q}, \omega) &\equiv \frac{|\gamma|^2}{4\epsilon_0^2 \omega^2} \Re\sigma_{1L}(\mathbf{q}, \omega) \Re\sigma_{2L}(\mathbf{q}, \omega) |T_{12}^p|^2 \\ &= \frac{(1 - |r_1^p|^2 - |t_1^p|^2)(1 - |r_2^p|^2 - |t_2^p|^2)}{4|1 - r_1^p r_2^p e^{2i\gamma D}|^2}, \end{aligned} \quad (2.145)$$

where we have used expression (2.128) for the transmission coefficient T_{12} . In the second case ($\omega/c < q$) one has

$$\frac{\omega}{2\epsilon_0 c^2 |\gamma|} \Re\sigma_T = \frac{\Im r^s}{|t^s|^2}, \quad (2.146)$$

$$\frac{|\gamma|}{2\epsilon_0 \omega} \Re\sigma_L = \frac{\Im r^p}{|t^p|^2}, \quad (2.147)$$

$$h_{nf}^s(\mathbf{q}, \omega) \equiv \frac{\omega^2}{4\epsilon_0^2 c^4 |\gamma|^2} \Re\sigma_{1T}(\mathbf{q}, \omega) \Re\sigma_{2T}(\mathbf{q}, \omega) |T_{12}^s|^2 = \frac{\Im r_1^s \Im r_2^s e^{-2|\gamma|D}}{|1 - r_1^s r_2^s e^{-2|\gamma|D}|^2}, \text{ and} \quad (2.148)$$

$$h_{nf}^p(\mathbf{q}, \omega) \equiv \frac{|\gamma|^2}{4\epsilon_0^2 \omega^2} \Re\sigma_{1L}(\mathbf{q}, \omega) \Re\sigma_{2L}(\mathbf{q}, \omega) |T_{12}^p|^2 = \frac{\Im r_1^p \Im r_2^p e^{-2|\gamma|D}}{|1 - r_1^p r_2^p e^{-2|\gamma|D}|^2}. \quad (2.149)$$

At last we obtain for the heat transfer (equation (2.135)) from the first graphene sheet to the second graphene sheet

$$H_{1 \rightarrow 2} = H_{1 \rightarrow 2, ff} + H_{1 \rightarrow 2, nf}, \quad (2.150)$$

where the far field ($\omega/c > q$) and near field ($\omega/c < q$) contributions are respectively given by

$$H_{1 \rightarrow 2, ff} = \frac{1}{\pi} \int d\omega \frac{\hbar\omega}{1 - e^{-\beta_1 \hbar\omega}} \frac{1}{L^2} \sum_{\mathbf{q}, \mu} h_{ff}^\mu(q, \omega), \text{ and} \quad (2.151)$$

$$H_{1 \rightarrow 2, nf} = \frac{1}{\pi} \int d\omega \frac{\hbar\omega}{1 - e^{-\beta_1 \hbar\omega}} \frac{1}{L^2} \sum_{\mathbf{q}, \mu} h_{nf}^\mu(q, \omega). \quad (2.152)$$

In the same manner one can calculate heat transfer from the second graphene sheet to the first graphene sheet $H_{2 \rightarrow 1}$, so the total heat transfer ($H = H_{1 \rightarrow 2} - H_{2 \rightarrow 1}$) between two graphene sheets can be written as

$$H = H_{ff} + H_{nf}, \quad (2.153)$$

$$H_{ff} = \frac{2}{\pi} \int_0^\infty d\omega [\Theta(\omega, T_1) - \Theta(\omega, T_2)] \frac{1}{(2\pi)^2} \int_0^{\omega/c} 2\pi q dq \sum_\mu h_{ff}^\mu(q, \omega), \quad (2.154)$$

$$H_{nf} = \frac{2}{\pi} \int_0^\infty d\omega [\Theta(\omega, T_2) - \Theta(\omega, T_1)] \frac{1}{(2\pi)^2} \int_{\omega/c}^\infty 2\pi q dq \sum_\mu h_{nf}^\mu(q, \omega). \quad (2.155)$$

Here we have introduced the Boltzman factor: $\Theta(\omega, T) = \hbar\omega/(e^{\beta\hbar\omega} - 1)$, which comes about since the zero point energy cancels when taking the difference between emission and absorption. We write here again functions h_{ff}^μ and h_{nf}^μ for the sake of clearance

$$h_{ff}^\mu(\mathbf{q}, \omega) \equiv \frac{(1 - |r_1^\mu|^2 - |t_1^\mu|^2)(1 - |r_2^\mu|^2 - |t_2^\mu|^2)}{4|1 - r_1^\mu r_2^\mu e^{2i\gamma D}|^2}, \quad (2.156)$$

$$h_{nf}^\mu(\mathbf{q}, \omega) \equiv \frac{\Im r_1^\mu \Im r_2^\mu e^{-2|\gamma|D}}{|1 - r_1^\mu r_2^\mu e^{-2|\gamma|D}|^2}. \quad (2.157)$$

Note that for the case of black body which has perfect absorption $1 = |a|^2 = 1 - |r|^2 - |t|^2$, i.e. zero reflection or transmission ($r = t = 0$), equation (2.154) simply gives the Stefan-Boltzman law:

$$H_{ff} = \frac{\pi^2 k^4}{60c^2 \hbar^3} (T_1^4 - T_2^4) \quad (2.158)$$

To summarize, in this section we have calculated the total heat transfer, that is, the transfer of heat energy per unit time per unit area between two graphene sheets at different temperatures. Total heat transfer $H = H_{ff} + H_{nf}$ has a contribution from the propagating waves in the far field (H_{ff}) and evanescent waves in the near field (H_{nf}), given by equations (2.154) and (2.155), respectively.

Chapter 3

Plasmonics in graphene

In this chapter we investigate plasmons in doped graphene and demonstrate that they simultaneously enable low-losses and significant wave localization for frequencies of the light smaller than the optical phonon frequency $\hbar\omega_{Oph} \approx 0.2$ eV. Interband losses via emission of electron-hole pairs (1st order process) can be blocked by sufficiently increasing the doping level, which pushes the interband threshold frequency ω_{inter} toward higher values (already experimentally achieved doping levels can push it even up to near infrared frequencies). The plasmon decay channel via emission of an optical phonon together with an electron-hole pair (2nd order process) is inactive for $\omega < \omega_{Oph}$ (due to energy conservation), however, for frequencies larger than ω_{Oph} this decay channel is non-negligible. This is particularly important for large enough doping values when the interband threshold ω_{inter} is above ω_{Oph} : in the interval $\omega_{Oph} < \omega < \omega_{inter}$ the 1st order process is suppressed, but the phonon decay channel is open. In this chapter, the calculation of losses is performed within the framework of a random-phase approximation (RPA) and number conserving relaxation-time approximation [34]; the measured DC relaxation-time from Ref. [5] serves as an input parameter characterizing collisions with impurities, whereas the optical phonon relaxation times are estimated from the influence of the electron-phonon coupling [35] on the optical conductivity [36].

In Sec. 3.1, we provide a brief review of conventional surface plasmons and their relevance for nanophotonics. In Sec. 3.2 we discuss the trade off between plasmon losses and wave localization in doped graphene, as well as the optical properties of these plasmons. We conclude and provide an outlook in Sec. 3.3.

3.1 Surface plasmons

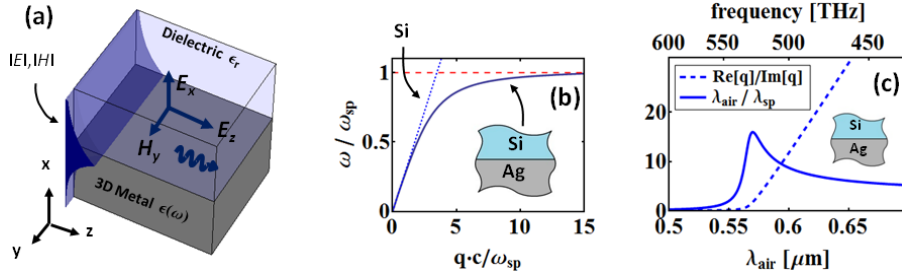


Figure 3.1: (a) Schematic description of a surface plasmon (SP) on metal-dielectric interface. (b) SP dispersion curve (solid blue line) for Ag-Si interfaces; dotted blue is the light line in Si; dashed red line denotes the SP resonance. (c) Wave localization and propagation length for SPs at Ag-Si interface (experimental Ag losses are taken into account).

Surface plasmons (SPs) are electromagnetic (EM) waves that propagate along the boundary surface of a metal and a dielectric [see Fig. 3.1(a)]; these are transverse magnetic (TM) modes accompanied by collective oscillations of surface charges, which decay exponentially in the transverse directions (see, e.g., Refs. [12, 13] and Refs. therein). Their dispersion curve is given by:

$$q_{sp} = \frac{\omega}{c} \sqrt{\frac{\epsilon_r \epsilon(\omega)}{\epsilon_r + \epsilon(\omega)}} \quad (3.1)$$

[see Fig. 3.1(b)]; note that close to the SP resonance ($\omega = \omega_{SP}$), the SP wave vector [solid blue line in Fig. 3.1(b)] is much larger than the wave vector of the same frequency excitation in the bulk dielectric [dotted blue line in Fig. 3.1(b)]. As a result, a localized SP wave packet can be much smaller than a same frequency wave packet in a dielectric. Moreover, this shrinkage is accompanied by a large transverse localization of the plasmonic modes. These features are considered very promising for enabling nano-photonics [12, 13, 14, 15], as well as high field localization and enhancement. A necessary condition for the existence of SPs is $\epsilon(\omega) < -\epsilon_r$ (i.e., $\epsilon(\omega)$ is negative), which is why metals are usually used. However, SPs in metals are known to have small propagation lengths, which are conveniently quantified (in terms of the SP wavelength) with the ratio $\Re q_{sp} / \Im q_{sp}$; this quantity is a measure of how many SP wavelengths can an SP propagate before it loses most of its energy. The

wave localization (or wave "shrinkage") is quantified as $\lambda_{air}/\lambda_{sp}$, where $\lambda_{air} = 2\pi c/\omega$ (the wavelength in air). These quantities are plotted in Fig. 3.1(c) for the case of Ag-Si interface, by using experimental data (see [14] and references therein) to model silver (metal with the lowest losses for the frequencies of interest). Near the SP resonance, wave localization reaches its peak; however, losses are very high there resulting in a small propagation length $l \approx 0.1\lambda_{sp} \approx 5\text{nm}$. At higher wavelengths one can achieve low losses but at the expense of poor wave localization.

3.2 Plasmons and their losses in doped graphene

Graphene behaves as an essentially 2D electronic system. In the absence of doping, conduction and valence bands meet at a point (called Dirac point) which is also the position of the Fermi energy. The band structure, calculated in the tight binding approximation is shown in Fig. 2(b); for low energies the dispersion around the Dirac point can be expressed as $E_{n,\mathbf{k}} = nv_F\hbar|\mathbf{k}|$, where the Fermi velocity is $v_F = 10^6\text{m/s}$, $n = 1$ for conduction, and $n = -1$ for the valence band. Recent experiments [37] have shown that this linear dispersion relation is still valid even up to the energies (frequencies) of visible light, which includes the regime we are interested in.

Here we consider TM modes in geometry depicted in figure 3.2 (a), where graphene is surrounded with dielectrics of constants ϵ_{r1} and ϵ_{r2} . Throughout the paper, for definiteness we use $\epsilon_{r1} = 4$ corresponding to SiO_2 substrate, and $\epsilon_{r2} = 1$ for air on top of graphene, which corresponds to a typical experimental setup. TM modes are found by assuming that the electric field has the form

$$\begin{aligned} E_z &= Ae^{iqz-Q_1x}, E_y = 0, E_x = Be^{iqz-Q_1x}, \text{ for } x > 0, \\ E_z &= Ce^{iqz+Q_2x}, E_y = 0, E_x = De^{iqz+Q_2x}, \text{ for } x < 0. \end{aligned} \quad (3.2)$$

After inserting this ansatz into Maxwells equations and matching the boundary conditions [which include the conductance of the 2D graphene layer, $\sigma(\omega, q)$], we obtain the dispersion relation for TM modes:

$$\frac{\epsilon_{r1}}{\sqrt{q^2 - \frac{\epsilon_{r1}\omega^2}{c^2}}} + \frac{\epsilon_{r2}}{\sqrt{q^2 - \frac{\epsilon_{r2}\omega^2}{c^2}}} = -\frac{\sigma(\omega, q)i}{\omega\epsilon_0} \quad (3.3)$$

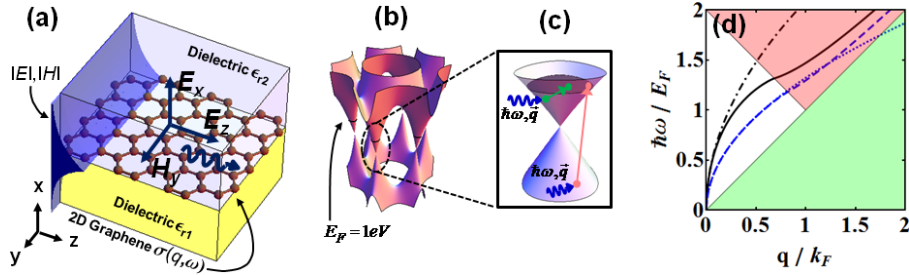


Figure 3.2: (a) Schematic of the graphene system and TM plasmon modes. Note that the profile of the fields looks the same as the fields of an SP [Fig. 3.1(a)]. (b) Electronic band structure of graphene; to indicate the vertical scale we show the Fermi energy level for the case $E_F = 1 \text{ eV}$. (c) Sketch of the intraband (green arrows) and interband (red arrows) single particle excitations that can lead to large losses; these losses can be avoided by implementing a sufficiently high doping. (d) Plasmon RPA and semiclassical dispersion curves. Black solid (RPA) and black dot-dashed (semiclassical) lines correspond to $\epsilon_{r1} = \epsilon_{r2} = 1$; Blue dashed (RPA) and blue dotted (semiclassical) lines correspond to $\epsilon_{r1} = 4$ and $\epsilon_{r2} = 1$. The green (lower) and rose (upper) shaded areas represent regimes of intraband and interband excitations, respectively.

By explicitly writing the dependence of the conductivity on the wave vector q we allow for the possibility of nonlocal effects, where the mean free path of electrons can be smaller than q^{-1} [38]. Throughout this work we consider the nonretarded regime ($q \gg \omega/c$), so equation (3.3) simplifies to

$$q \approx Q_1 \approx Q_2 \approx \epsilon_0 \frac{\epsilon_{r1} + \epsilon_{r2}}{2} \frac{2i\omega}{\sigma(\omega, q)}. \quad (3.4)$$

Note that a small wavelength (large q) leads to a high transversal localization of the modes, which are also accompanied by a collective surface charge oscillation, similar to SPs in metals; however, it should be understood that, in contrast to SPs, here we deal with 2D collective excitations, i.e. plasmons. We note that even though field profiles of plasmons in graphene and SPs in metals look the same, these two systems are qualitatively different since electrons in graphene are essentially frozen in the transverse dimension [39]. This fact and the differences in electronic dispersions (linear Dirac cones vs. usual parabolic) lead to qualitatively different dispersions of TM modes in these two systems [see Fig. 3.1(b) and Fig. 3.2(d)]. To find dispersion of plasmons in graphene we need the conductivity of graphene $\sigma(\omega, q)$, which we now proceed to ana-

lyze by employing the semiclassical model [38] (in subsection 3.2.1), RPA and number conserving relaxation-time approximation [34] (in subsection 3.2.2), and by estimating the relaxation-time due to the influence of electron-phonon coupling [35] on the optical conductivity [36] (in subsection 3.2.3).

3.2.1 Semiclassical model

For the sake of the clarity of the presentation, we first note that by employing a simple semi-classical model for the conductivity (see Ref. [38]), one obtains a Drude-like expression:

$$\sigma(\omega) = \frac{e^2 E_F}{\pi \hbar^2} \frac{i}{\omega + i\tau^{-1}} \quad (3.5)$$

(the semiclassical conductivity does not depend on q). Here τ denotes the relaxation-time (RT), which in a phenomenological way takes into account losses due to electron-impurity, electron-defect, and electron-phonon scattering. Equation (3.5) is obtained by assuming zero temperature $T \approx 0$, which is a good approximation for highly doped graphene considered here, since $E_F \gg k_B T$. From Eqs. (3.4) and (3.5) it is straightforward to obtain plasmon dispersion relation:

$$q(\omega) = \frac{\pi \hbar^2 \epsilon_0 (\epsilon_{r1} + \epsilon_{r2})}{e^2 E_F} \left(1 + \frac{i}{\tau \omega}\right) \omega^2, \quad (3.6)$$

as well as losses,

$$\frac{\Re q}{\Im q} = \omega \tau = \frac{2\pi c \tau}{\lambda_{air}}. \quad (3.7)$$

In order to quantify losses one should estimate the relaxation time τ . If the frequency ω is below the interband threshold frequency ω_{inter} , and if $\omega < \omega_{Oph}$, then both interband damping and plasmon decay via excitation of optical phonons together with an electron-hole pair are inactive. In this case, the relaxation time can be estimated from DC measurements [5], i.e., it can be identified with DC relaxation time which arises mainly from impurities (see Refs. [5]). It is reasonable to expect that impurity related relaxation time will not display large frequency dependence. In order to gain insight into the losses by using this line of reasoning let us assume that the doping level is given by $E_F = 0.64$ eV (corresponding to electron concentration of $n = 3 \times 10^{13}$ cm⁻²);

the relaxation time corresponds to DC mobility $\mu = 10000 \text{ cm}^2/\text{Vs}$ measured in Ref. [5]: $\tau_{DC} = \mu \hbar \sqrt{n\pi} / ev_F = 6.4 \times 10^{-13} \text{ s}$. As an example, for the frequency $\hbar\omega = 0.155 \text{ eV}$ ($\lambda_{air} = 8 \mu\text{m}$), the semiclassical model yields $\Re q / \Im q \approx 151$ for losses and $\lambda_{air} / \lambda_p \approx 42$ for wave localization. Note that both of these numbers are quite favorable compared to conventional SPs [e.g., see Fig. 3.1(c)]. It will be shown in the sequel that for the doping value $E_F = 0.64 \text{ eV}$ this frequency is below the interband loss threshold, and it is evidently also smaller than the optical phonon loss threshold $\hbar\omega_{Oph} \approx 0.2 \text{ eV}$, so both of these loss mechanisms can indeed be neglected.

3.2.2 RPA and relaxation-time approximation

In order to take the interband losses into account, we use the self-consistent linear response theory, also known as the random-phase approximation (RPA) [38], together with the relaxation-time (finite τ) approximation introduced by Mermin [34]. Both of these approaches, that is, the collisionless RPA ($\tau \rightarrow \infty$) [40, 41], and the RPA-RT approximation (finite τ) [46], have been applied to study graphene. In the $\tau \rightarrow \infty$ case, the RPA 2D polarizability of graphene is given by [41]:

$$\bar{\chi}(q, \omega) = \frac{e^2}{q^2} \Pi(q, \omega), \quad (3.8)$$

where

$$\begin{aligned} \Pi(q, \omega) = \frac{4}{\Omega} \sum_{\mathbf{k}, n_1, n_2} \frac{f(E_{n_2, \mathbf{k}+\mathbf{q}}) - f(E_{n_1, \mathbf{k}})}{\hbar\omega + E_{n_1, \mathbf{k}} - E_{n_2, \mathbf{k}+\mathbf{q}} + i\eta} \\ \times |\langle n_1, \mathbf{k} | e^{-i\mathbf{q}\cdot\mathbf{r}} | n_2, \mathbf{k} + \mathbf{q} \rangle|^2. \end{aligned} \quad (3.9)$$

Here $f(E) = (e^{(E-E_F)/k_B T} + 1)^{-1}$ is the Fermi distribution function, E_F is the Fermi energy and factor 4 stands for 2 spin and 2 valley degeneracies. Note that polarizability $\bar{\chi}(q, \omega)$ is simply related to the density-density response function $\chi(q, \omega)$, introduced in chapter 2, since $\Pi(q, \omega) = -\chi(q, \omega)$.

Now, in Eq. (3.8) ω is given an infinitesimally small imaginary part which leads to the famous Landau damping; that is, plasmons can decay by exciting an electron-hole pair (interband and intraband scattering) as illustrated in Fig. 3.2(c). The effects of other types of scattering (impurities, phonons) can be accounted for by using the relaxation-time τ as a parameter within the

RPA-RT approach [34], which takes into account conservation of local electron number. Within this approximation the 2D polarizability is

$$\bar{\chi}_\tau(q, \omega) = \frac{(1 + i/\omega\tau)\bar{\chi}(q, \omega + i/\tau)}{1 + (i/\omega\tau)\bar{\chi}(q, \omega + i/\tau)/\bar{\chi}(q, 0)}. \quad (3.10)$$

The 2D dielectric function and conductivity are respectively given by (see [42]): and

$$\sigma_{RPA}(q, \omega) = -i\omega\bar{\chi}_\tau(q, \omega). \quad (3.11)$$

We note here that throughout the text only π -bands are taken into consideration; it is known that in graphite, higher σ -bands give rise to a small background dielectric constant [43] at low energies, which is straightforward to implement in the formalism. Using Eqs. (3.4) and (3.11) we obtain that the properties of plasmons (i.e., dispersion, wave localization and losses) can be calculated by solving

$$\epsilon_{RPA}(q, \omega) = 0, \quad (3.12)$$

with complex wave vector $q = q_1 + iq_2$. The calculation is simplified by linearizing Eq. (3.12) in terms of small q_2/q_1 , to obtain,

$$\frac{\epsilon_{r1} + \epsilon_{r2}}{2} + \frac{e^2}{2\epsilon_0 q_1} \Re[\Pi(q_1, \omega)] = 0, \quad (3.13)$$

for the plasmon dispersion, and

$$q_2 = \frac{\Im[\Pi(q_1, \omega)] + \frac{1}{\tau} \frac{\partial}{\partial \omega} \Re[\Pi(q_1, \omega)] + \frac{1}{\omega\tau} \Re[\Pi(q_1, \omega)(1 - \Pi(q_1, \omega))/\Pi(q_1, 0)]}{\frac{1}{q_1} \Re[\Pi(q_1, \omega)] - \frac{\partial}{\partial q_1} \Re[\Pi(q_1, \omega)]} \quad (3.14)$$

yielding losses. Note that in the lowest order the dispersion relation (and consequently λ_{air}/λ_p and the group velocity v_g) does not depend on τ . This linearization is valid when $q_2 \ll q_1$; as the plasmon losses increase, e.g., after entering the interband regime [the rose area in Fig. 3.2(d)], results from Eqs. (3.13) and (3.14) should be regarded as only qualitative. The characteristic shape of the plasmon dispersion is shown in Fig. 3.2(d). Note that the semi-classical model and the RPA model agree well if the system is sufficiently below the interband threshold [for small q , $\omega(q) \sim \sqrt{q}$ as in Eq. (3.6)]. By comparing Figs. 3.2(d) and 3.1(b) we see that the dispersion for SPs on silver-dielectric surface qualitatively differs from the plasmon dispersion in graphene

[39]. While SPs' dispersion relation approaches an asymptote ($\omega \rightarrow \omega_{SP}$) for large q values [Eq. (3.1)], graphene plasmon relation gives $\omega(q)$ which continuously increases [Fig. 3.2(d)].

Theoretically predicted plasmon losses $\Re q/\Im q$ and wave localization λ_{air}/λ_p are illustrated in Fig. 3.3 for doping level $E_F = 0.135$ eV and relaxation time $\tau = 1.35 \times 10^{-13}$ s. We observe that for this particular doping level, for wavelengths smaller than $\lambda_{inter} \approx 7.7 \mu\text{m}$, the system is in the regime of high interband losses (rose shaded region). Below the interband threshold, both losses and wave localization obtained by employing RPA-RT approach are quite well described by the previously obtained semiclassical formulae. Since the frequencies below the interband threshold are (for the assumed doping level) also below the optical phonon frequency, the relaxation time can be estimated from DC measurements.

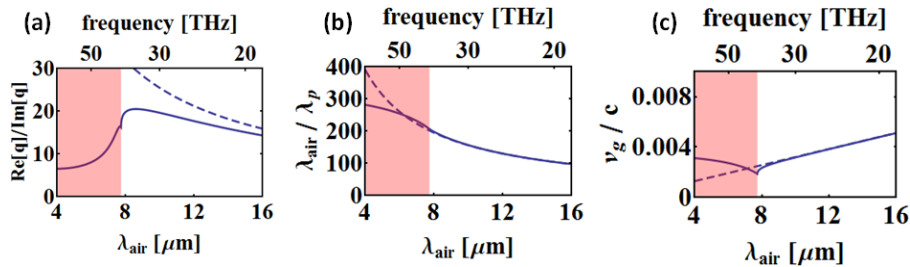


Figure 3.3: Properties of plasmons in doped graphene. Solid-lines are obtained with the number-conserving RPA calculation, and the dashed lines with the semiclassical approach. Losses (a), field localization (wave "shrinkage") (b), and group velocity (c) for doping $E_F = 0.135$ eV, and relaxation time $\tau = 1.35 \times 10^{-13}$ s, which corresponds to the mobility of $10000 \text{ cm}^2/\text{Vs}$. The upper scale in all figures is frequency $\nu = \omega/2\pi$, whereas the rose shaded areas denote the region of high interband losses.

At this point we also note that in all our calculations we have neglected the finite temperature effects, i.e., $T \approx 0$. To justify this, we note that for doping values utilized in this paper the Fermi energies are $0.135 \text{ eV} \approx 5.2k_B T_r$ ($n = 1.35 \times 10^{12} \text{ cm}^{-2}$) and $0.64 \text{ eV} \approx 25k_B T_r$ ($n = 3 \times 10^{13} \text{ cm}^{-2}$) for room temperature $T_r = 300$ K. The effect of finite temperature is to slightly smear the sharpness of the interband threshold, but only in the vicinity ($\sim k_B T_r$) of the threshold.

By increasing the doping, E_F increases, and the region of interband plasmonic losses moves towards higher frequencies (smaller wavelengths). How-

ever, by increasing the doping, the interband threshold frequency will eventually become larger than graphene's optical phonon frequency ω_{Oph} : there will exist an interval of frequencies, $\omega_{Oph} < \omega < \omega_{inter}$, where it is kinematically possible for the photon of frequency ω to excite an electron-hole pair together with emission of an optical phonon. This second order process can reduce the relaxation time estimated from DC measurements and should be taken into account, as we show in the following subsection.

3.2.3 Losses due to optical phonons

In what follows, we estimate and discuss the relaxation time due to the electron-phonon coupling. This can be done by using the Kubo formula which has been utilized in Ref. [36] to calculate the real part of the optical conductivity, $\Re\sigma(\omega, q = 0)$. The calculation of conductivity $\Re\sigma(\omega, 0)$ involves the electron self-energy $\Sigma(E)$, whose imaginary part expresses the width of a state with energy E , whereas the real part corresponds to the energy shift. Let us assume that the electron self-energy stems from the electron-phonon coupling and impurities,

$$\Sigma(E) = \Sigma_{e-ph}(E) + \Sigma_{imp}(E). \quad (3.15)$$

For Σ_{e-ph} we utilize a simple yet fairly accurate model derived in Ref. [35]: If $|E - E_F| > \hbar\omega_{Oph}$, then

$$\Im\Sigma_{e-ph}(E) = \gamma|E - \text{sgn}(E - E_F)\hbar\omega_{Oph}|, \quad (3.16)$$

while elsewhere $\Im\Sigma_{e-ph}(E) = 0$; the dimensionless constant $\gamma = 18.3 \times 10^{-3}$ [35] is proportional to the square of the electron-phonon matrix element [35], i.e., the electron-phonon coupling coefficient. In order to mimic impurities, we will assume that $\Im\Sigma_{imp}(E)$ is a constant (whose value can be estimated from DC measurements). The real parts of the self-energies are calculated by employing the Kramers-Krönig relations. In all our calculations the cut-off energy is taken to be 8.4 eV, which corresponds to the cut-off wavevector $k_c = \pi/a$, where $a = 2.46 \text{ \AA}$. By employing these self-energies we calculate the conductivity $\Re\sigma(\omega, q = 0)$, from which we estimate the relaxation time by

using Eq. (3.5), i.e.,

$$\tau(\omega) \approx \frac{e^2 E_F}{\pi \hbar^2 \omega^2} \frac{1}{\Re \sigma(\omega, 0)} \quad (3.17)$$

for the region below the interband threshold; in deriving (3.17) we have assumed $\tau\omega \gg 1$.

Figure 3.4 plots the real part of the conductivity and the relaxation time for two values of doping: $E_F = 0.135$ eV ($n = 1.35 \times 10^{12}$ cm $^{-2}$, solid line) and $E_F = 0.64$ eV ($n = 3 \times 10^{13}$ cm $^{-2}$, dashed line). In order to isolate the influence of the electron-phonon coupling on the conductivity and plasmon losses, the contribution from impurities is assumed to be very small: $\Im \Sigma_{imp}(E) = 10^{-6}$ eV. The real part of the conductivity has a universal value $\sigma_0 = \pi e^2/2h$ above the interband threshold value $\hbar\omega = 2E_F$ (for $q = 0$), e.g., see [37, 44]. We clearly see that the relaxation time is not affected by the electron-phonon coupling for frequencies below ω_{Oph} , that is, we conclude that scattering from impurities and defects is a dominant decay mechanism for $\omega < \omega_{Oph}$ (assuming we operate below the interband threshold). However, for $\omega > \omega_{Oph}$, the relaxation times in Fig. 3.4 are on the order of $10^{-14} - 10^{-13}$ s, indicating that optical phonons are an important decay mechanism.

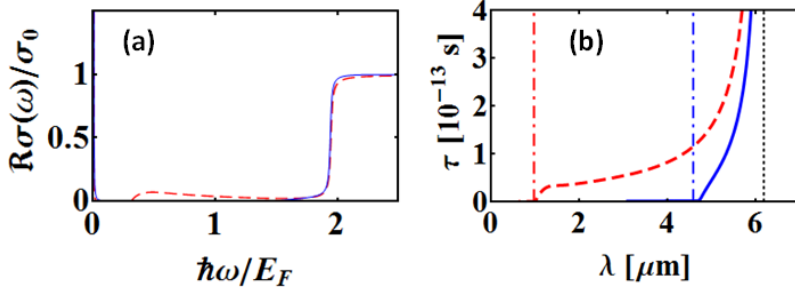


Figure 3.4: (a) The real part of the conductivity in units of $\sigma_0 = \pi e^2/2h$ in dependence of frequency $\hbar\omega/E_F$, and (b) the corresponding relaxation time as a function of wavelength. The contribution to $\Re \sigma(\omega)$ from impurities is chosen to be negligible. The displayed graphs correspond to two different values of doping which yield $E_F = 0.135$ eV (solid blue line), and $E_F = 0.640$ eV (dashed red line). The position of the optical phonon frequency $\hbar\omega_{Oph} \approx 0.2$ eV is depicted by the dotted vertical line in (b); dot-dashed lines depict the values of wavelengths corresponding to $2E_F$, that is, the interband threshold value (for $q = 0$) for the two doping concentrations.

It should be emphasized that the exact calculated values should be taken with some reservation for the following reason: strictly speaking, one should

calculate the relaxation times $\tau(\omega, q)$ along the plasmon dispersion curve given by Eq. (3.13); namely the matrix elements which enter the calculation depend on q , whereas the phase space available for the excitations also differ for $q = 0$ and $q > 0$. Moreover, the exact value of the matrix element for electron phonon coupling is still a matter of debate in the community. Therefore, the actual values for plasmon losses could be somewhat different for $\omega > \omega_{Oph}$. Nevertheless, fairly small values of relaxation times presented in Fig. 3.4 for $\omega > \omega_{Oph}$ indicate that emission of an optical phonon together with an electron-hole pair is an important decay mechanism in this regime. Precise calculations for $q > 0$ and $\omega > \omega_{Oph}$ are a topic for a future paper.

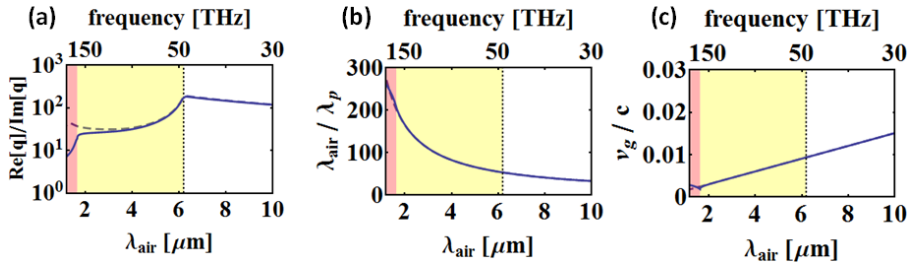


Figure 3.5: Properties of plasmons in doped graphene. Solid-lines are obtained with the number-conserving RPA calculation, and the dashed lines with the semiclassical approach. Losses (a), field localization (wave "shrinkage") (b), and group velocity (c) for doping $E_F = 0.64$ eV; losses are calculated by using the relaxation time $\tau^{-1} = \tau_{DC}^{-1} + \tau_{e-ph}^{-1}$, where $\tau_{DC} = 6.4 \times 10^{-13}$ s, and τ_{e-ph} is the relaxation time from the electron-phonon coupling for the given parameters. In the white regions (right regions in all panels), losses are determined by τ_{DC} . In the yellow shaded regions (central regions in all panels), losses are determined by the optical phonon emission, i.e., τ_{e-ph} . The rose shaded areas (left region in all panels) denote the region of high interband losses. Dotted vertical lines correspond to the optical phonon frequency $\omega_{Oph} \approx 0.2$ eV. The upper scale in all figures is frequency $\nu = \omega/2\pi$. See text for details.

Plasmonic losses and wave localization calculated from the RPA-RT approximation are illustrated in Fig. 3.5 for doping level $E_F = 0.64$ eV and the relaxation time τ given by $\tau^{-1} = \tau_{DC}^{-1} + \tau_{e-ph}^{-1}$, where $\tau_{DC} = 6.4 \times 10^{-13}$ s (mobility $10000 \text{ cm}^2/\text{Vs}$), whereas τ_{e-ph} is frequency dependent and corresponds to electron-phonon coupling assuming very clean samples [see dashed line in Fig. 3.4(b)]. Interband losses [left (rose shaded) regions in all panels] are active for wavelengths smaller than $\lambda_{inter} \approx 1.7 \mu\text{m}$. In the frequency in-

terval $\omega_{inter} > \omega > \omega_{Oph}$ [central (yellow shaded) regions in all panels], the decay mechanism via electron phonon coupling determines the loss rate, i.e., $\tau \approx \tau_{e-ph}$. For $\omega < \omega_{Oph}$ [right (white) regions in all panels], the DC relaxation time τ_{DC} can be used to estimate plasmon losses.

It should be noted that the mobility of $10000 \text{ cm}^2/\text{Vs}$ could be improved, likely even up to mobility $100000 \text{ cm}^2/\text{Vs}$ [47], thereby further improving plasmon propagation lengths for frequencies below the optical phonon frequency. However, for these larger mobilities the calculation of losses should also include in more details the frequency dependent contribution to the relaxation time from acoustic phonons (this decay channel is open at all frequencies); such a calculation would not affect losses for $\omega > \omega_{Oph}$ where optical phonons are dominant.

3.3 Conclusion and Outlook

In conclusion, we have used RPA and number-conserving relaxation-time approximation with experimentally available input parameters, and theoretical estimates for the relaxation-time utilizing electron-phonon coupling, to study plasmons and their losses in doped graphene. We have shown that for sufficiently large doping values high wave localization and low losses are simultaneously possible for frequencies below that of the optical phonon branch $\omega < \omega_{Oph}$ (i.e., $E_{plasmon} < 0.2 \text{ eV}$). For sufficiently large doping values, there is an interval of frequencies above ω_{Oph} and below interband threshold, where an important decay mechanism for plasmons is excitation of an electron-hole pair together with an optical phonon (for $\omega < \omega_{Oph}$ this decay channel is inactive); the relaxation times for this channel were estimated and discussed. We point out that further more precise calculations of plasmon relaxation times should include coupling to the substrate (e.g., coupling to surface-plasmon polaritons of the substrate), a more precise shape of the phonon dispersion curves, and dependence of the relaxation time via electron-phonon coupling on $q > 0$ (see subsection 3.2.3).

The main results, shown in Figures 3.3 and 3.5 point out some intriguing opportunities offered by plasmons in graphene for the field of nano-photonics and metamaterials in infrared (i.e. for $\omega < \omega_{Oph}$). For example, we can see in

those figures that high field localization and enhancement $\lambda_{air}/\lambda_p \sim 200$ [see Figure 3.3(b)] are possible (resulting in $\lambda_p < 50$ nm), while plasmons of this kind could have propagation loss-lengths as long as $\sim 10\lambda_p$ [see Fig. 3.5(a)]; these values (albeit at different frequencies) are substantially more favorable than the corresponding values for conventional SPs, for example, for SPs at the Ag/Si interface $\lambda_{air}/\lambda_p \sim 20$, whereas propagation lengths are only $\sim 0.1\lambda_{sp}$ [see Fig. 3.1(c)]. Another interesting feature of plasmons in graphene is that, similar to usual SP-systems [15], wave localization is followed by a group velocity decrease; the group velocities can be of the order $v_g = 10^{-3} - 10^{-2}c$, and the group velocity can be low over a wide frequency range, as depicted in Figs. 3.3(c) and 3.5(c). This is of interest for possible implementation of novel nonlinear optical devices in graphene, since it is known that small group velocities can lead to savings in both the device length and the operational power [45]; the latter would also be reduced because of the large transversal field localization of the plasmon modes.

Chapter 4

Transverse-electric plasmons

In Chapter 3 we were studying longitudinal charge density oscillations i.e. longitudinal plasmons or TM modes. However, due to unusual electron dispersion, graphene can also support transverse plasmons or TE modes [48]. These excitations are possible only if the imaginary part of the conductivity of a thin sheet of material is negative [48]. On the other hand, such a conductivity requires some complexity of the band structure of the material involved. For example, TE plasmons cannot occur if the 2D material possesses a single parabolic electron band. From this perspective, bilayer graphene, with its rich band structure and optical conductivity (e.g., see [49] and references therein), seems as a promising material for exploring the possibility of existence of TE plasmons. Here we predict the existence of TE plasmons in bilayer graphene. We find that their plasmonic properties are much more pronounced in bilayer than in monolayer graphene, in a sense that the wavelength of TE plasmons in bilayer can be smaller than in monolayer graphene at the same frequency.

Throughout this work we consider bilayer graphene as an infinitely thin sheet of material with conductivity $\sigma(\mathbf{q}, \omega)$. We assume that air with $\epsilon_r = 1$ is above and below bilayer graphene. Given the conductivity, by employing classical electrodynamics, one finds that self-sustained oscillations of the charge occur when (see [48] and references therein)

$$1 + \frac{i\sigma(\mathbf{q}, \omega)\sqrt{q^2 - \omega^2/c^2}}{2\epsilon_0\omega} = 0 \quad (4.1)$$

for TM modes, and

$$1 - \frac{\mu_0 \omega i \sigma(\mathbf{q}, \omega)}{2\sqrt{q^2 - \omega^2/c^2}} = 0 \quad (4.2)$$

for TE modes. The TM plasmons can considerably depart from the light line, that is, their wavelength can be considerably smaller than that of light at the same frequency. For this reason, when calculating TM plasmons it is desirable to know the conductivity as a function of both frequency ω and wavevector \mathbf{q} . However, it turns out that the TE plasmons (both in monolayer [48] and bilayer graphene, as will be shown below) are quite close to the light line $q = \omega/c$, and therefore it is a good approximation to use $\sigma(\omega) = \sigma(\mathbf{q} = 0, \omega)$. Moreover, these plasmons are expected to show strong polariton character, i.e., creation of hybrid plasmon-photon excitations. At this point it is worthy to note that if the relative permittivity of dielectrics above and below graphene are sufficiently different, so that light lines differ substantially, then TE plasmon will not exist (perhaps they could exist as leaky modes).

4.1 Optical conductivity of bilayer graphene

The conductivity $\sigma(\omega) = \Re\sigma(\omega) + i\Im\sigma(\omega)$ is complex, and plasmon dispersion is characterized by the imaginary part $\Im\sigma(\omega)$, whereas $\Re\sigma(\omega)$ determines plasmon losses, or more generally absorption of the sheet. From Eq. (4.2) it follows that the TE plasmons exist only if $\Im\sigma(\omega) < 0$ [48].

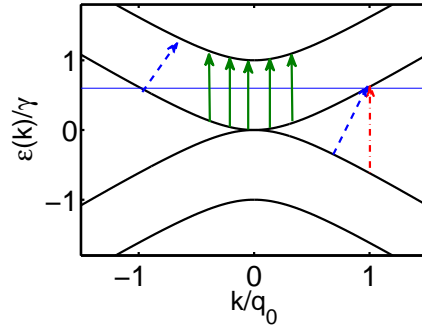


Figure 4.1: The band-structure of bilayer graphene. The two upper bands (as well as the two lower bands) are perfectly nested and separated by $\gamma \sim 0.4$ eV; $q_0 = \gamma/\hbar v_F$. Horizontal line depicts one possible value of the Fermi level, and arrows denote some of the possible interband electronic transitions. See text for details.

In order to calculate the imaginary part of the conductivity, we employ Kramers-Kronig relations and the calculation of absorption by Nicol and Carbotte [49], where $\Re\sigma(\omega)$ [see Eqs. (19)-(21) in Ref. [49]] was calculated by using the Kubo formula. The optical conductivity has rich structure due to the fact that the single-particle spectrum of graphene is organized in four bands given by [49],

$$\frac{\epsilon(\mathbf{k})}{\gamma} = \pm \sqrt{\frac{1}{4} + \left(\frac{\hbar v_F k}{\gamma}\right)^2} \pm \frac{1}{2}, \quad (4.3)$$

where $v_F = 10^6$ m/s, the parameter $\gamma \approx 0.4$ eV is equal to the separation between the two conduction bands (which is equal to the separation between the valence bands). The band structure (4.3) is calculated from the tight binding approach, where v_F is connected to the nearest-neighbour hopping terms for electrons to move in each of the two graphene planes, and the distance between Carbon atoms in one monolayer (see Ref. [49]), whereas γ is the hopping parameter corresponding to electrons hopping from one layer to the other and vice versa [49]. The two graphene layers are stacked one above the other according to the so-called Bernal-type stacking (e.g., see Ref. [50]). We emphasize that the perfect nesting of bands gives rise to the stronger plasmon like features of TE plasmons in bilayer than in monolayer graphene. The four bands are illustrated in Fig. 4.1 along with some of the electronic transitions which result in absorption. Absorption depends on γ and the Fermi level μ ; the latter can be changed by applying external bias voltage.

The imaginary part of the conductivity can be calculated from $\Re\sigma(\omega)$ by using the Kramers-Kronig relations

$$\Im\sigma(\omega) = -\frac{2\omega}{\pi} \mathcal{P} \int_0^\infty \frac{\Re\sigma(\omega')}{\omega'^2 - \omega^2} d\omega', \quad (4.4)$$

which yields

$$\begin{aligned}
\frac{\Im\sigma(\omega)}{\sigma_0} &= f(\Omega, 2\mu) + g(\Omega, \mu, \gamma) \\
&+ [f(\Omega, 2\gamma) + g(\Omega, \gamma, -\gamma)]\Theta(\gamma - \mu) \\
&+ [f(\Omega, 2\mu) + g(\Omega, \mu, -\gamma)]\Theta(\mu - \gamma) \\
&+ \frac{\gamma^2}{\Omega^2} \left[\frac{\Omega}{\pi(2\mu + \gamma)} + f(\Omega, 2\mu + \gamma) \right] \\
&+ \frac{\gamma^2}{\Omega^2} \left[\frac{\Omega}{\pi\gamma} + f(\Omega, \gamma) \right] \Theta(\gamma - \mu) \\
&+ \frac{\gamma^2}{\Omega^2} \left[\frac{\Omega}{\pi(2\mu - \gamma)} + f(\Omega, 2\mu - \gamma) \right] \Theta(\mu - \gamma) \\
&+ \frac{a(\mu)}{\pi\Omega} + \frac{2\Omega b(\mu)}{\pi(\Omega^2 - \gamma^2)}, \tag{4.5}
\end{aligned}$$

where

$$\begin{aligned}
f(x, y) &= \frac{1}{2\pi} \log \left| \frac{x - y}{x + y} \right|, \\
g(x, y, z) &= \frac{z}{2\pi} \frac{(x - z) \log |x - 2y| + (x + z) \log |x + 2y| - 2x \log |2y + z|}{x^2 - z^2}, \\
a(\mu) &= \frac{4\mu(\mu + \gamma)}{2\mu + \gamma} + \frac{4\mu(\mu - \gamma)}{2\mu - \gamma} \Theta(\mu - \gamma), \\
b(\mu) &= \frac{\gamma}{2} \left[\log \frac{2\mu + \gamma}{\gamma} - \log \frac{2\mu - \gamma}{\gamma} \Theta(\mu - \gamma) \right], \tag{4.6}
\end{aligned}$$

$\sigma_0 = e^2/2\hbar$, $\Theta(x) = 1$ if $x \geq 0$ and zero otherwise, and $\Omega = \hbar\omega$. Here we assume zero temperature $T \approx 0$, which is a good approximation for sufficiently doped bilayer graphene where $\mu \gg k_B T$. Formulae (4.5) and (4.6) are used to describe the properties of TE plasmons.

In Figure 4.2 we show the real and imaginary part of the conductivity for two different values of the Fermi level: $\mu = 0.4\gamma$ and $\mu = 0.9\gamma$ (we focus on the electron doped system $\mu > 0$). Because plasmons are strongly damped by interband transitions, it is instructive at this point to discuss the kinematical requirements for the excitation of electron-hole pairs. If the doping is such that $\mu < \gamma/2$, a quantum of energy $\hbar\omega$ (plasmon or photon) with in-plane momentum $q = 0$ can excite an electron-hole pair only if $\hbar\omega > 2\mu$ (excitations from the upper valence to the lower conduction band shown as red dot-dashed

line in Fig. 4.1). If $\mu > \gamma/2$, the $(q = 0, \omega)$ -quantum can excite an electron-hole pair only for $\hbar\omega \geq \gamma$ (excitations from the lower to the upper conduction band shown as green solid lines in Fig. 4.1 occur at $\hbar\omega = \gamma$). If the plasmon/photon has in-plane momentum q larger than zero, then interband transitions are possible for smaller frequencies (see blue dashed lines in Fig. 4.1). There is a region in the (q, ω) -plane where electron-hole excitations are forbidden due to the Pauli principle. Because plasmons are strongly damped by these interband transitions (this is Landau damping), in our search for the TE plasmons, we focus on their dispersion curve in the regime where electron-hole pair formation is inadmissible (via first-order transition).

4.2 Transverse-electric plasmon dispersion in bilayer graphene

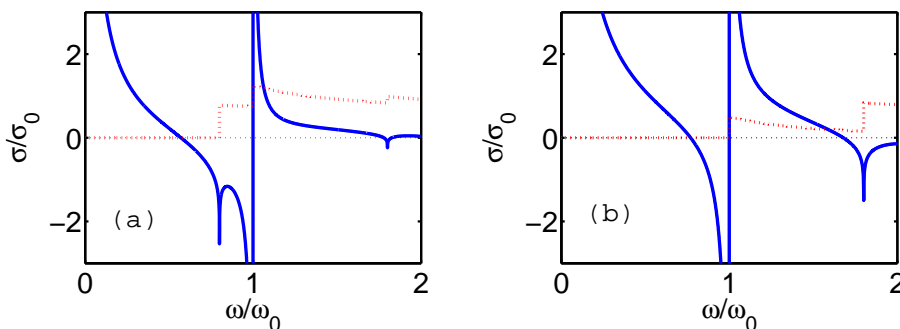


Figure 4.2: The real (red dotted lines) and imaginary (blue solid lines) part of the conductivity of bilayer graphene for two values of doping: $\mu = 0.4\gamma$ (a), and $\mu = 0.9\gamma$ (b). The conductivity is in units of $\sigma_0 = e^2/2\hbar$, and the frequency is in units of $\omega_0 = \gamma/\hbar$. The δ -functions in $\Re\sigma(\omega)$ at $\omega = 0$ (intraband transitions) and $\omega = \gamma/\hbar$ (transitions from the lower to the upper conduction band depicted as green solid arrows in Fig. 4.1) are not shown (see [49]).

In Figure 4.3 we show the plasmon dispersion curves for $\mu = 0.4\gamma$ and $\mu = 0.9\gamma$; in the spirit of Ref. [48], we show $\Delta q = q - \omega/c$ as a function of frequency ω . Plasmons are very close to the light line and thus one can to a

very good approximation write the dispersion curve as

$$\Delta q \approx \frac{\omega}{8\epsilon_0^2 c^3} \Im\sigma(\omega)^2. \quad (4.7)$$

To the left (right) of the vertical red dotted line in Fig. 4.3, plasmon damping via excitation of electron-hole pairs is (is not) forbidden.

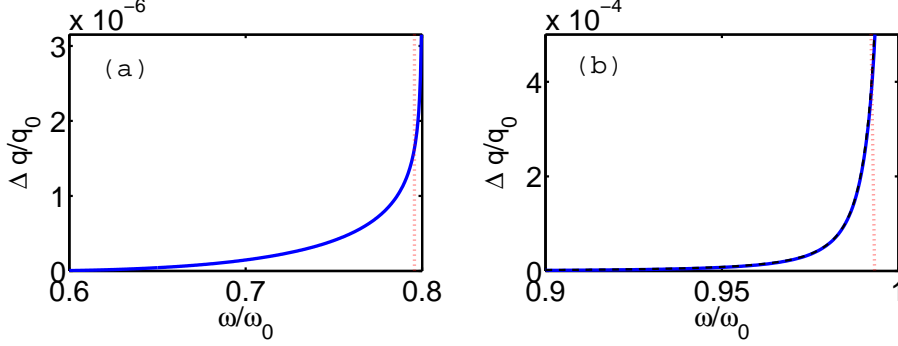


Figure 4.3: The plasmon dispersion curve $\Delta q = q - \omega/c$ vs. ω for $\mu = 0.4\gamma$ (a), and $\mu = 0.9\gamma$ (b) is shown as blue solid line. To the right of the vertical red dotted lines plasmons can be damped via excitation of electron-hole pairs, whereas to the left of this line these excitations are forbidden due to the Pauli principle. Black dashed line in (b) (which closely follows the blue line) corresponds to Eq. (4.8). The wave vector is in units of $q_0 = \gamma/\hbar v_F$, and the frequency is in units of $\omega_0 = \gamma/\hbar$.

For $\mu = 0.4\gamma$, $\Im\sigma(\omega)$ is smaller than zero for ω in an interval of frequencies just below 2μ . From the leading term in $\Im\sigma(\omega)$ we find that departure of the dispersion curve from the light line is logarithmically slow: $\Delta q_{0 < \mu < \gamma/2} \propto [\log |\hbar\omega - 2\mu|]^2$. The same type of behavior occurs in monolayer graphene [48].

However, for $\mu = 0.9\gamma$, one can see the advantage of bilayer over monolayer graphene in the context of TE plasmons. The conductivity $\Im\sigma(\omega)$ is smaller than zero in an interval of frequencies below γ . In this interval, the most dominant term to the conductivity is the last one from Eq. (4.5), that is,

$$\Delta q_{\gamma/2 < \mu < \gamma} \approx \frac{\omega\sigma_0^2}{2\pi^2\epsilon_0^2 c^3} \left[\frac{\hbar\omega b(\mu)}{\gamma^2 - (\hbar\omega)^2} \right]^2. \quad (4.8)$$

This approximation is illustrated with black dashed line in Fig. 4.3, and it almost perfectly matches the dispersion curve. Note that the singularity in $\Im\sigma(\omega)$ at $\hbar\omega = \gamma$ is of the form $1/(\gamma - \hbar\omega)$, whereas the singularity at $\hbar\omega = 2\mu$

is logarithmic (as in monolayer graphene [48]). As a consequence, the departure of the dispersion curve from the light line in bilayer graphene is much faster for $\mu > \gamma/2$ than for $\mu < \gamma/2$, and it is faster than in monolayer graphene as well [note the two orders of magnitude difference between the abscissa scales in Figs. 4.3(a) and (b)]. Thus, we conclude that more pronounced plasmonic features of TE plasmons (shrinking of wave length which is measured as departure of q from the light line) can be obtained in bilayer graphene. The term in $\Im\sigma(\omega)$ which is responsible for TE plasmons for $\mu > \gamma/2$ corresponds (via Kramers-Kronig relations) to the absorption term $b(\mu)\delta(\hbar\omega - \gamma)$ [49], which arises from the transitions from the first to the second valence band (shown as green solid arrows in Fig. 4.1), which are perfectly nested and separated by γ . Thus, this unique feature of bilayer graphene gives rise to TE plasmons with more pronounced plasmon like features than in monolayer graphene.

Before closing this chapter, let us discuss some properties and possible observation of TE plasmons. First, note that since the electric field oscillations are both perpendicular to the propagation vector \mathbf{q} , and lie in the bilayer graphene plane, the electric current $\mathbf{j} = \sigma(\omega)\mathbf{E}$ is also perpendicular to \mathbf{q} . Thus, $\mathbf{j} \cdot \mathbf{q} = 0$, and the equation of continuity yields that the charge density is zero (i.e., one has self-sustained oscillations of the current). In order to excite plasmons of frequency ω with light of the same frequency, one has to somehow account for the conservation of the momentum which is larger for plasmons. Since the momentum mismatch is relatively small, the standard plasmon excitation schemes such as the prism or grating coupling methods (e.g., see [12] and references therein) could be used for the excitation of these plasmons.

To conclude this chapter, we have predicted the existence of transverse electric (TE) plasmons in bilayer graphene. Since they exist very close to the light line, these plasmons are expected to show strong polariton character, i.e., mixing with photon modes. However, due to the perfectly nested valence bands of bilayer graphene, their dispersion departs much more from the light line than in monolayer graphene.

Chapter 5

Plasmon-phonon coupling

In this chapter we analyze the coupling of plasmons with intrinsic optical phonons in graphene by using the self-consistent linear response formalism. We find that longitudinal plasmons (LP) couple only to transverse optical (TO) phonons, while transverse plasmons (TP) couple only to longitudinal optical (LO) phonons. The LP-TO coupling is stronger for larger concentration of carriers, in contrast to the TP-LO coupling (which is fairly weak). The former could be measured via current experimental techniques. Thus, plasmon-phonon resonance could serve as a magnifier for exploring the electron-phonon interaction, and for novel electronic control (by externally applied voltage) over crystal lattice vibrations in graphene.

To analyze plasmon-phonon coupling let us start with the Hamiltonian for the Dirac electrons in graphene

$$H_e = \hbar v_F \boldsymbol{\sigma} \cdot \mathbf{k}, \quad (5.1)$$

where $v_F = 10^6$ m/s, $\mathbf{k} = (k_x, k_y) = -i\nabla$ is the wave-vector operator, $\boldsymbol{\sigma} = (\sigma_x, \sigma_y)$, and $\sigma_{x,y}$ are the Pauli spin matrices. We label the eigenstates of Hamiltonian H_e by $|s, \mathbf{k}\rangle$ and the appropriate eigenvalues by $E_{s,\mathbf{k}} = s\hbar v_F |\mathbf{k}|$, where $s = 1$ for the conduction band and $s = -1$ for the valence band.

The long-wavelength in-plane optical phonon branch in graphene consists of two modes (LO and TO) which are effectively dispersionless and degenerate at energy $\hbar\omega_0 = 0.196eV$. Let $\mathbf{u}(\mathbf{R}) = [\mathbf{u}_A(\mathbf{R}) - \mathbf{u}_B(\mathbf{R})]/\sqrt{2}$ denote the relative displacements of the sub-lattice atoms A and B of a unit cell specified by a coordinate \mathbf{R} [see Fig. 5.1(c)]. Then, in the long-wavelength limit \mathbf{R} can be

replaced by a continuous coordinate \mathbf{r} and we have

$$\mathbf{u}(\mathbf{r}) = \sum_{\mu\mathbf{q}} \frac{1}{\sqrt{NM}} Q_{\mu\mathbf{q}} \mathbf{e}_{\mu\mathbf{q}} e^{i\mathbf{q}\mathbf{r}}, \quad (5.2)$$

where N is the number of unit cells, M is the carbon atom mass, $\mathbf{q} = q(\cos\phi_{\mathbf{q}}, \sin\phi_{\mathbf{q}})$ is the phonon wave vector, $\mu = L, T$ stands for the polarization, and the polarization unit vectors are $\mathbf{e}_{L\mathbf{q}} = i(\cos\phi_{\mathbf{q}}, \sin\phi_{\mathbf{q}})$, and $\mathbf{e}_{T\mathbf{q}} = i(-\sin\phi_{\mathbf{q}}, \cos\phi_{\mathbf{q}})$. The displacement vector $\mathbf{u}(\mathbf{r})$ is parallel (perpendicular) to the phonon propagation wave vector \mathbf{q} for LO (TO, respectively) phonons [see Fig. 5.1(c)]. The phonon Hamiltonian is given by

$$H_{ph} = \frac{1}{2} \sum_{\mu\mathbf{q}} (P_{\mu\mathbf{q}}^\dagger P_{\mu\mathbf{q}} + \omega_0^2 Q_{\mu\mathbf{q}}^\dagger Q_{\mu\mathbf{q}}), \quad (5.3)$$

where $Q_{\mu\mathbf{q}}$ and $P_{\mu\mathbf{q}}$ denote phonon coordinate and momentum. The electron-phonon interaction takes a peculiar form in graphene (see chapter 2):

$$H_{e-ph} = -\sqrt{2} \frac{\beta \hbar v_F}{b^2} \boldsymbol{\sigma} \times \mathbf{u}(\mathbf{r}), \quad (5.4)$$

where $\boldsymbol{\sigma} \times \mathbf{u} = \sigma_x u_y - \sigma_y u_x$, $b = 0.142$ nm is the nearest carbon atoms distance, and $\beta = 2$. We find it convenient to write Eq. (5.4) as

$$H_{e-ph} = L^2 F \sum_{\mu\mathbf{q}} \mathbf{j}_{\mathbf{q}}^\dagger \times \mathbf{e}_{\mu\mathbf{q}} Q_{\mu\mathbf{q}} \quad (5.5)$$

where $\mathbf{j}_{\mathbf{q}} = -ev_F L^{-2} \boldsymbol{\sigma} e^{-i\mathbf{q}\mathbf{r}}$ is the single-particle current-density operator, L^2 is the area of the system, e is charge of the electron, and $F = \frac{\sqrt{2}\beta\hbar}{eb^2\sqrt{NM}}$.

The electromagnetic field in the plane of graphene is completely described by the vector potential $\mathbf{A} = \sum_{\mu\mathbf{q}} \mathbf{e}_{\mu\mathbf{q}} A_{\mu\mathbf{q}} e^{i\mathbf{q}\mathbf{r}}$ (scalar potential is gauged to zero, time dependence is implicitly assumed, and $\mu = L, T$ denote polarizations). The interaction with Dirac electrons is obtained by substitution $\hbar\mathbf{k} \rightarrow \hbar\mathbf{k} + e\mathbf{A}$ in Eq. (5.1), which leads to

$$H_{e-em} = ev_F \boldsymbol{\sigma} \cdot \mathbf{A} = -L^2 \sum_{\mu\mathbf{q}} \mathbf{j}_{\mathbf{q}}^\dagger \cdot \mathbf{e}_{\mu\mathbf{q}} A_{\mu\mathbf{q}}. \quad (5.6)$$

By comparing Eqs. (5.4) and (5.6) it follows that electron-phonon interaction

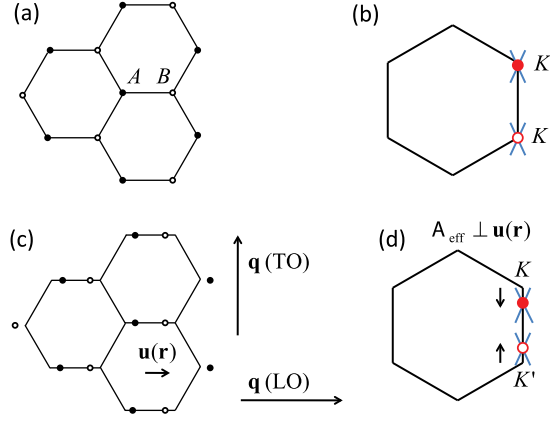


Figure 5.1: (a) Schematic illustration of the lattice structure with two sublattices (A and B). (b) The two degenerate Dirac cones are centered at K and K' points at the edge of the Brillouin zone. (c) A displacement of lattice atoms $\mathbf{u}(\mathbf{r})$ is parallel (perpendicular) to the propagation wave vector \mathbf{q} of a LO (TO) phonon. (d) The displacement $\mathbf{u}(\mathbf{r})$ creates an effective vector potential \mathbf{A}_{eff} perpendicular to $\mathbf{u}(\mathbf{r})$ (the sign of \mathbf{A}_{eff} for the K' point is opposite to that for the K point).

can be regarded as a presence of an effective vector potential

$$\mathbf{A}_{\text{eff}} = F \sum_{\mathbf{q}} (\mathbf{e}_{T\mathbf{q}} Q_{L\mathbf{q}} - \mathbf{e}_{L\mathbf{q}} Q_{T\mathbf{q}}) e^{i\mathbf{q}\mathbf{r}}, \quad (5.7)$$

that is, $H_{e-ph} = ev_F \boldsymbol{\sigma} \cdot \mathbf{A}_{\text{eff}}$. It is evident that $\mathbf{A}_{\text{eff}} \cdot \mathbf{u}(\mathbf{r}) = 0$ that is the effective vector potential \mathbf{A}_{eff} is perpendicular to $\mathbf{u}(\mathbf{r})$ as illustrated in Figs. 5.1(c) and (d) (see also Ref. [50]), which is responsible for the mixing of polarizations in plasmon-phonon coupling.

As a first pass, let us ignore the phonons and focus on the Hamiltonian $H = H_e + H_{e-em}$. Without an external perturbation, the electrons in graphene fill the Fermi sea according to the Fermi distribution function $f_{s\mathbf{k}}$. A field $A_{\mu\mathbf{q}}(\omega)$ oscillating at frequency ω will induce an average current density (up to a linear order in the vector potential)

$$\langle J_{\mu}(\mathbf{q}, \omega) \rangle = -\chi_{\mu}(\mathbf{q}, \omega) A_{\mu\mathbf{q}}(\omega), \quad (5.8)$$

where the current-current response function (including 2-spin and 2-valley de-

generacy) is given by [56]

$$\chi_\mu(\mathbf{q}, \omega) = 4L^2 \sum_{s_1 s_2 \mathbf{k}} \frac{f_{s_1 \mathbf{k}} - f_{s_2 \mathbf{k} + \mathbf{q}}}{\hbar\omega + \hbar\omega_{s_1 \mathbf{k}} - \hbar\omega_{s_2 \mathbf{k} + \mathbf{q}} + i\eta} \times |\langle s_1 \mathbf{k} | \mathbf{j}_{\mathbf{q}} \cdot \mathbf{e}_{\mu \mathbf{q}}^* | s_2 \mathbf{k} + \mathbf{q} \rangle|^2. \quad (5.9)$$

For the response function $\chi_\mu(\mathbf{q}, \omega)$ we utilize the analytical expression from Ref. [54]. The subtlety involved with the divergence in Eq. (5.9) is solved by subtracting from $\chi_L(\mathbf{q}, \omega)$ [$\chi_T(\mathbf{q}, \omega)$] the value $\chi_L(\mathbf{q}, \omega = 0)$ [$\chi_T(\mathbf{q} \rightarrow 0, \omega = 0)$] to take into account that there is no current response to the longitudinal [transverse] time [time and space] independent vector potential, see [54, 55] for details. We would like to note that when working with the current-current response function, rather than with the density-density response function, the nature of the plasmon-phonon interaction (especially the mixing of polarizations as shown below) is far more transparent.

Next, it is straightforward to show from the Maxwell equations that an electric current oscillating in a two-dimensional plane will induce a vector potential

$$\langle A_{L\mathbf{q}}(\omega) \rangle = \langle J_L(\mathbf{q}, \omega) \rangle \frac{\sqrt{q^2 - \omega^2/c^2}}{-2\omega^2\epsilon_0}, \quad (5.10)$$

and

$$\langle A_{T\mathbf{q}}(\omega) \rangle = \langle J_T(\mathbf{q}, \omega) \rangle \frac{\mu_0}{2\sqrt{q^2 - \omega^2/c^2}}, \quad (5.11)$$

where we have assumed that graphene is suspended in air and that there are no other sources present in space. This induced vector potential in turn acts on electrons in graphene through the interaction Hamiltonian H_{e-em} which can result in plasmons - self-sustained collective oscillations of electrons. From Eqs. (5.8) and (5.10) we get the dispersion relation for longitudinal plasmons [40, 41]

$$1 - \frac{\sqrt{q^2 - \omega^2/c^2}}{2\omega^2\epsilon_0} \chi_L(\mathbf{q}, \omega) = 0. \quad (5.12)$$

From Eqs. (5.8) and (5.11) we get the dispersion relation for transverse plasmons [48]

$$1 + \frac{\mu_0}{2\sqrt{q^2 - \omega^2/c^2}} \chi_T(\mathbf{q}, \omega) = 0. \quad (5.13)$$

Longitudinal plasmons are also referred to as transverse magnetic modes since

they are accompanied by a longitudinal electric (E) and a transverse magnetic field (B) in the plane of graphene. Likewise transverse plasmons or transverse electric modes are accompanied by a transverse electric and a longitudinal magnetic field [48]. Dispersion relation of LP (TP) modes is shown by the blue dashed line in Fig. 5.2. (Fig. 5.3, respectively). Finally we note that we are primarily interested in non-radiative modes ($q > \omega/c$) in which case fields are localized near the graphene plane ($z = 0$) and decay exponentially: $E(z), B(z) \propto e^{-|z|\sqrt{q^2 - \omega^2/c^2}}$.

In order to find the plasmon-phonon coupled excitations we consider the complete Hamiltonian $H = H_e + H_{e-em} + H_{e-ph} + H_{ph}$. We assume that the hybrid plasmon phonon mode oscillates at some frequency ω with wavevector q (which are to be found). From the equation of motion for the phonon amplitudes $Q_{\mu\mathbf{q}}$ one finds [56]

$$(\omega^2 - \omega_0^2)\langle Q_{T\mathbf{q}} \rangle = L^2 F \langle J_L(\mathbf{q}, \omega) \rangle, \quad (5.14)$$

and

$$(\omega^2 - \omega_0^2)\langle Q_{L\mathbf{q}} \rangle = -L^2 F \langle J_T(\mathbf{q}, \omega) \rangle. \quad (5.15)$$

The electron phonon interaction (5.5) is included as the effective vector potential (5.7) in Eq. (5.6), which from Eq. (5.8) immediately yields

$$\langle J_L(\mathbf{q}, \omega) \rangle = \chi_L(\mathbf{q}, \omega)(-\langle A_{L\mathbf{q}}(\omega) \rangle + F \langle Q_{T\mathbf{q}} \rangle), \quad (5.16)$$

and

$$\langle J_T(\mathbf{q}, \omega) \rangle = \chi_T(\mathbf{q}, \omega)(-\langle A_{T\mathbf{q}}(\omega) \rangle - F \langle Q_{L\mathbf{q}} \rangle). \quad (5.17)$$

From Eqs. (5.14) - (5.17) it is clear that transverse (longitudinal) phonons couple only to longitudinal (transverse) plasmons. Apparently, this follows from the fact that LO (TO, respectively) phonons are equivalent to oscillations of an effective vector potential \mathbf{A}_{eff} [see Eq. (5.7)], and therefore an effective electric field, perpendicular (parallel, respectively) to \mathbf{q} .

Finally using Eqs. (5.10), (5.14), and (5.16) we get the dispersion relation for the LP-TO coupled mode

$$\omega^2 - \omega_0^2 = \frac{L^2 F^2 \chi_L(\mathbf{q}, \omega)}{1 - \frac{\sqrt{q^2 - \omega^2/c^2}}{2\omega^2 \epsilon_0} \chi_L(\mathbf{q}, \omega)}, \quad (5.18)$$

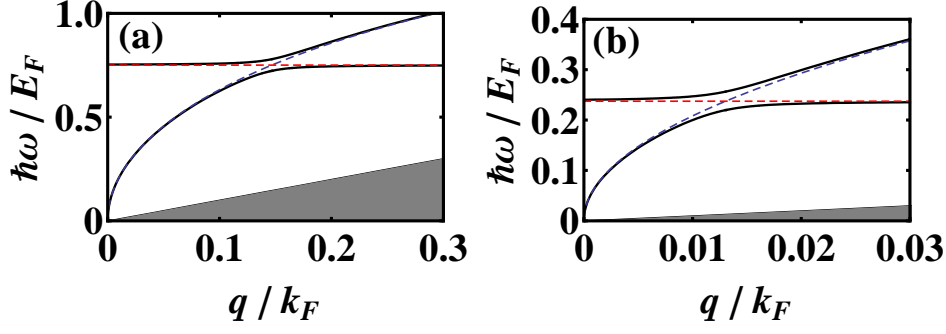


Figure 5.2: Dispersion lines of hybrid LP-TO plasmon-phonon modes (solid lines) and of the uncoupled modes (dashed lines) for two values of doping: (a) $n = 5 \times 10^{12} \text{ cm}^{-2}$, and (b) $n = 5 \times 10^{13} \text{ cm}^{-2}$. The hybridization is stronger for larger doping values. Grey areas denote the region of single-particle damping.

and from Eqs. (5.11), (5.15), and (5.17) dispersion relation for the TP-LO coupled mode

$$\omega^2 - \omega_0^2 = \frac{L^2 F^2 \chi_T(\mathbf{q}, \omega)}{1 + \frac{\mu_0}{2\sqrt{q^2 - \omega^2/c^2}} \chi_T(\mathbf{q}, \omega)}. \quad (5.19)$$

The plasmon dispersions relations (5.12) and (5.13) appear as poles in the Eqs. (5.18) and (5.19) for the coupled modes, which means that the coupling is greatest at the resonance point where plasmon momentum and energy match that of the appropriate phonon mode. We denote this point (where the uncoupled plasmon and phonon dispersion cross) by (q_c, ω_0) . One can quantify the strength of the coupling effect by calculating the frequency difference between the hybrid modes at the wavevector q_c in units of the uncoupled frequency value: $\Delta\omega/\omega_0$. Finally by doping one can change plasmon dispersion which in turn changes q_c and the strength of the plasmon-phonon coupling.

The dispersion lines for the hybrid LP-TO modes are shown in Fig. 5.2 for two values of doping, (a) $n = 5 \times 10^{12} \text{ cm}^{-2}$, $E_F = 0.261 \text{ eV}$, $k_F = 3.96 \times 10^8 \text{ m}^{-1}$, and (b) $n = 5 \times 10^{13} \text{ cm}^{-2}$, $E_F = 0.825 \text{ eV}$, $k_F = 1.25 \times 10^9 \text{ m}^{-1}$. The strength of the coupling increases with increasing values of doping, and one has for the case (a) $\Delta\omega/\omega_0 = 7.5\%$, and (b) $\Delta\omega/\omega_0 = 15.5\%$. To describe graphene sitting on a substrate (say SiC, which is a polar material), one only needs to include the dielectric function of the substrate into our calculation. In that case plasmons can also couple to surface phonon modes of the polar substrate [57]. However, since these surface phonons have sufficiently smaller

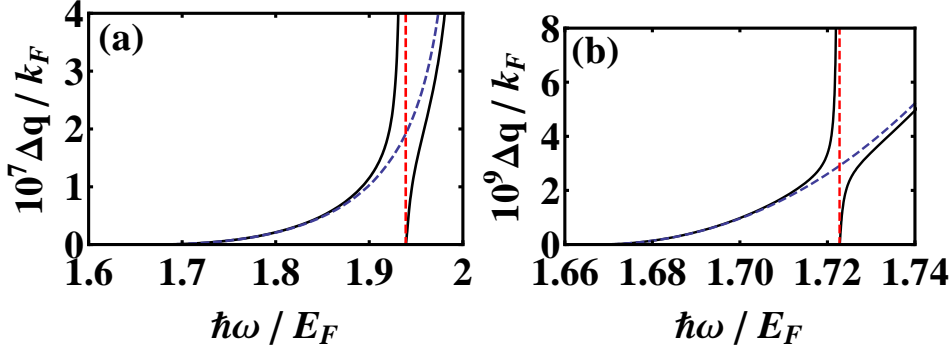


Figure 5.3: Dispersion lines of hybrid TP-LO plasmon-phonon modes (solid lines) and of the uncoupled modes (dashed lines) for two values of doping: (a) $n = 7.5 \times 10^{11} \text{ cm}^{-2}$, and (b) $n = 9.5 \times 10^{11} \text{ cm}^{-2}$. The plasmon-like dispersion is very close to the light line $q = \omega/c$; therefore, the ordinate shows $\Delta q = q - \omega/c$.

energies than optical phonons in graphene our results are qualitatively unchanged in that case. LP-TO hybrid modes could be measured by observing the change in the phonon dispersion with the Neutron Spectroscopy or Inelastic X-ray Scattering. Alternatively, one could use grating coupler or Electron Energy Loss Spectroscopy to measure the shift in the plasmon energy. Our results imply that plasmon-phonon coupling could serve to explore the electron-phonon interaction (the frequency shifts at resonance are much larger than the G peak shift recently measured by Raman Spectroscopy [32]), and that by externally applying voltage one can influence the properties of lattice vibrations.

In spite of the fact that the formal derivation of hybrid TP-LO coupled modes is equivalent to the derivation of the LP-TO modes, their properties qualitatively differ. First, we note that the dispersion of transverse plasmons is extremely close to the light line, and we plot $\Delta q = q - \omega/c$ vs. frequency ω following Ref. [48]. For this reason, transverse plasmons are expected to have strong polariton character and they will be hard to distinguish from free photons (also, even a small plasmon linewidth will obscure the distinction). Moreover, they do not exist in graphene between two dielectrics with sufficiently different relative permittivity, where the light lines for the dielectrics are separated. Next, transverse plasmons exist only in the frequency interval $2E_F > \hbar\omega > 1.667E_F$ [48], which means that the LO phonon energy

must be in the same interval for the hybridization to occur. Figure 5.3 shows the dispersion curves of the hybrid TP-LO modes for two values of doping, (a) $n = 7.5 \times 10^{11} \text{ cm}^{-2}$, $E_F = 0.101 \text{ eV}$, $k_F = 1.53 \times 10^8 \text{ m}^{-1}$, and (b) $n = 9.5 \times 10^{11} \text{ cm}^{-2}$, $E_F = 0.114 \text{ eV}$, $k_F = 1.73 \times 10^8 \text{ m}^{-1}$. We observe that the trend here is opposite to that of the LP-TO coupling, as the strength of the coupling decreases with increasing doping; specifically, one has for the case (a) $\Delta\omega/\omega_0 = 0.17\%$, and (b) $\Delta\omega/\omega_0 = 0.02\%$. The maximal coupling occurs when $2E_F$ is just above $\hbar\omega_0$, and it is zero when $\hbar\omega_0 = 1.667E_F$. We emphasize that the strength of the coupling for TP-LO modes is in general much weaker than in LP-TO modes.

Before closing this chapter, we note another interesting result which is captured by our calculations. Equations (5.18) and (5.19) for shifts in the energies of TO and LO modes at $q = 0$ reduce to

$$\omega^2 - \omega_0^2 = \frac{L^2 F^2 \chi_{L,T}(0, \omega)}{1 + \frac{i}{2\omega\epsilon_0 c} \chi_{L,T}(0, \omega)}, \quad (5.20)$$

which is identical to the result of Ref. [51], where the coupling of optical phonons to single-particle excitations was studied, apart from the imaginary term in the denominator which is zero in [51]. This small but qualitative difference is consequence of phonon coupling to the radiative electromagnetic modes, which increases the phonon linewidth. For example, for the doping values of $n = 5 \times 10^{12} \text{ cm}^{-2}$, $5 \times 10^{13} \text{ cm}^{-2}$, and $5 \times 10^{14} \text{ cm}^{-2}$, Eq. (5.20) yields 0.005%, 0.07%, and 0.7%, respectively, for the linewidths, while there is no linewidth from single-particle damping at these doping values. This effect is qualitatively unchanged for graphene sitting on a substrate and could be measured by Raman spectroscopy. Finally, we note an interesting solution of Eq. (5.19) (valid for suspended graphene): when the hybrid TP-LO mode dispersion crosses the light line it has the same energy as the uncoupled phonon mode, i.e., $\omega = \omega_0$. In other words, LO phonon at a wavevector $q = \omega_0/c$ decouples from all (single particle and collective) electron excitations, while no such effect exists for the TO phonons.

In conclusion, we have predicted hybridization of plasmons and intrinsic optical phonons in graphene using self-consistent linear response theory. To the best of our knowledge, this is the first study of such resonance in an isolated 2D

material. We found that graphene's unique electron-phonon interaction leads to unconventional mixing of plasmon and optical phonon polarizations: longitudinal plasmons couple exclusively to transverse optical phonons, whereas graphene's transverse plasmons couple to longitudinal optical phonons; this contrasts plasmon-phonon coupling in all previously studied systems. The strength of the hybridization increases with doping in LP-TO coupled modes, while the trend is opposite for TP-LO modes. The LP-TO coupling is much stronger than TP-LO coupling, and it could be measured by current experiments, which would act as a magnifier for exploring the electron-phonon interaction in graphene. This coupling is an even more striking example of a breakdown of Born-Oppenheimer approximation in graphene than the recently measured stiffening of the Raman G peak [32]. Moreover, plasmon-phonon interaction can serve to electronically control the frequencies of lattice vibrations in graphene, which could have interesting technological implications.

Chapter 6

Near field heat transfer

6.1 Near field heat transfer between two graphene sheets

In this chapter we analyze the near field heat transfer between two graphene sheets mediated by thermally excited plasmon modes and demonstrate that there is a large enhancement of heat transfer compared to the far field black body radiation. The system we analyze, shown in figure 6.1, consists of a suspended graphene sheet at temperature T_1 emitting to another suspended graphene sheet held at room temperature $T_2 = 300K$, and a distance D away.

In chapter 2 we calculated the expression for the radiative heat exchange between two graphene sheets. Total heat transfer $H = H_{ff} + H_{nf}$ can be conveniently separated into the contribution from the propagating waves in the far field

$$H_{ff} = \frac{1}{\pi^2} \int_0^\infty d\omega [\Theta(\omega, T_1) - \Theta(\omega, T_2)] \int_0^{\omega/c} q dq \sum_{\mu} h_{ff}^{\mu}(q, \omega), \quad (6.1)$$

and evanescent waves in the near field

$$H_{nf} = \frac{1}{\pi^2} \int_0^\infty d\omega [\Theta(\omega, T_2) - \Theta(\omega, T_1)] \int_{\omega/c}^\infty q dq \sum_{\mu} h_{nf}^{\mu}(q, \omega). \quad (6.2)$$

Here $\Theta(\omega, T) = \hbar\omega / (e^{\beta\hbar\omega} - 1)$ is the Boltzman factor, μ stands for s or p

polarization and functions h_{ff}^μ and h_{nf}^μ are given by:

$$h_{ff}^\mu(\mathbf{q}, \omega) \equiv \frac{(1 - |r_1^\mu|^2 - |t_1^\mu|^2)(1 - |r_2^\mu|^2 - |t_2^\mu|^2)}{4|1 - r_1^\mu r_2^\mu e^{2i\gamma D}|^2}, \text{ and} \quad (6.3)$$

$$h_{nf}^\mu(\mathbf{q}, \omega) \equiv \frac{\Im r_1^\mu \Im r_2^\mu e^{-2|\gamma|D}}{|1 - r_1^\mu r_2^\mu e^{-2|\gamma|D}|^2}. \quad (6.4)$$

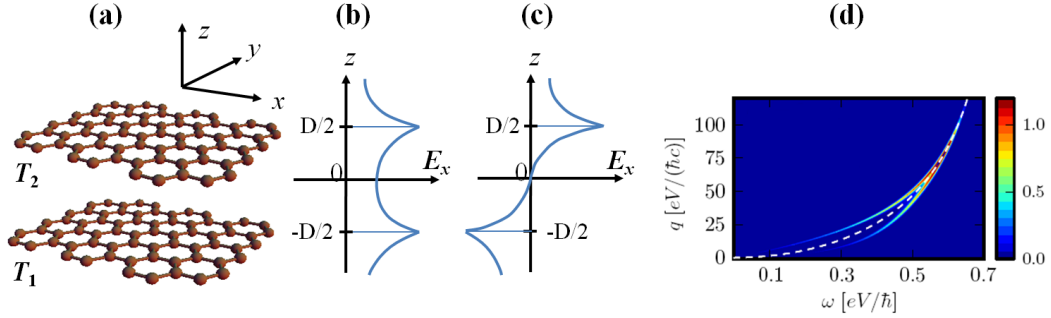


Figure 6.1: (a) Schematic diagram of the radiation transfer problem: a free standing sheet of graphene at temperature T_1 is radiating to another free standing graphene sheet at temperature T_2 and distance D away. (b) Schematic diagram of the field profile for even mode. (c) Odd mode. (d) Contour plot of the transfer function h_{nf}^p for the case of two graphene sheets at the same chemical potentials $\mu_{1,2} = 0.5eV$ and same temperatures $T_{1,2} = 300K$, separated by a distance of $D = 10$ nm. Dashed line denotes the plasmon dispersion relation for a single isolated graphene sheet, while poles of transfer function h_{nf}^p show dispersion relations of the coupled (even and odd) modes of the two sheets.

Let us first note that graphene is a poor absorber in the far field, since it is only one atom thick. Indeed, it was experimentally demonstrated [37] that graphene absorbs only $|a|^2 \approx 2\%$ of the incident light (see equation (2.77)). Since one can also write $|a|^2 = 1 - |r|^2 - |t|^2$ we can simply neglect the far field transfer (see equations (6.1) and (6.3)), at least compared to the black body case which is characterized by $|a_{BB}|^2 = 100\%$. On the other hand, we will see that near field heat transfer can be significantly greater than the black body case, if graphene sheets are sufficiently close to allow the tunneling of surface modes (plasmons).

To analyze the near field heat transfer between two graphene sheets let us write the p polarization reflection coefficient (2.131) for a single sheet as $r^p = (1 - \epsilon)/\epsilon$ where $\epsilon = 1 + \gamma\sigma/(2\epsilon_0\omega)$ is the dielectric function of graphene [61].

We immediately see that poles of r^p are located at the plasmon dispersion $\epsilon = 0$ which was derived in chapter 3 but we write it here again for the sake of clearance:

$$q = \epsilon_0 \frac{2i\omega}{\sigma(\omega, T)}. \quad (6.5)$$

We assumed here $\gamma = \sqrt{\omega^2/c^2 - q^2} \approx iq$ since we have shown that plasmon dispersion is mainly located in the non-retarded regime $q \gg \omega/c$. We have already pointed out that strong near field heat transfer requires graphene sheets to be very close, which in turn allows coupling of two plasmon modes (see figure 6.1). In the case when two graphene sheets have identical parameters ($r_1^p = r_2^p$) this coupling results in two new modes: even mode described by an equation $r^p = e^{qD}$, and an odd mode described by an equation $r^p = -e^{qD}$. Naturally, when sheets are sufficiently far apart ($D \gg \lambda$) or the wave vector is sufficiently large ($q \gg \omega/c$) so that the coupling becomes irrelevant, these two modes become degenerate again, described by a pole in r^p . Further on, note that these two equations can be joined in a single one: $1 - (r^p)^2 e^{-2qD} = 0$, which is precisely a denominator in equation (6.4) which determines the poles of the function h_{nf}^p . In other words, these two coupled surface modes, strongly enhance and dominate the near field heat transfer. Note however from equation (6.4) that $h_{nf}^p \propto e^{-2qD}$ so that graphene sheets have to be very close to have a significant near field heat transfer. In other words plasmon surface modes can act as an excellent heat conductors, only the graphene sheets have to be very close to allow the coupling of exponentially decaying ($E \propto e^{-qD}$) plasmon field.

Finally note that $h_{nf}^p \propto \Im r_1^p \Im r_2^p$, while $\Im r^p$ has a pole at the bare plasmon dispersion so there will be a competition between this factor and a pole at a dispersion of a coupled mode. Therefore the function h_{nf}^p will increase with increasing wave vector since the coupling between the modes will decrease and even/odd mode dispersion (and a corresponding pole) will join that of a bare plasmon (and a corresponding pole). However, when these dispersions meet ($q \approx 1/D$) the function h_{nf}^p will start to decrease with the wave vector due to exponentially decaying factor $h_{nf}^p \propto e^{-2qD}$. At last note that function h_{nf}^p is multiplied with a Boltzman factor $\Theta(\omega, T)$ which shifts everything to lower frequencies so there are several competing effects in action which will be hard to disentangle in the end when everything gets integrated over all q, ω values.

The same analysis applies to the s polarization however it is easy to see that

it will have a minor contribution to the total near field heat transfer. The reason for this is a large difference in the character of the plasmon dispersion relations (compare figure 5.2 and figure 5.3). On one hand longitudinal plasmons, described by a pole in r^p , are located in the non-retarded regime ($q \gg \omega/c$) with a large density of states, while transverse plasmons, describe by a pole in r^s , are located in the strongly retarded regime ($q \approx \omega/c$) with a tiny density of states. Since each q value can be thought of as a separate heat channel, and if graphene sheets are close enough so that all relevant q modes are active, the p polarization will have many more heat channels and dominate over the s polarization.

To model graphene we shall use q -independent conductivity which simplifies the mathematical calculations and gives a good order of magnitude on the heat transfer (see discussion below). In chapter 2 we showed that the total conductivity $\sigma(\omega) = \sigma_D(\omega) + \sigma_I(\omega)$, can be separated into Drude (intraband) and interband part, expressed respectively as (see also [61]):

$$\begin{aligned}\sigma_D(\omega) &= \frac{i}{\omega + i/\tau} \frac{e^2 2k_b T}{\pi \hbar^2} \ln \left[2 \cosh \frac{\mu}{2k_b T} \right] \\ \sigma_I(\omega) &= \frac{e^2}{4\hbar} \left[G \left(\frac{\hbar\omega}{2} \right) + i \frac{4\hbar\omega}{\pi} \int_0^\infty \frac{G(\epsilon) - G(\hbar\omega/2)}{(\hbar\omega)^2 - 4\epsilon^2} d\epsilon \right].\end{aligned}\tag{6.6}$$

where $G(\epsilon) = \sinh(\epsilon/k_b T) / (\cosh(\mu/k_b T) + \cosh(\epsilon/k_b T))$, and μ is the chemical potential. Various electron scattering processes are taken into account through the relaxation time τ . From DC mobility measurements in graphene, one obtains an order-of-magnitude value of $\tau \approx 10^{-13} s$. Now, due to fluctuation-dissipation theorem $h_{nf}^p \propto \Im r^p$ and $\Im r^p \propto \Re \sigma$ (see equation (2.147)), so we have to take particular attention to the origin of dissipation ($\Re \sigma$) in our system. At zero temperature the situation is very simple since Drude term (intraband contribution) and relaxation time τ determines the losses for low frequencies, while interband contribution is dominant for frequencies above the interband threshold ($\hbar\omega = 2\mu$). However, at finite temperature, interband processes can play a leading role even below the absorption threshold $\omega \approx 2\mu$, particularly for small chemical potential where thermal broadening of interband threshold (on the order of few $k_b T$) becomes more significant. While the use of q -independent expression for graphene conductivity (6.6) for intraband processes is a good approximation, one must take care when applying (6.6) to interband transi-

tions. Here, the contribution from the finite wave-vector becomes important since it broadens the interband threshold from 2μ to $2\mu - \hbar qv_F$. On the other hand, this is similar to finite temperature effects which also broaden the interband threshold, so we do not expect a qualitatively different result with q -dependent conductivity.

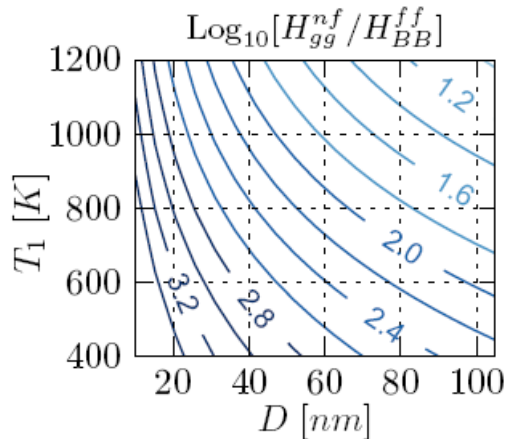


Figure 6.2: Contour plot of the near field heat transfer between two graphene sheets H_{gg}^{nf} normalized to the far field heat transfer between two black bodies H_{BB}^{ff} of the same temperatures, in the log scale. Here $T_2 = 300K$, $\mu_{1,2} = 0.1eV$ and $\tau_{1,2} = 10^{-13}s$.

To quantify the heat exchange in the near field we plot in figure 6.2 the total transfer H_{nf} (6.2) normalized to the transfer between two black bodies in the far field. Since the exponentially decaying Boltzmann factor shifts all the contributions to the lower frequencies we will focus on the small values of chemical potential. For $\mu_{1,2} = 0.1eV$, we observe orders-of-magnitude increase in heat exchange particularly at small separations ($\times 1000$ for $D = 20nm, T_1 = 800K$), but also at separations as large as $0.1\mu m$. In general, dependence of transfer on separation D is non-uniform and does not seem to yield a simple functional dependence on the emitter and absorber temperatures (as is the case for two black bodies). This efficient heat exchange between two graphene sheets in the near field, together with recently reported advances in hot carrier extraction from graphene [62], may offer a potential for a novel, hybrid thermophotovoltaic/thermoelectric solid-state heat-to-electricity conversion device.

6.2 Near field thermo-photo-voltaics using graphene as a thermal emitter

Here we show that graphene can be used as a thermal emitter in the near field thermo-photo-voltaic (TPV) system resulting in high efficiencies and power densities. The near field heat transfer is mediated by thermally excited plasmon modes in graphene similarly to the situation in the last section.

The system we analyze consists of a hot graphene emitter at a temperature T_1 and a photo-voltaic (PV) cell held at room temperature $T_2 = 300\text{K}$ and distance D away from graphene. It is interesting to note that the expression for the near field heat transfer between graphene and a PV cell is given by the same expression (6.2) for the graphene to graphene heat transfer

$$H_{nf} = \frac{1}{\pi^2} \int_0^\infty d\omega \left[\frac{\hbar\omega}{e^{\beta_1\hbar\omega} - 1} - \frac{\hbar\omega}{e^{\beta_2\hbar\omega} - 1} \right] \int_{\omega/c}^\infty q dq h_{nf}^p(q, \omega), \quad (6.7)$$

where

$$h_{nf}^p(\mathbf{q}, \omega) \equiv \frac{\Im r_1^p \Im r_2^p e^{-2qD}}{|1 - r_1^p r_2^p e^{-2qD}|^2}. \quad (6.8)$$

Here we have neglected the contribution from s polarization, and assumed $\gamma = \sqrt{\omega^2/c^2 - q^2} \approx iq$ since the near field heat transfer is mediated by graphene plasmon modes in the non-retarded regime ($q \gg \omega/c$). To model graphene we use q -independent conductivity $\sigma(\omega)$ from equation (6.6) as before, and the reflection coefficient is given by equation (2.131) which we write again for the sake of clearance:

$$r_1^p(q, \omega) = \frac{\frac{iq\sigma(\omega)}{2\epsilon_0\omega}}{1 + \frac{iq\sigma(\omega)}{2\epsilon_0\omega}}. \quad (6.9)$$

Above hot graphene emitter we now have PV cell which we model as a simple direct band-gap semiconductor with parameters:

$$\epsilon_2(\omega) = \left(n + i \frac{\alpha}{2k_0} \right)^2 \quad \text{where} \quad \alpha(\omega) = \begin{cases} 0 & , \omega < \omega_g \\ \alpha_0 \sqrt{\frac{\omega - \omega_g}{\omega_g}} & , \omega > \omega_g \end{cases} \quad (6.10)$$

Here n is the refractive index, $k_0 = 2\pi/\lambda = c/\omega$ is the photon wavelength in vacuum, and ω_g is the bandgap frequency. Specifically we will discuss the case of indium antimonide (InSb) with parameters $\omega_g = 0.17\text{eV}$ and $\alpha_0 \approx$

$0.7 \times 10^4 \text{cm}^{-1}$ (at room temperature [64]). Finally the reflection coefficient of the PV cell, in the non-retarded regime ($q \gg \omega/c$), is simply given by [67]

$$r_2^p(\omega) = \frac{\epsilon_2(\omega) - 1}{\epsilon_2(\omega) + 1}. \quad (6.11)$$

When the PV cell is biased at a voltage¹ V_o , we can express the total radiative power exchange as [65]

$$P_{rad} = \frac{1}{\pi^2} \int_0^\infty d\omega \left[\frac{\hbar\omega}{e^{\beta_1\hbar\omega} - 1} - \frac{\hbar\omega}{e^{\beta_2(\hbar\omega - V_o)} - 1} \right] \int_{\omega/c}^\infty qdq h_{nf}^p(q, \omega). \quad (6.12)$$

On the other hand we can also write the total photon flux into the PV cell as

$$j_{ph} = \frac{1}{\pi^2} \int_0^\infty d\omega \left[\frac{1}{e^{\beta_1\hbar\omega} - 1} - \frac{1}{e^{\beta_2(\hbar\omega - V_o)} - 1} \right] \int_{\omega/c}^\infty qdq h_{nf}^p(q, \omega). \quad (6.13)$$

In the Shockley-Queisser limit [69] of ideal PV cell, the only recombination of the charge carriers happens through the radiative processes so the electron current is simply: $j_e = ej_{ph}$. Then the electrical power generated in the PV cell is $P_{PV} = j_e V_o$, and efficiency of device is

$$\eta_{TPV} = \frac{P_{PV}}{P_{rad}} = \frac{ej_{ph}V_o}{P_{rad}}. \quad (6.14)$$

Let us now choose the graphene's chemical potential to be $\mu = 0.25$ eV, and that the PV cell is held at room temperature $T_2 = 300\text{K}$ and distance $D = 10$ nm away from the graphene sheet. Then for the case of graphene's temperature $T_1 = 600$ K and biased voltage $V_o = 0.08$ V, the output power density of our TPV device is $P_{PV}/A = 6$ W/cm² with an efficiency of $\eta = 35\%$. We note that these are remarkably high power densities considering that our thermal emitter is only one atom thick. To get a better sense of the scales involved we can compare the far field radiative power exchange P_{rad}^{BB} between two black bodies held at temperatures T_1 and T_2 but involving only the photons of energies above the given PV band gap, and the near field radiative power exchange P_{rad}^{gPV} between graphene and a PV cell held at these temperatures. For the

¹In general, the optimal voltage V_o depends on other parameters in the system. We avoid the full optimization procedure, and, motivated by the observed dependence of efficiency on V_o , choose a voltage slightly below the limit $V_o^{max} = \omega_g(1 - T_2/T_1)$.

temperatures $T_1 = 600$ K and $T_2 = 300$ K one obtains $P_{rad}^{gPV} / P_{rad}^{BB} = 62$ times increase over the black body case.

Further on, note that the near field heat transfer is particularly convenient since the energy is transferred by the evanescent modes and the photons with energy below the band gap, that are not absorbed by the PV cell, simply return to the graphene emitter as heat, unlike the far field case where they are lost in the form of propagating waves. This results in the high efficiencies $\eta = 35\%$, however note that these numbers are still below the Carnot limit $\eta = 50\%$ for temperatures $T_1 = 600$ K and $T_2 = 300$ K. The reason for this is the broad band plasmon spectrum contributing to the heat transfer with the high energy photons ($\omega > \omega_g$) wasting the energy difference ($\Delta E = \hbar\omega - \hbar\omega_g$) on the thermalization losses heating up the system.

To achieve even higher efficiencies one would need to tailor the emitter properties so that it selectively radiates only in the small interval around the band gap of the PV cell. One way to do this would be to use surface plasmons at metal-dielectric surface, since they have very large density of states around the surface plasmon resonance; see figure 3.1 b, and compare it to broad band spectrum of graphene plasmon mode from figure 3.2 d. However, the problem with metals is that surface plasmon resonance usually falls in the visible/ultraviolet regime which is impossible to excite thermally. Alternatively one could use highly doped semiconductors like Indium-Tin-Oxide [70] which has a resonance in the infra-red [71], however due to high doping level there is a lot of electron-impurity scattering and high losses result in reduced efficiencies. In that regards graphene TPV system shows large promise for a new temperature range (600–1200K) solid state energy conversion, where conventional thermoelectrics can not operate due to high temperatures and far field TPV schemes suffer from low efficiency and power density.

Chapter 7

Summary

We have explored light-matter interaction in graphene in the context of plasmonics and other technological applications but also used graphene as a platform to explore many body physics phenomena like the interaction between plasmons, phonons and other elementary excitations. Plasmons and plasmon-phonon interaction were analyzed within self-consistent linear response approximation. We demonstrated that electron-phonon interaction leads to large plasmon damping when plasmon energy exceeds that of the optical phonon but also a peculiar mixing of plasmon and optical phonon polarizations. Plasmon-phonon coupling is strongest when these two excitations have similar energy and momentum. We also analyzed properties of transverse electric plasmons in bilayer graphene. Finally we have showed that thermally excited plasmons strongly mediate and enhance the near field radiation transfer between two closely separated graphene sheets. We also demonstrated that graphene can be used as a thermal emitter in the near field thermophotovoltaics leading to large efficiencies and power densities. Near field heat transfer was analyzed withing the framework of fluctuational electrodynamics.

In Chapter 2 we presented analytical methods that were used throughout the text. We have derived electron band structure and electron-phonon interaction using the tight binding approximation. After that we derived the linear response functions (density-density and current-current) and used the fluctuation dissipation theorem to calculate the current-current correlation function induced by the thermal fluctuations in the system. Finally we employed these results to calculate radiative heat transfer between two graphene sheets.

In Chapter 3 we have investigated plasmons in doped graphene and demonstrated that they simultaneously enable low-losses and significant wave localization for frequencies of the light smaller than the optical phonon frequency $\hbar\omega_{Oph} \approx 0.2$ eV. Interband losses via emission of electron-hole pairs (1st order process) were shown to be blocked by sufficiently increasing the doping level, which pushes the interband threshold frequency ω_{inter} toward higher values (already experimentally achieved doping levels can push it even up to near infrared frequencies). The plasmon decay channel via emission of an optical phonon together with an electron-hole pair (2nd order process) is inactive for $\omega < \omega_{Oph}$ (due to energy conservation), however, for frequencies larger than ω_{Oph} this decay channel is non-negligible. This is particularly important for large enough doping values when the interband threshold ω_{inter} is above ω_{Oph} : in the interval $\omega_{Oph} < \omega < \omega_{inter}$ the 1st order process is suppressed, but the phonon decay channel is open.

In Chapter 4 we showed that graphene can also support unusual transverse electric plasmons and we predicted the existence of TE plasmons in bilayer graphene. We found that their plasmonic properties are much more pronounced in bilayer than in monolayer graphene, in a sense that the wavelength of TE plasmons in bilayer can be smaller than in monolayer graphene at the same frequency.

In Chapter 5 we analyzed the coupling of plasmons with intrinsic optical phonons in graphene by using the self-consistent linear response formalism. We found that longitudinal plasmons (LP) couple only to transverse optical (TO) phonons, while transverse plasmons (TP) couple only to longitudinal optical (LO) phonons. The LP-TO coupling is stronger for larger concentration of carriers, in contrast to the TP-LO coupling (which is fairly weak). The former could be measured via current experimental techniques. Thus, plasmon-phonon resonance could serve as a magnifier for exploring the electron-phonon interaction in graphene.

In Chapter 6 we analyzed the near field heat transfer between two graphene sheets mediated by thermally excited plasmon modes, and we demonstrated that there is a large enhancement of heat transfer compared to the far field black body radiation. Finally we showed that graphene can be used as a thermal emitter in the thermo-photo-voltaic system resulting in high device efficiencies and power densities.

Appendix A

Plasmon-phonon coupling in the context of Feynman diagrams

In this appendix we give alternative derivation of plasmon-phonon coupling in the context of Feynman diagrams. In that respect let us start by writing Coulomb potential

$$V(\mathbf{r}) = \frac{e^2}{4\pi\epsilon_0 r}, \quad (\text{A.1})$$

and its Fourier transform in two dimensions

$$V(\mathbf{q}) = \frac{e^2}{2\epsilon_0 q}. \quad (\text{A.2})$$

Bare Coulomb interaction $V(\mathbf{q})$ can polarize electron gas by creating electron-hole pair which in turn screens the bare interaction resulting with an effective interaction $W(\mathbf{q}, \omega)$. This process can happen several times in a row (see figure A.1) so we can write self-consistent equation for the effective interaction [66]

$$[-iW(\mathbf{q}, \omega)] = [-iV(\mathbf{q})] + [-iV(\mathbf{q})] [-i\Pi(\mathbf{q}, \omega)] [-iW(\mathbf{q}, \omega)]. \quad (\text{A.3})$$

If we now use the Random Phase Approximation which neglects higher order scattering of the created electron-hole pair, then the polarizability $\Pi(\mathbf{q}, \omega)$,

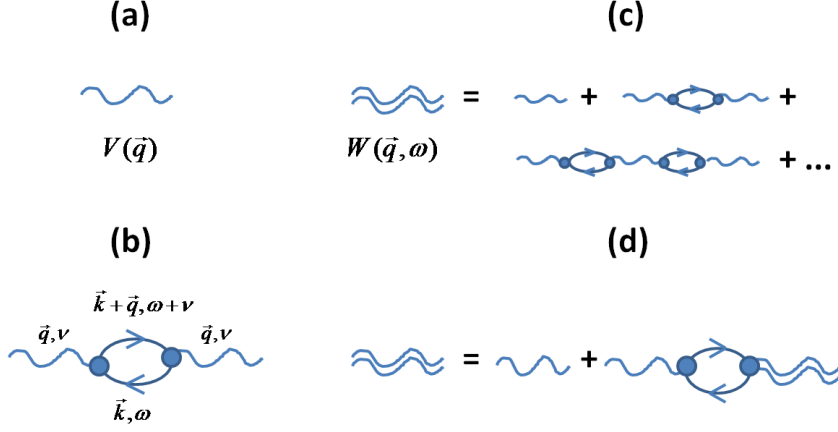


Figure A.1: (a) Feynman diagram for bare Coulomb interaction $V(\mathbf{q})$. (b) Polarizability $\Pi(\mathbf{q}, \omega)$. (c) and (d) Screened Coulomb interaction $W(\mathbf{q}, \omega)$ in the Random Phase Approximation.

depicted with a Feynman diagram in figure A.1 (b), can be written as

$$\begin{aligned}
 -i\Pi(\mathbf{q}, \omega) &= -4 \int \frac{d\mathbf{k}d\nu}{(2\pi)^3} \sum_{n, n'} iG_0(n', \mathbf{k} + \mathbf{q}, \omega + \nu) iG_0(n, \mathbf{k}, \nu) \\
 &\quad \times \langle n' \mathbf{k} + \mathbf{q} | e^{i\mathbf{q}\mathbf{r}} | n \mathbf{k} \rangle \langle n \mathbf{k} | e^{-i\mathbf{q}\mathbf{r}} | n' \mathbf{k} + \mathbf{q} \rangle. \quad (\text{A.4})
 \end{aligned}$$

Here $|n\mathbf{k}\rangle$, i.e. the wave function $\psi_{n\mathbf{k}}(\mathbf{r}) = \langle \mathbf{r} | n\mathbf{k} \rangle$, denotes single particle free Dirac electron states (see relation (2.29)) and the Green function $G_0(n, \mathbf{k}, \nu)$ is given by expression [66]

$$G_0(n, \mathbf{k}, \nu) = \frac{1 - f_{n\mathbf{k}}}{\hbar\nu - E_{n\mathbf{k}} + i\eta} + \frac{f_{n\mathbf{k}}}{\hbar\nu - E_{n\mathbf{k}} - i\eta}, \quad (\text{A.5})$$

where $f_{n\mathbf{k}}$ denotes the Fermi-Dirac distribution. After integration over energy ν we obtain

$$\begin{aligned}
 \Pi(\mathbf{q}, \omega) &= 4 \int \frac{d\mathbf{k}}{(2\pi)^2} \sum_{n, n'} \frac{f_{n\mathbf{k}} - f_{n'\mathbf{k}+\mathbf{q}}}{\hbar\omega + E_{n\mathbf{k}} - E_{n'\mathbf{k}+\mathbf{q}}} \\
 &\quad \times \langle n' \mathbf{k} + \mathbf{q} | e^{i\mathbf{q}\mathbf{r}} | n \mathbf{k} \rangle \langle n \mathbf{k} | e^{-i\mathbf{q}\mathbf{r}} | n' \mathbf{k} + \mathbf{q} \rangle, \quad (\text{A.6})
 \end{aligned}$$

and then by using the exact wave function for Dirac electrons $\psi_{n\mathbf{k}}(\mathbf{r}) = \langle \mathbf{r} | n\mathbf{k} \rangle$, given in equation (2.29), we obtain the polarizability

$$\begin{aligned} \Pi(\mathbf{q}, \omega) &= 4 \int \frac{d\mathbf{k}}{(2\pi)^2} \sum_{n,n'} \frac{f_{n\mathbf{k}} - f_{n'\mathbf{k}+\mathbf{q}}}{\hbar\omega + E_{n\mathbf{k}} - E_{n'\mathbf{k}+\mathbf{q}}} \\ &\quad \times \frac{1}{2} (1 + nn' \cos[\varphi(\mathbf{k} + \mathbf{q}) - \varphi(\mathbf{k})]). \end{aligned} \quad (\text{A.7})$$

Further on, by using relation (A.3) we can write the screened interaction

$$W(\mathbf{q}, \omega) = \frac{V(\mathbf{q})}{1 - \Pi(\mathbf{q}, \omega)V(\mathbf{q})}, \quad (\text{A.8})$$

where we recognize the expression for dielectric function of electron gas

$$\epsilon(\mathbf{q}, \omega) = 1 - \Pi(\mathbf{q}, \omega)V(\mathbf{q}) = 1 - \frac{e^2}{2\epsilon_0 q} \Pi(\mathbf{q}, \omega). \quad (\text{A.9})$$

Finally, we note that plasmons are simply defined as zeros of the dielectric function: $\epsilon(\mathbf{q}, \omega) = 0$.

Let us find now the phonon Green function for free phonons at zero temperature. Since longitudinal and transverse optical phonons are degenerate at energy $\hbar\omega_0 = 0.196$ eV, then the Green function for both branches is given by

$$D_\mu^0(\mathbf{q}, \omega) = \frac{2\hbar\omega_0}{\hbar\omega(\hbar\omega + i\eta) - (\hbar\omega_0)^2}. \quad (\text{A.10})$$

Now, the electron-phonon interaction was given in equation (2.62)

$$H_{e-ph} = L^2 \sum_{\mathbf{q}, \mu} g M_{\mathbf{q}\mu} \rho_{\mathbf{q}}^+ Q_{\mathbf{q}\mu}. \quad (\text{A.11})$$

The phonon motion can in turn polarize the electron gas which is described by a self-consistent equation for the phonon Green function renormalization (see figure A.2)

$$[-iD_\mu(\mathbf{q}, \omega)] = [-iD_\mu^0(\mathbf{q}, \omega)] + [-iD_\mu^0(\mathbf{q}, \omega)] [-i\Pi_{e-ph}(\mu, \mathbf{q}, \omega)] [-iD_\mu(\mathbf{q}, \omega)], \quad (\text{A.12})$$

so the renormalized Green function is given by an expression:

$$\begin{aligned} D_\mu(\mathbf{q}, \omega) &= \frac{D_\mu^0(\mathbf{q}, \omega)}{1 - D_\mu^0(\mathbf{q}, \omega)\Pi_{e-ph}(\mu, \mathbf{q}, \omega)} \\ &= \frac{2\hbar\omega_0}{(\hbar\omega)^2 - (\hbar\omega_0)^2 - 2\hbar\omega_0\Pi_{e-ph}(\mu, \mathbf{q}, \omega)}. \end{aligned} \quad (\text{A.13})$$

Finally, the renormalized phonon frequency is defined by a pole of the Green function

$$\omega^2 - \omega_0^2 = 2\frac{\omega_0}{\hbar}\Pi_{e-ph}(\mu, \mathbf{q}, \omega). \quad (\text{A.14})$$

Up to the lowest order, the interaction will create virtual electron-hole pair (see figure A.2) which can be described with a polarization function

$$\begin{aligned} -i\Pi_{e-ph}^0(\mu, \mathbf{q}, \omega) &= -4g^2 \int \frac{d\mathbf{k}d\nu}{(2\pi)^3} \sum_{n, n'} iG_0(n', \mathbf{k} + \mathbf{q}, \omega + \nu) iG_0(n, \mathbf{k}, \nu) \\ &\quad \times \langle n'\mathbf{k} + \mathbf{q} | M_{\mathbf{q}\mu} e^{i\mathbf{q}\mathbf{r}} | n\mathbf{k} \rangle \langle n\mathbf{k} | M_{\mathbf{q}\mu}^* e^{-i\mathbf{q}\mathbf{r}} | n'\mathbf{k} + \mathbf{q} \rangle. \end{aligned} \quad (\text{A.15})$$

We note here that $M_{\mathbf{q}\mu}$ given by equation (2.61) is two by two matrix so that polarizability $\Pi_{e-ph}^0(\mu, \mathbf{q}, \omega)$ isn't simply proportional to the function $\Pi(\mathbf{q}, \omega)$ which was obtained in relation to the screened Coulomb interaction (see relation (A.4)). In the context of Feynman diagrams we can say that diagram vertices are different for the case of Coulomb (electron-electron) interaction from the case of electron-phonon interaction. Further on, we obtain

$$\begin{aligned} \Pi_{e-ph}^0(\mu, \mathbf{q}, \omega) &= 4g^2 \int \frac{d\mathbf{k}}{(2\pi)^2} \sum_{n, n'} \frac{f_{n\mathbf{k}} - f_{n'\mathbf{k}+\mathbf{q}}}{\hbar\omega + E_{n\mathbf{k}} - E_{n'\mathbf{k}+\mathbf{q}}} \\ &\quad \times \langle n'\mathbf{k} + \mathbf{q} | M_{\mathbf{q}\mu} e^{i\mathbf{q}\mathbf{r}} | n\mathbf{k} \rangle \langle n\mathbf{k} | M_{\mathbf{q}\mu}^* e^{-i\mathbf{q}\mathbf{r}} | n'\mathbf{k} + \mathbf{q} \rangle. \end{aligned} \quad (\text{A.16})$$

Let us now take the exact form of the wave function $\psi_{n\mathbf{k}}$ and the matrix element $M_{\mathbf{q}\mu}$ according to relations (2.29) and (2.61). We can see that the polarizability depends on the phonon polarization and we obtain

$$\begin{aligned} \Pi_{e-ph}^0(L, \mathbf{q}, \omega) &= 4g^2 \int \frac{d\mathbf{k}}{(2\pi)^2} \sum_{n, n'} \frac{f_{n\mathbf{k}} - f_{n'\mathbf{k}+\mathbf{q}}}{\hbar\omega + E_{n\mathbf{k}} - E_{n'\mathbf{k}+\mathbf{q}}} \\ &\quad \times \frac{1}{2}(1 - nn' \cos[2\varphi(\mathbf{q}) - \varphi(\mathbf{k}) - \varphi(\mathbf{k} + \mathbf{q})]), \text{ and} \end{aligned} \quad (\text{A.17})$$

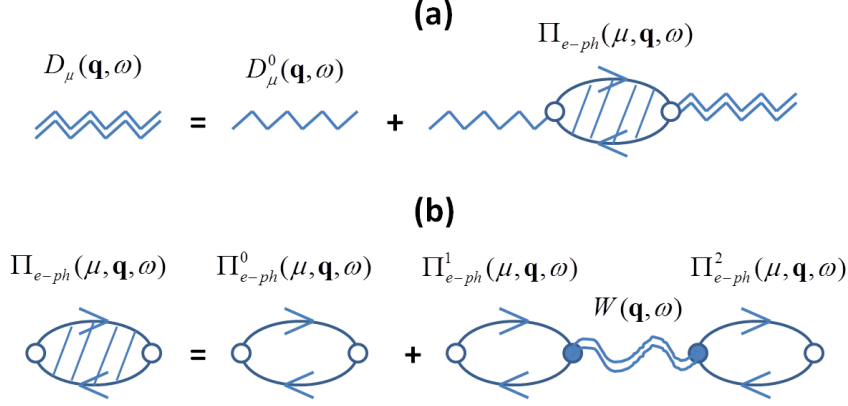


Figure A.2: (a) Feynman diagrams for phonon Green function renormalization. (b) Feynman diagrams for polarizability function. Note that the electron-electron interaction vertex is different from the electron-phonon vertex.

$$\begin{aligned} \Pi_{e-ph}^0(T, \mathbf{q}, \omega) &= 4g^2 \int \frac{d\mathbf{k}}{(2\pi)^2} \sum_{n,n'} \frac{f_{n\mathbf{k}} - f_{n'\mathbf{k}+\mathbf{q}}}{\hbar\omega + E_{n\mathbf{k}} - E_{n'\mathbf{k}+\mathbf{q}}} \\ &\quad \times \frac{1}{2} (1 + nn' \cos[2\varphi(\mathbf{q}) - \varphi(\mathbf{k}) - \varphi(\mathbf{k} + \mathbf{q})]). \quad (\text{A.18}) \end{aligned}$$

If we now imagine that phonon energy and momentum matches plasmon energy and momentum, then the electron-phonon interaction will be amplified through the collective electron response. In that case it won't be sufficient to calculate only the polarization of single electron hole pair and we will have to take into consideration contribution from the infinite sequence of bubble diagrams (which are in fact necessary to describe plasmon excitation). The easiest way to do this is to take the electron-phonon interaction which polarizes a single electron hole pair and include the possibility that Coulomb interaction can in turn create another electron hole pair. The infinite sequence of diagrams can be included if we work from the start with screened Coulomb interaction instead of bare interaction and one should take special account of the nature of diagram vertices considering if the electron hole pair was created by Coulomb or electron-phonon interaction (see figure A.2). In that way we obtain the screened electron-phonon polarizability in the Random Phase Approximation

$$\Pi_{e-ph}(\mu, \mathbf{q}, \omega) = \Pi_{e-ph}^0(\mu, \mathbf{q}, \omega) + \Pi_{e-ph}^1(\mu, \mathbf{q}, \omega)W(\mathbf{q}, \omega)\Pi_{e-ph}^2(\mu, \mathbf{q}, \omega). \quad (\text{A.19})$$

Here $W(\mathbf{q}, \omega) = \frac{V(\mathbf{q})}{1 - \Pi(\mathbf{q}, \omega)V(\mathbf{q})}$ so we immediately see that if phonon disper-

sion crosses the plasmon dispersion then the electron-phonon interaction will be amplified due the collective electron response where we have $\epsilon(\mathbf{q}, \omega) = 1 - \Pi(\mathbf{q}, \omega)V(\mathbf{q}) = 0$. That part is in fact responsible for the plasmon phonon coupling. Finally the polarizability describing the bubble with different vertices is given by

$$\begin{aligned} \Pi_{e-ph}^1(\mu, \mathbf{q}, \omega) &= \Pi_{e-ph}^2(\mu, \mathbf{q}, \omega)^* = 4g \int \frac{d\mathbf{k}}{(2\pi)^2} \sum_{n,n'} \frac{f_{n\mathbf{k}} - f_{n'\mathbf{k}+\mathbf{q}}}{\hbar\omega + E_{n\mathbf{k}} - E_{n'\mathbf{k}+\mathbf{q}}} \\ &\quad \times \langle n'\mathbf{k} + \mathbf{q} | M_{\mathbf{q}\mu} e^{i\mathbf{q}\mathbf{r}} | n\mathbf{k} \rangle \langle n\mathbf{k} | e^{-i\mathbf{q}\mathbf{r}} | n'\mathbf{k} + \mathbf{q} \rangle. \end{aligned} \quad (\text{A.20})$$

If we include here the exact wave function $\psi_{n\mathbf{k}}$ and matrix elements $M_{\mathbf{q}\mu}$, we obtain different expressions depending on the phonon polarization:

$$\begin{aligned} \Pi_{e-ph}^1(L, \mathbf{q}, \omega) &= 4g \int \frac{d\mathbf{k}}{(2\pi)^2} \sum_{n,n'} \frac{f_{n\mathbf{k}} - f_{n'\mathbf{k}+\mathbf{q}}}{\hbar\omega + E_{n\mathbf{k}} - E_{n'\mathbf{k}+\mathbf{q}}} \\ &\quad \times \frac{i}{2} (n \sin[\varphi(\mathbf{q}) - \varphi(\mathbf{k})] + n' \sin[\varphi(\mathbf{q}) - \varphi(\mathbf{k} + \mathbf{q})]), \text{ and} \end{aligned} \quad (\text{A.21})$$

$$\begin{aligned} \Pi_{e-ph}^1(T, \mathbf{q}, \omega) &= 4g \int \frac{d\mathbf{k}}{(2\pi)^2} \sum_{n,n'} \frac{f_{n\mathbf{k}} - f_{n'\mathbf{k}+\mathbf{q}}}{\hbar\omega + E_{n\mathbf{k}} - E_{n'\mathbf{k}+\mathbf{q}}} \\ &\quad \times \frac{i}{2} (n \cos[\varphi(\mathbf{q}) - \varphi(\mathbf{k})] + n' \cos[\varphi(\mathbf{q}) - \varphi(\mathbf{k} + \mathbf{q})]). \end{aligned} \quad (\text{A.22})$$

Let us first analyze interaction with the longitudinal optical phonons. In that respect let us take expression (A.21) and assume, without the loss of generality, that $\varphi(\mathbf{q}) = 0$ i.e. vector \mathbf{q} is along \hat{x} direction. We than obtain

$$\begin{aligned} \Pi_{e-ph}^1(L, \mathbf{q}, \omega) &= 4g \int \frac{d\mathbf{k}}{(2\pi)^2} \sum_{n,n'} \frac{f_{n\mathbf{k}} - f_{n'\mathbf{k}+\mathbf{q}}}{\hbar\omega + E_{n\mathbf{k}} - E_{n'\mathbf{k}+\mathbf{q}}} \\ &\quad \times \frac{i}{2} (-n \sin[\varphi(\mathbf{k})] - n' \sin[\varphi(\mathbf{k} + \mathbf{q})]). \end{aligned} \quad (\text{A.23})$$

But the function under the integral sign is odd with respect to reflection across the x axis, meaning that the entire integral vanishes i.e. $\Pi_{e-ph}^1(L, \mathbf{q}, \omega) = 0$.

In other words we have shown analytically that there is no whatsoever coupling of plasmons and longitudinal optical phonons! Finally, to find the coupling of plasmons with transverse optical phonons one only needs to solve self-consistent set of equations (A.14) and (A.19) which was done numerically and demonstrated to agree with the results of chapter 5, where we used different gauge to obtain the same result.

Bibliography

- [1] P.R. Wallace, Phys. Rev. **71**, 622 (1947).
- [2] G.W. Semenoff, Phys. Rev. Lett. **53**, 2449 (1984).
- [3] R.E. Peierls, Ann. I. H . Poincare **5**, 177 (1935).
- [4] L.D. Landau, Zh. Eksp. Teor. Fiz, **7**, 19 (1937).
- [5] K.S. Novoselov, *et al.*, Science **306**, 666 (2004).
- [6] K.S. Novoselov, D. Jiang, F. Schedin, T.J. Booth, V.V. Khotkevich, S.V. Morozov, and A.K. Geim, Proc. Natl. Acad. Sci. USA **102**, 10451 (2005).
- [7] K.S. Novoselov, *et al.*, Nature (London) **438**, 197 (2005).
- [8] A. Reina, *et al.*, Nano Lett. **9**, 30 (2009).
- [9] K.V. Emtsev, *et al.*, Nature Mater. **8**, 203 (2009).
- [10] Y. Hernandez, *et al.*, Nature Nanotech. **3**, 563 (2008).
- [11] I. Pletikosić, *et al.*, Phys. Rev. Lett. **102**, 056808 (2009).
- [12] W.L. Barnes, A. Dereux, T.W. Ebbesen, Nature (London) **424**, 824 (2003).
- [13] S.A. Maier, H.A. Atwater, J. Appl. Phys. **98**, 011101 (2005).
- [14] H. Lee, S. Vudentam, J. Tang, J. Conway, M. Staffaroni, E. Yablonovitch, arXiv:0810.1553.
- [15] A. Karalis, E. Lidorikis, M. Ibanescu, J.D. Joannopoulos, M. Soljačić, Phys. Rev. Lett. **95**, 063901 (2005).

- [16] V.G. Veselago, Sov. Phys. Uspekhi **10**, 509 (1968).
- [17] V.M. Shalaev, Nature Photonics **1**, 41 (2007).
- [18] J.B. Pendry, Phys. Rev. Lett. **85**, 3966 (2000).
- [19] D.R. Smith, J.B. Pendry, M.C.K. Wiltshire, Science **305**, 788 (2004).
- [20] S. Rytov, Yu.A. Kratsov, V.I. Tatarskii, *Principles of Statistical Radiophysics* (Springer-Verlag, 1987).
- [21] D. Polder, M. Van Hove, Phys. Rev. B **4**, 3303 (1971).
- [22] J. Pendry, Journal of Physics: Condensed Matter **11**, 6621 (1999).
- [23] C. Hargreaves, Physics Letters A **30**, 491 (1969).
- [24] A. Narayanaswamy, S. Shen, G.Chen, Phys. Rev. B **78**, 115303 (2008).
- [25] S. Shen, A. Narayanaswamy, G. Chen, Nano Letters **9**, 2909 (2009). PMID: 19719110.
- [26] E. Rousseau, A. Siria, G. Jourdan, S. Volz, F. Comin, J. Chevrier, and J.-J. Greffet, Nature Photonics **3**, 514 (2009).
- [27] T.J. coutts, Sol. Energy. Mater. Sol. Cells, **66**, 443 (2001).
- [28] M.G. Mauk, Mid-Infrared Semiconductor Optoelectronics, **118**, 673 (2006).
- [29] M. Whale, E. Cravalho, Energy Conversion, IEEE Transactions **17** 130 (2002).
- [30] M. Laroche, R. Carminati, J.-J. Greffet, J. Appl. Phys. **100**, 063704 (2006).
- [31] M. Francoeur, R. Vaillon, M.P. Menguc, Energy Conversion, IEEE Transaction **26**, 686 (2011).
- [32] S. Pisana *et al.*, Nature Materials **6**, 198 (2007)
- [33] L.I. Schiff, *Quantum Physics*, 1st. ed., McGraw-Hill book company, 1949

- [34] N.D. Mermin, *Lindhard Dielectric Function in the Relaxation-Time Approximation*, Phys. Rev. B **1**, 2362 (1970).
- [35] Ch.-H. Park, F. Giustino, M.L. Cohen, S.G. Louie, Phys. Rev. Lett. **99**, 086804 (2007).
- [36] T. Stauber, N.M.R. Peres, and A.H. Castro-Neto, Phys. Rev. B **78**, 085418 (2008).
- [37] R.R. Nair, P. Blake, A.N. Grigorenko, K.S. Novoselov, T.J. Booth, T. Stauber, N.M.R. Peres, A.K. Geim, Science **320**, 1308 (2008).
- [38] N.W. Ashcroft, N.D. Mermin, *Solid State Physics*, (Saunders, Philadelphia, PA, 1976).
- [39] W.H. Backes, F.M. Peeters, F. Brosens, J.T. Devreese, Phys. Rev. B **45**, 8437 (1992).
- [40] B. Wunsch, T. Stauber, F. Sols, F. Guinea, N. Jour. of Phys. **8**, 318 (2006).
- [41] E.H. Hwang, S. Das Sarma, Phys. Rev. B **75**, 205418 (2007).
- [42] F. Stern, Phys. Rev. Lett. **18**, 546 (1967).
- [43] E.A. Taft, H.R. Philipp, Phys. Rev. **138**, 197 (1965).
- [44] K.-F. Mak, M.Y. Sfeir, Y. Wu, C.-H. Lui, J.A. Misewich, and T.F. Heinz, Phys. Rev. Lett. **101**, 196405 (2008).
- [45] M. Soljačić, J.D. Joannopoulos, Nature Mater. **3**, 211 (2004).
- [46] F. Rana, IEEE Transactions on Nanotechnology **7**, 91 (2008).
- [47] A.K. Geim, K.S. Novoselov, Nature Mater. **6**, 183 (2007).
- [48] S.A. Mikhailov, K. Ziegler, Phys. Rev. Lett. **99**, 016803 (2007).
- [49] E.J. Nicol and J.P. Carbotte, Phys. Rev. B **77**, 155409 (2008).
- [50] A.H. Castro Neto, F. Guinea, N.M.R. Peres, K.S. Novoselov, and A.K. Geim, Rev. Mod. Phys. **81**, 109 (2009).
- [51] T. Ando, J. Phy. Soc. Jpn. **75**, 124701 (2006)

- [52] H. Suzuura, T. Ando, Phys. Rev. B, **65**, 235412 (2002).
- [53] K. Ishikawa, T. Ando, J. Phy. Soc. Jpn. **75**, 084713 (2006).
- [54] A. Principi, M. Polini, G. Vignale, Phys. Rev. B, **80**, 075418 (2009).
- [55] L.A. Falkovsky, A.A. Varlamov, Eur. Phys. J. B **56**, 281 (2007).
- [56] D. Pines, P. Nozieres, *The Theory of Quantum Liquids* (Benjamin, New York, 1966).
- [57] Y. Liu and R. F. Willis, Phys. Rev. B 81, 081406 (2010).
- [58] S.Rytov, A.Kratsov, Yu, and V.I. Tatarskii, *Principles of Statistical Radiophysics* (Springer-Verlag, 1987).
- [59] H.A. Haus, Journal of Applied Physics **32**, 493 (1961).
- [60] J.E. Sipe, J. Opt. Soc. Am. B **4**, 481 (1987).
- [61] L. A. Falkovsky, Journal of Physics: Conference Series **129**, 012004 (2008).
- [62] N. M. Gabor, J. C. W. Song, Q. Ma, N. L. Nair, T. Taychatanapat, K. Watanabe, T. Taniguchi, L. S. Levitov, and P. Jarillo-Herrero, Science **334**, 648 (2011).
- [63] J.R.Dixon, J.M.Ellis, Phys. REv. **123**, 1560 (1961).
- [64] G.W.Gobei, H.Y.Fan, Phys. Rev. **119**, 613 (1960).
- [65] I.Celanovic *et al.*, Opt. Lett. **29**, 863 (2004).
- [66] M. Šunjić, *Kvantna fizika mnoštva čestica*, Školska knjiga, Zagreb, 2002
- [67] J. D. Jackson, *Classical Electrodynamics*, 3rd ed., John Willey and Sons, Inc., 1999
- [68] J. J. Sakurai, *Modern Quantum Mechanics*, Addison-Wesley Publishing Company, Inc., 1994
- [69] W. Shockley, H.J. Queisser, Journal of Applied Physics, **32**, 510 (1961).

[70] I. Hamberg, C.G. Granqvist, *Journal of Applied Physics*, **60**, R123-R160 (1986).

[71] P. West, *et al.*, *Laser and Photonics Reviews* **4**, 795-808 (2010).

List of Figures

- 2.1 a) Graphene crystal structure. Unit cell vectors are \mathbf{a}_1 and \mathbf{a}_2 while A and B are atoms of the basis. b) Brillouin zone. We mark high symmetry points \mathbf{K} and \mathbf{K}' where the low-energy electron excitations are described by massless Dirac equation. 8
- 2.2 Graphene electron band structure with Dirac cones around \mathbf{K} point (magnified). Intrinsic graphene has Fermi level $E_F = E_{\mathbf{K}} = 0$ 11
- 2.3 a) Atom motion in graphene during the longitudinal optical phonon oscillations. b) Motion of basis atoms described by a vector \mathbf{u} in the real space induces vector potential \mathbf{A} that moves Dirac points in the reciprocal space. Dirac point symmetry causes unusual polarization of this vector potential: $\mathbf{A} \perp \mathbf{u}$ 15
- 2.4 (a) Schematic diagram of the radiation transfer problem: a free standing sheet of graphene at temperature T_1 is radiating to another free standing graphene sheet at temperature T_2 and distance D away. (b) Polarization vectors defined in the text. 34
- 3.1 (a) Schematic description of a surface plasmon (SP) on metal-dielectric interface. (b) SP dispersion curve (solid blue line) for Ag-Si interfaces; dotted blue is the light line in Si; dashed red line denotes the SP resonance. (c) Wave localization and propagation length for SPs at Ag-Si interface (experimental Ag losses are taken into account). 40

- 3.2 (a) Schematic of the graphene system and TM plasmon modes. Note that the profile of the fields looks the same as the fields of an SP [Fig. 3.1(a)]. (b) Electronic band structure of graphene; to indicate the vertical scale we show the Fermi energy level for the case $E_F = 1$ eV. (c) Sketch of the intraband (green arrows) and interband (red arrows) single particle excitations that can lead to large losses; these losses can be avoided by implementing a sufficiently high doping. (d) Plasmon RPA and semiclassical dispersion curves. Black solid (RPA) and black dot-dashed (semiclassical) lines correspond to $\epsilon_{r1} = \epsilon_{r2} = 1$; Blue dashed (RPA) and blue dotted (semiclassical) lines correspond to $\epsilon_{r1} = 4$ and $\epsilon_{r2} = 1$. The green (lower) and rose (upper) shaded areas represent regimes of intraband and interband excitations, respectively. 42
- 3.3 Properties of plasmons in doped graphene. Solid-lines are obtained with the number-conserving RPA calculation, and the dashed lines with the semiclassical approach. Losses (a), field localization (wave "shrinkage") (b), and group velocity (c) for doping $E_F = 0.135$ eV, and relaxation time $\tau = 1.35 \times 10^{-13}$ s, which corresponds to the mobility of 10000 cm²/Vs. The upper scale in all figures is frequency $\nu = \omega/2\pi$, whereas the rose shaded areas denote the region of high interband losses. 46
- 3.4 (a) The real part of the conductivity in units of $\sigma_0 = \pi e^2/2h$ in dependence of frequency $\hbar\omega/E_F$, and (b) the corresponding relaxation time as a function of wavelength. The contribution to $\Re\sigma(\omega)$ from impurities is chosen to be negligible. The displayed graphs correspond to two different values of doping which yield $E_F = 0.135$ eV (solid blue line), and $E_F = 0.640$ eV (dashed red line). The position of the optical phonon frequency $\hbar\omega_{Oph} \approx 0.2$ eV is depicted by the dotted vertical line in (b); dot-dashed lines depict the values of wavelengths corresponding to $2E_F$, that is, the interband threshold value (for $q = 0$) for the two doping concentrations. 48

3.5 Properties of plasmons in doped graphene. Solid-lines are obtained with the number-conserving RPA calculation, and the dashed lines with the semiclassical approach. Losses (a), field localization (wave "shrinkage") (b), and group velocity (c) for doping $E_F = 0.64$ eV; losses are calculated by using the relaxation time $\tau^{-1} = \tau_{DC}^{-1} + \tau_{e-ph}^{-1}$, where $\tau_{DC} = 6.4 \times 10^{-13}$ s, and τ_{e-ph} is the relaxation time from the electron-phonon coupling for the given parameters. In the white regions (right regions in all panels), losses are determined by τ_{DC} . In the yellow shaded regions (central regions in all panels), losses are determined by the optical phonon emission, i.e., τ_{e-ph} . The rose shaded areas (left region in all panels) denote the region of high interband losses. Dotted vertical lines correspond to the optical phonon frequency $\omega_{Oph} \approx 0.2$ eV. The upper scale in all figures is frequency $\nu = \omega/2\pi$. See text for details. 49

4.1 The band-structure of bilayer graphene. The two upper bands (as well as the two lower bands) are perfectly nested and separated by $\gamma \sim 0.4$ eV; $q_0 = \gamma/\hbar v_F$. Horizontal line depicts one possible value of the Fermi level, and arrows denote some of the possible interband electronic transitions. See text for details. 54

4.2 The real (red dotted lines) and imaginary (blue solid lines) part of the conductivity of bilayer graphene for two values of doping: $\mu = 0.4\gamma$ (a), and $\mu = 0.9\gamma$ (b). The conductivity is in units of $\sigma_0 = e^2/2\hbar$, and the frequency is in units of $\omega_0 = \gamma/\hbar$. The δ -functions in $\Re\sigma(\omega)$ at $\omega = 0$ (intraband transitions) and $\omega = \gamma/\hbar$ (transitions from the lower to the upper conduction band depicted as green solid arrows in Fig. 4.1) are not shown (see [49]). 57

- 4.3 The plasmon dispersion curve $\Delta q = q - \omega/c$ vs. ω for $\mu = 0.4\gamma$ (a), and $\mu = 0.9\gamma$ (b) is shown as blue solid line. To the right of the vertical red dotted lines plasmons can be damped via excitation of electron-hole pairs, whereas to the left of this line these excitations are forbidden due to the Pauli principle. Black dashed line in (b) (which closely follows the blue line) corresponds to Eq. (4.8). The wave vector is in units of $q_0 = \gamma/\hbar v_F$, and the frequency is in units of $\omega_0 = \gamma/\hbar$ 58
- 5.1 (a) Schematic illustration of the lattice structure with two sublattices (A and B). (b) The two degenerate Dirac cones are centered at K and K' points at the edge of the Brillouin zone. (c) A displacement of lattice atoms $\mathbf{u}(\mathbf{r})$ is parallel (perpendicular) to the propagation wave vector \mathbf{q} of a LO (TO) phonon. (d) The displacement $\mathbf{u}(\mathbf{r})$ creates an effective vector potential \mathbf{A}_{eff} perpendicular to $\mathbf{u}(\mathbf{r})$ (the sign of \mathbf{A}_{eff} for the K' point is opposite to that for the K point). 63
- 5.2 Dispersion lines of hybrid LP-TO plasmon-phonon modes (solid lines) and of the uncoupled modes (dashed lines) for two values of doping: (a) $n = 5 \times 10^{12} \text{ cm}^{-2}$, and (b) $n = 5 \times 10^{13} \text{ cm}^{-2}$. The hybridization is stronger for larger doping values. Grey areas denote the region of single-particle damping. 66
- 5.3 Dispersion lines of hybrid TP-LO plasmon-phonon modes (solid lines) and of the uncoupled modes (dashed lines) for two values of doping: (a) $n = 7.5 \times 10^{11} \text{ cm}^{-2}$, and (b) $n = 9.5 \times 10^{11} \text{ cm}^{-2}$. The plasmon-like dispersion is very close to the light line $q = \omega/c$; therefore, the ordinate shows $\Delta q = q - \omega/c$ 67

6.1	(a) Schematic diagram of the radiation transfer problem: a free standing sheet of graphene at temperature T_1 is radiating to another free standing graphene sheet at temperature T_2 and distance D away. (b) Schematic diagram of the field profile for even mode. (c) Odd mode. (d) Contour plot of the transfer function h_{nf}^p for the case of two graphene sheets at the same chemical potentials $\mu_{1,2} = 0.5eV$ and same temperatures $T_{1,2} = 300K$, separated by a distance of $D = 10$ nm. Dashed line denotes the plasmon dispersion relation for a single isolated graphene sheet, while poles of transfer function h_{nf}^p show dispersion relations of the coupled (even and odd) modes of the two sheets.	72
6.2	Contour plot of the near field heat transfer between two graphene sheets H_{gg}^{nf} normalized to the far field heat transfer between two black bodies H_{BB}^{ff} of the same temperatures, in the log scale. Here $T_2 = 300K$, $\mu_{1,2} = 0.1eV$ and $\tau_{1,2} = 10^{-13}s$	75
A.1	(a) Feynman diagram for bare Coulomb interaction $V(\mathbf{q})$. (b) Polarizability $\Pi(\mathbf{q}, \omega)$. (c) and (d) Screened Coulomb interaction $W(\mathbf{q}, \omega)$ in the Random Phase Approximation.	82
A.2	(a) Feynman diagrams for phonon Green function renormalization. (b) Feynman diagrams for polarizability function. Note that the electron-electron interaction vertex is different from the electron-phonon vertex.	85